

The Rapid Analytical-FEA Technique for Reduced Simulation Times of Piezoelectric MEMS Resonators

A Dissertation

Presented to the Faculty of the Graduate School

of Cornell University

in Partial Fulfillment of the Requirements for the Degree of

Doctor of Philosophy

By

Jonathan Michael Puder

May 2018

© 2018 Jonathan Michael Puder

The Rapid Analytical-FEA Technique for Massively Reduced Simulation Times of
Piezoelectric MEMS Resonators

Jonathan Michael Puder, Ph.D.

Cornell University 2018

Piezoelectric radio frequency microelectromechanical resonators are a promising technology for meeting the increasing demands of a crowded electromagnetic spectrum. Contour mode resonators are a potential technology for next generation filtering to replace current bulk acoustic wave (BAW) solutions. The lithographically defined center frequencies of contour mode resonators facilitate monolithic integration of multiple frequencies on a single chip, ideal for filter bank applications. Despite these advantages, contour mode resonator technology has not seen widespread use in commercial or military applications, with one of the main obstacles towards this end being spurious modes. Frequently, designs optimally exciting an intended mode will often excite many other modes. This can affect important performance metrics, such as the passband roll-off and group delay of filters created from these resonators, and potentially exposes the radio system to damaging high power signals.

Part of the reason spurious modes remain a challenge is the lack of a rapid and wide-band simulation technique. Piezoelectric resonators typically have complex responses that must be modeled using finite element analysis (FEA) for accuracy. Conventionally, a multi-physics harmonic analysis is run to model resonators. These simulations can take hours to days to complete. Trades must be made between frequency spacing and bandwidth for the simulation to complete in a reasonable amount of time, and can

possibly miss modes. Due to the time limitations, designers often run 2D simulations which complete much faster, but will miss any out-of-plane information.

To address these challenges, the wide-band Rapid Analytical-FEA Technique (RAFT) has been developed using software commonly found in research laboratories. The RAFT combines the speed of analytical analysis with the accuracy of FEA for full 3D solutions that complete orders of magnitude faster than conventional harmonic analysis while accurately modeling relevant modes. This enhanced speed is enabled by generalized expressions for the motional parameters of the modified Butterworth van-Dyke equivalent circuit: the motional resistance (R_m), inductance (L_m), and capacitance (C_m). Information from separate mechanical modal analysis and electrostatic analysis are entered into these expressions, and the frequency response is then simulated in analytical software. This accounts for the effect of all modes in the simulation bandwidth.

This method is shown to improve simulation speeds by several orders of magnitude. Additionally, the RAFT enables new uses of FEA for design and analysis. Wide band simulations to assess the resonator performance far from resonance are now possible. Accurate parametric device exploration to investigate mode scaling and behavior to higher frequencies can be undertaken. The reduced simulation duration frees time for researchers to conduct studies of other critical device variables, such as the simulations of fabrication non-idealities, including electrode misalignment or sidewall angles. These effects are often not simulated due to time constraints. Thermal effects on frequency may be included to generate frequency-temperature curves for each mode's unique response to temperature variations.

BIOGRAPHICAL SKETCH

Jonnathan M. Puder was born in Boston Massachusetts in 1989. He received the B.S., M.S., and Ph.D. degrees in Mechanical Engineering from the Cornell University Sibley School of Mechanical and Aerospace Engineering in 2012, 2016, and 2017, respectively. He joined the OxideMEMS Lab of Cornell University as an Undergraduate Research Assistant University in 2012 under the supervision of Professor Sunil Bhawe. He later continued his Masters and Ph.D. work in the same group, where he worked on MEMS gyroscopes and piezoelectric MEMS resonators. In 2014, he also joined the PiezoMEMS Team at the US Army Research Laboratory (ARL), Adelphi, MD as an ORAU Graduate Researcher under the mentorship of Dr. Ronald Polcawich, Jeffrey Pulskamp, and Dr. Ryan Rudy. He has completed his Ph.D. work while at the US ARL, which has been focused on simulation enhancement of piezoelectric MEMS resonators. His work was selected as a best paper finalist at the 2017 International Frequency Control Symposium.

To my Father and Mother

Acknowledgements

I would like to thank my advisor Professor Sunil Bhave, who first saw something special in me as an undergraduate student in 2011, then took a leap of faith and offered to take me on as a Ph.D. student in 2012. Without your support of and belief in me, nothing I have accomplished in these past 5 years would be possible. It is difficult to enumerate your many gifts to me, but I will name some of the most salient in my mind: inviting me to earn my Ph.D., helping me with my Q exam, fighting for my right to remain a student, orchestrating the amazing opportunity at the US Army Research Laboratory, and always being available to provide your wisdom and cool-headed advice. I admire your generosity to your students, your (seeming) omniscience, your bird's-eye-view of the technology space, and your ability to push your students to achieve. Thank you for believing in me when I did not believe in myself.

I would like to thank past and present members of the PiezoMEMS Team at the US Army Research Laboratory for welcoming me and affording me the opportunity to complete my Ph.D.: Dr. Ron Polcawich, Jeff Pulskamp, Dr. Ryan Rudy, Dr. Bob Benoit, Dr. Dan Potrepka, Dr. Luz Sanchez, Joel Martin, Brian Power, and Manny Rivas. I would like to also thank Diane Green for your help in all things administrative. I would particularly like to thank Jeff Pulskamp for his mentorship. Your generosity in terms of both time and knowledge and your belief in my abilities were a catalyst to my success. I would also like to thank Ryan Rudy for his patience, friendship, and insightful discussions. Your ability to listen, question my ideas, and talk through my latest crazy idea has been invaluable. To Ron Polcawich, thank you for guidance and always

providing your much-contested time, and for first agreeing to take me on as a summer intern. I look at you and your career as a model of what I hope to achieve.

I would also like to thank other scientists at ARL, namely Ryan Knight, Sarah Bedair, and Gabe Smith for lending their insights and friendship. I would also like to thank Branch Chiefs Brett Piekarski and Will Nothwang for allowing me to continue my research at the US ARL.

I would also like to thank my Cornell committee members: chair Professor Amit Lal, and minor members Professors David Erickson and Clifford Pollock. Thank you for abiding my many requests for signatures and forms. Thank you in particular to Amit for taking on the additional headache filling in as my advisor. Thank you to Marcia Sawyer for acting as my liaison to the Graduate School and DGS and ensuring that I was meeting the many requirements for graduation.

Thank you to the various members of the OxideMEMS Lab at Cornell University who I have had the pleasure to call my colleagues and friends: Ryan Wang, Tanay Gosavi, Siddarth Tallur, Tiffany Cheng, Laura Fegely, Ben Tang, Ajay Bhat, and Matt Storey. Thank you to Ryan for your mentorship in the first year of my Ph.D. Thank you to Tanay for your guidance and taking me under your wing as a first year student.

Thank you to my friends. Thank you to Sam Tremlett and family. Your family's acceptance of me as one of their own has been invaluable and is something I still treasure despite how infrequently we see each other. Thank you to my Mech. E. friends James Young, Anthony Savas, and Francis Lora. My undergraduate and early graduate years would not have been so fondly remembered without your friendship. Thank you to Patrick Stewart for your continued friendship despite my shortcomings as a friend.

Caitlyn Leasure, thank for your support, encouragement, loyalty, trust, kindness, and for listening to my every thought on anything. Thank you for your unending patience though my various hobbies, projects, and interests when I dig myself in over my head. Thank you for choosing me.

Thank you to my family, Mark and Elena, Matt, and Rachel Puder. Thank you Mom and Dad for making sure we had a better life than you had. Thank you Dad for sacrificing so much for your children, for encouraging me, for setting me up for a successful future, and letting me be my own person. You are an inspiration to me and I hope I have made you proud.

I would also to like to thank various others: Dana Weinstein, Cliff Lardin, Shayhaan Desai, Brad Treat, Cristian Cassella, Guofeng Cheng, Sachin Nadig, the Cornell Nanofabrication Facility staff, Sue Bulkley, John Pavco, Nick Contreras, Alex Chip, the Sushanth Family, Elena Contreras, Alain and Vanessa Laroche, Rick and Bob Puder, Paul Muniz, and Jonathan Daudelin,

TABLE OF CONTENTS

CHAPTER 1.....	1
1.1 Piezoelectric Contour-Mode Radio-Frequency MEMS Resonators	1
1.1.1 Operating Principles	4
1.1.2 Commonly Studied Modes	12
1.1.3 State of the Technology.....	14
1.2 Spurious Modes.....	16
1.2.1 Introduction to Spurious Modes	16
1.2.2 The Spurious Mode Problem in FBARS	17
1.2.3 The Spurious Mode Problem in Contour Mode Resonators	18
1.3 Common Piezoelectric Thin Films for Contour Mode Resonators	20
1.3.1 Introduction	20
1.3.2 Aluminum Nitride (AlN).....	21
1.3.1 Lead Zirconate Titanate (PZT).....	22
1.3.2 Lithium Niobate	25
CHAPTER 2.....	27
2.1 The mBVD Model.....	27
2.1.1 Modal Analysis.....	27
2.1.2 Overview of mBVD	31
2.1.3 Optimal mBVD Values	36
2.1.4 Modifying the mBVD to Model Multiple Acoustic Modes	39
2.2 The Motional Resistance.....	41
2.2.1 Introduction	41
2.2.2 Previous Efforts.....	41
2.2.3 Derivation of the Generalized Motional Resistance, Capacitance, Inductance, and Electromechanical Coupling.....	44
2.2.4 Alternative Derivation of the Motional Resistance	53
2.2.5 Specific Expressions for the Motional Resistance: Beam Extension, Beam Flexure, Disk Flexure, and the A0 Lamb Mode	57
CHAPTER 3.....	71
3.1 Modeling and Extracting mBVD Parameters.....	71
3.1.1 Introduction	71
3.1.2 Extraction from Measured Microwave Parameters	71
3.1.3 Extraction from Test Structures	76

3.2	4.2 Validation of Motional Resistance Equation.....	76
3.2.1	Beam Flexure Resonators.....	77
3.2.2	Disk Resonators.....	81
CHAPTER 4.....		87
4.1	Overview of RAFT.....	87
4.1.1	RAFT Overview.....	87
4.1.2	Advantages of RAFT.....	88
4.1.3	Assumptions and Limitations.....	90
4.2	Wide Band Sweeps and Validation.....	92
4.2.1	Resonators, Material Properties, and mBVD Parameter Extraction for Wide Band Validation.....	92
4.2.2	PZT-on-Silicon Disk Resonator.....	94
4.2.3	PZT-on-Silicon Beam Resonator.....	97
4.2.4	AlN Cross-Sectional Lamé Mode Bar Resonators.....	99
4.3	5.3 Other Modeling Capabilities Enabled by RAFT.....	105
4.3.1	Wide Band Spur Suppression.....	105
4.3.2	Parametric Device Design.....	118
4.4	RAFT Discussion.....	124
4.4.1	Comparison to COMSOL®.....	124
4.4.2	Qualitative Comparison to Coventorware®.....	125
4.4.3	Gyroscopes.....	125
4.4.4	Ultrasonic Motors.....	126
4.4.5	Strain Sensors.....	126
4.4.6	PMUTs.....	127
4.4.7	Energy Harvesters.....	127
CHAPTER 5.....		128
5.1	Future Work.....	128
5.1.1	Applicability to Other Transduction Methods.....	129
5.1.2	Quality Factor Modeling.....	130
5.2	Summary of Contribution to the Body of Work.....	131
APPENDIX A - CODE.....		133
APPENDIX B – Disk Cross-Sectional Lamé Mode Resonators.....		147
CHAPTER 6 Bibliography.....		152

CHAPTER 1

PIEZOELECTRIC MEMS RESONATORS

1.1 Piezoelectric Contour-Mode Radio-Frequency MEMS Resonators

Contour-mode piezoelectric radio-frequency (RF) microelectromechanical (MEMS) resonators are of interest for next generation front-end filtering capabilities [1]. Acoustic wavelengths are much shorter than electromagnetic waves at the same frequency (approximately 10^5 time smaller [2]), providing massive size advantages for MEMS devices. The piezoelectric effect, which transduces directly between electrical and mechanical domains, is a logical phenomenon to exploit these size advantages for radio signal filtering at frequencies below several gigahertz. Additionally, the materials and topologies utilized in these resonators tend to have intrinsically low mechanical loss and high Q (or in the case of PZT resonators, high loss is compensated for with silicon). These devices have displayed characteristic impedances allowing for direct interface with $50\ \Omega$ terminated devices without any external matching [3, 4, 5]. Electrostatic drive MEMS resonators are widely used in devices and have displayed very high quality factors [6], but suffer from low coupling factors, resulting in impedances in the thousands of ohms.

The moniker “contour mode” is used to differentiate these devices from two topologies which have successfully exploited the piezoelectric effect. Surface Acoustic Wave (SAW) and Bulk Acoustic Wave (BAW) systems have been successfully integrated in filters in military radios and personal hand-held communication devices [7].

SAW devices are based upon travelling acoustic waves near the surface of the active material, with exponentially decreasing amplitude into the thickness. They have met quite aggressive cost targets, showing excellent performance up to 2.5 GHz. Above this frequency, the challenges of achieving lithographic feature sizes less than 0.25 μm and compensating the temperature coefficient of frequency have limited this technologies growth [2]. SAW filters tend to have lower quality factors due to the one-dimensional energy confinement inherent to the topology, although recent designs have used Bragg type reflectors to boost quality factor.

Devices with high quality factors are highly desirable for several reasons. Filter roll-off is directly related to device quality factor. Guard bands – unused portions of the radio spectrum used to prevent interference between bands – are undesirable and may be minimized by utilizing filters with steep roll-off. With increasing demands for wider bandwidth, the RF spectrum has become a more crowded and coveted resource to be used most efficiently. Additionally, the insertion loss is related to the quality factor. Higher insertion loss results in higher current draw towards amplification of the filtered signal, and therefore lower battery life. The slow pace of battery life enhancement technology compared with increasing performance demands results in handset designers requesting ever more efficient radio components.

The answer to this problem came in the form of BAW resonators. Solidly mounted resonators (SMRs) and thin film bulk acoustic resonators (FBARs) are the commonly utilized topologies. They operate in the first harmonic of thickness-extension, which is a standing wave with well-confined acoustic energy showing Q s well over 2000 and a small package size relative to SAW filters. FBARs are released on the top and bottom

sides, while the SMRs are fabricated upon a Bragg reflector for acoustic energy confinement. Commercial devices are generally fabricated from aluminum nitride, and utilize the strongest piezoelectric constant of aluminum nitride, e_{33} , and have shown excellent insertion loss [8].

AlN FBARs currently meet the requirements of today's wireless standards. However, as it is a thickness mode, its resonant frequency is dictated by the film thickness, resulting in difficulties in fabricating and/or integrating these devices as filter banks. In more recent years, for logistical efficiency, phone manufacturers began to produce "international" phones capable of supporting 20+ LTE bands, and this number will only increase, exacerbating the problem of integrating many discrete filters. International phones are generally cheaper to design and manufacture, rather than the older model of designing a phone with filters specific to each market. Assuming one filter for uplink and downlink, the ability to monolithically fabricate filters of several frequencies on a single chip would result in significantly reduced size and improved manufacturability. Contour mode resonators (CMRs) have shown promise as an answer to the problem of the increasing number of filters.

The name "contour-mode" refers to the characteristic ability to define frequencies *lithographically*. Accordingly, a very wide range of resonator frequencies may be defined on the same chip [9], resulting in the ability to monolithically realize filter banks on a single chip. This can result in significant size reduction and increased integratability. This concept is also useful for military radios, which use frequency hopping techniques across a wide range of UHF frequencies. At the lower frequencies for military applications, these devices have shown large size advantages compared to

SAW devices along with frequency tunability capabilities [5]. These devices have shown low insertion loss and high quality factors across a wide range of frequencies [10, 3, 11]. Generally, contour mode resonators are fully released structures with anchors in the same plane as the thin film. This is in contrast to FBARs and SMRs, which are released by clamped on all sides in plane or solidly mounted, respectively.

1.1.1 Operating Principles

The direct piezoelectric effect is a physical phenomenon where electrical polarization changes in response to an applied mechanical stress. The indirect effect is the opposite: mechanical deformation occurs due to an applied electric field. When linearized, this effect is described by the linear piezoelectric constitutive equations, which are generally derived using thermodynamic arguments [12].

$$T = c_E \cdot S - e^t \cdot E \quad (1.1)$$

$$D = e \cdot S + \varepsilon_S \cdot E \quad (1.2)$$

Here T is the material stress, S is the material strain, D is the electric displacement, and E is the electric field, c is the matrix of stiffness coefficients, e is the matrix of piezoelectric coupling constants, and ε is the electric permittivity. The subscripts describe the field which should be held constant (preferably zero) when material properties are measured (e.g. c_E indicates the stiffness should be measured at constant-preferably zero-electric field). In many materials, the piezoelectric effect does not exist, and equations (1.1) and (1.2) reduce to Hooke's law and the electric displacement – electric field relationship. There are three other forms in which the constitutive equation may be written [13], and the form given here is referred to as the “stress-charge” form.

Some crystal classes only exhibit piezoelectricity after a mechanical load is applied, thereby creating the dipole moment. Other, more desirable crystal classes which support a spontaneous electric dipole moment with no applied field, an applied electric field may interact with the dipole moments to deform the crystal. These are of most interest due to their strong polarities, resulting stronger piezoelectricity, and the ease of not requiring an applied mechanical boundary condition, which can be difficult to reproduce consistently at the micro-scale.

This two-way transduction between the mechanical and electrical domains is the basis for piezoelectric filters and resonators. Electrical energy from an antenna is transduced in the mechanical domain by an interaction between the electric field shape and mechanical mode shape mediated by the piezoelectric coupling constants. This transduction will be discussed in more detail in later chapter. If the frequency of electrical signal is near a mechanical natural frequency, the energy is stored most efficiently. The mechanical energy is then transduced back to electrical energy via the direct piezoelectric effect. Since storage of mechanical energy is most efficient near mechanical resonances, it may be said that the electrical energy is filtered through the mechanical domain. The total amount of energy which passes through the resonator near a particular mechanical resonance is governed by the efficiency of stored energy to lost energy (the quality factor) and the efficacy of both transduction steps (the coupling). Coupling is not an efficiency, as it is a process of conversion, with all other energy assumed transmitted or reflected.

The energy converted from electrical-to-mechanical or vice-versa is measured by an electromechanical coupling factor, which measures the square root of the fraction of

the mechanical energy converted to electrical energy each cycle, or vice-versa [14]. Coupling and transduction are often used synonymously in this work. There is not “an” electromechanical coupling factor, as this fraction depends upon the orientation of the piezoelectric with respect to the electric field, and electrical and mechanical boundary conditions [14], and mode shape when discussing the coupling of modes. There are several “quasi-static” coupling factors, which are measured and valid at low frequencies. Definition are given in IRE standards [15], and the most commonly used ones given by

$$k_{15}^2 = \frac{e_{15}^2}{c_{44}^E \epsilon_1^T} \quad (1.3)$$

$$k_{33}^2 = \frac{e_{33}^2}{c_{33}^E \epsilon_3^T} \quad (1.4)$$

$$k_{31}^2 = \frac{e_{31}^2}{c_{11}^E \epsilon_3^T} \quad (1.5)$$

$$k_p^2 = \frac{e_{31}^2}{\sqrt{\frac{2}{c_{11}^E + s_{12}^E}} \epsilon_3^T} \quad (1.6)$$

$$k_t^2 = \frac{e_{33}^2}{c_{33}^D \epsilon_3^S} \quad (1.7)$$

These define the coupling for well-defined electric and mechanical fields which exist in plates, cylinders, or bars at low (quasi-static) frequency. They are useful for quantifying the strength of piezoelectric in various directions, as they set an upper limit for the coupling when an electric field optimally interacts with a strain field. They are also useful for comparing expected resonator performance for various materials when used properly. For example, k_{31}^2 represents the coupling between the electrical and

mechanical domains with a uniform electric field in the 3 direction coupling with a uniform extension in the 1 direction (this mechanical strain is not possible for a normal mode). However, these are defined only for piezoelectric devices with no electrodes or other elastic bodies interacting with the piezoelectric material. The addition of any non-piezoelectric material reduces the overall coupling.

The situation becomes more complicated when considering the interaction of the electric field with mechanical modes. The coupling is then dependent not only upon geometric and material properties, but also the mode shape. When considering a normal mode of a device, the strain will vary throughout the body of the resonator. It will be zero at certain points, and can take on both positive and negative values. Due to this non-uniform strain distribution, certain points in the resonator will not couple as well to an applied electric field *for a particular mode*. The same point in space may actually couple a large portion of energy into a different mode. Generally, this results in reduced overall coupling when compared to the “quasi-static” coupling factors. Real devices have non-piezoelectric material integrated in the stack, which require energy to strain, but do not contribute to transduction. Therefore, when discussing the electromechanical coupling of mechanical modes to electrical fields with spatially varying electric field/strain magnitudes, directions, and fractions of non-piezoelectric material, the situation becomes more complex. Each individual mode in a resonator is said to have an effective electromechanical coupling, k_{eff}^2 . The square comes from the fact that there are two transduction steps, electrical to mechanical, and mechanical back to electrical. The word “effective” is used because the stresses and strains that exist for each mode will interact in a unique way to the same applied electric field shape compared to any

other mode. k_{eff}^2 is an important performance parameter because it characterizes how well energy is transduced into and out of a specific mode, and it fundamentally sets the maximum bandwidth of a filter created from cascades of one port devices, and it partially determines insertion loss.

Another important metric is the quality factor, or Q , which was briefly mentioned earlier. Q is a measure of how efficiently energy is stored in the resonator each cycle, or alternatively, how little energy is lost each cycle. There are various quality factors associated with piezoelectric devices, which will be discussed in section 2.1.2. For now, we will only discuss the meaning in general terms and its importance to resonator performance. One definition of Q is

$$Q \equiv 2\pi \frac{\text{energy stored}}{\text{energy dissipated per cycle}} \quad (1.8)$$

The 2π allows the Q to be expressed in terms of only the coefficients of second-order differential equation which describes many simple resonant systems.

Q is also directly related to the sharpness of a mechanical resonance peak in the frequency domain, as well as the transmission of a signal. The Q will also have a direct effect on the steepness of the skirts of a filter. There are various sources of energy loss in piezoelectric MEMS resonator systems. They may be electrical in nature (e.g. ohmic losses from traces, dielectric loss), or mechanical in nature (e.g. viscous damping, thermo-elastic damping). An overview of the various important sources of loss is given in [16].

Since it is desirable to transduce as much energy as possible into and out of a targeted mode with the least amount of dissipation, it makes intuitive sense that a figure

of merit (FoM) would be the product of the coupling and the quality factor. Additionally, if one were to create a wide filter with low insertion loss and steep skirts, one would desire to create a high Q , high k_{eff}^2 resonator. The FoM is defined [17]

$$FoM \equiv \frac{k_{eff}^2 Q}{1 - k_{eff}^2} \quad (1.9)$$

This expression may be derived from energy arguments. Since the electromechanical coupling factor is defined as the electrical energy produced divided by the mechanical energy input, and Q_m is the mechanical energy stored (input) over the energy dissipated per cycle, the FoM may be produced by considering these quantities. This perspective of the FoM allows one to consider it the ratio of the total electrical produced divided by the mechanical energy dissipated. That is, electrical energy at the mechanical natural frequency is incident upon the resonator and is converted to mechanical energy. Some of this energy is dissipated, and the piezoelectric resonator then transduces the energy back to the electrical domain (the “produced” energy).

The metrics by which a piezoelectric resonators is judged have been discussed. Creating a resonator for radio frequency filtering from such a device is quite simple in concept. Electrodes are attached to a piezoelectric material in such a way that when one is assigned ground and the other signal, an electric field will be created that penetrates the piezoelectric. Applying harmonic signals near the mechanical natural frequency of a desired mode will apply a time varying stress approximately in 90 degrees out of phase with the stress already present in the resonators, resulting in enhanced energy storage determined by the resonator quality factor. Any resulting strain will in turn create a time

varying charge, or current, on the output port. In some cases, phenomena such as charge and/or strain cancellation may prevent the mode from being sensed/excited, respectively. For modes with appreciable Q and non-zero coupling, energy will be transmitted most effectively near mechanical resonances, as will be discussed in 2.1.2. The challenge in resonator design is maximizing the two quantities (Q_m and k_{eff}^2) simultaneously.

To create a filter, one or more resonators are used. The ladder configuration is a relatively simple topology for filtering built using one port resonators. For ladders, a minimum of two resonators are required, one of which is a series resonator and the other is shunt. The series admittances of the resonators are aligned as shown in Figure 1.2. In Figure 1.2, the shunt resonators have the parallel resonance (f_p) (frequency of highest impedance) close to the series resonance (f_s) (frequency of minimum impedance) of series resonators. When placed in the topology shown in Figure 1.1, the ideal filter has a response similar to Figure 1.3. This behavior can be understood as follows: away from the primary resonances, the response is primarily dictated by the capacitive response of the resonators. At the series resonance frequency of the shunt filter, the signal passed through the series filter has a low impedance to ground. At the parallel resonance frequency of the series filter, incoming signal sees a very high impedance. In between these two frequencies, the series resonator has very high admittance and the shunt resonator has very low admittance, creating the filter response. For increased rejection, the unit cells of Figure 1.1 may be cascaded at the expense of insertion loss. Other types of filters include balanced ladder filters and lattice filters.

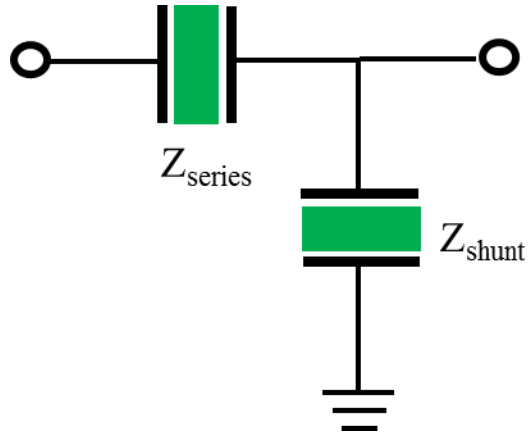


Figure 1.1 A unit cell of the ladder filter. These units may be cascaded to increase the rejection at the cost of insertion loss

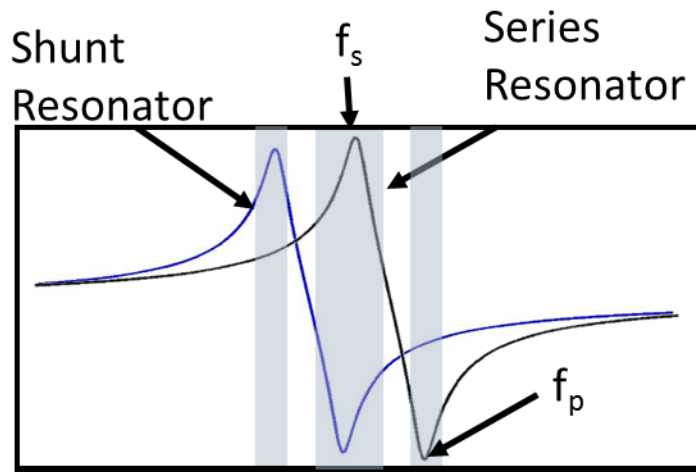


Figure 1.2 The series transmissions of the series and shunt resonators. At the peak transmission of the shunt resonator, a low impedance path to ground is provided, producing a notch. At the minimum transmission of the series resonator, the other notch is produced. In between these two frequencies, a large portion of the signal is transmitted

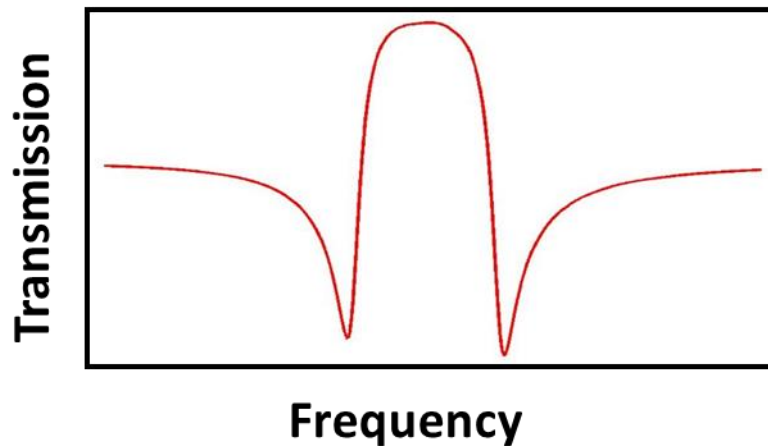


Figure 1.3 A qualitative illustration of the transmission response of a ladder filter.

1.1.2 Commonly Studied Modes

The term “Contour Mode Resonators” does not imply a specific mode as the term SAW, SMR, or FBAR does. There are a variety of modes in thin films for which lateral dimensions are the primary frequency determining dimension. This section will introduce common modes which have shown the highest performance

Length extension (also referred as beam extension) modes exist at frequencies below several hundred MHz, where at least one lateral dimension is much greater than the thickness [5, 18, 19]. These are sometimes considered one-dimensional, since energy is primarily stored in the strains in one dimension. The displacements of length extension harmonics are analytically described by cosine and sine harmonics. This mode is analyzed in more detail in section 2.2.5 . A closely related mode shape is width extension, in which the mode is designed to propagate in the width rather than length

[20]. The distinction between these modes is if the mode is propagating in the larger or smaller lateral dimension.

Another mode that has shown high frequency is the (1,1) harmonic of disk flexure. The numbers in parentheses denote the number of nodal lines and nodal circles, respectively that define them. The (1,1) mode has shown -1dB of loss in recent publications [3]. This mode is unique when compared to other high-performance devices in that its displacement is primarily out-of-plane-flexure. This mode is also discussed in more detail in section 2.2.5 .

At higher frequencies, where the resonator body thickness becomes comparable to the wavelength, extensional waves are no longer well described by the beam extension assumptions. Lamb's equations (often simply referred as "Lamb waves") describe the motion that occurs in this situation [21]. These modes may be thought of as a superposition of a purely longitudinal wave and a purely vertical-shear wave that recombine constructively at certain frequencies [22]. As such, they may no longer be treated as one-dimensional modes. There are symmetric (S_n) and anti-symmetric (A_n) modes, where the subscript n refers to the number of nodal planes. The S_0 mode has been of interest due to its coherent stresses and strains through the thickness, which results in higher coupling. The anti-symmetric modes are generally considered to be spurious. This is due to the fact that these modes generally have lower phase velocity, limiting their use towards higher frequencies, and lower effective coupling factors, limiting the bandwidth of filters composed of resonator utilizing these modes.

Lamb waves have no particle displacement in the plane perpendicular to the propagation direction and parallel to the major surfaces. Plate waves which do have this

characteristic are referred to as shear horizontal (SH) waves. These waves are complementary to Lamb waves, and together they describe all the waves that may propagate with a wave front of infinite depth in a plate. SH_0 based devices have been studied at higher frequencies and shown good performance [23].

Cross-sectional Lamé mode resonators have also recently been investigated as high frequency resonators in contour mode resonators [11]. These modes are isochoric, thus reducing losses from thermo-elastic damping [24]. Lamé modes have two significant directions of strain which are perpendicular to and parallel to the major film surface. In the contour mode resonators with interdigitated electrodes, this is exploited so that both the e_{31} and e_{33} are involved in coupling. Due to the two dimensional nature of the strain, these modes are more restricted in the resonance frequencies across which high performance devices may be fabricated on a single wafer. However, they are less restricted in frequency than FBARs.

1.1.3 State of the Technology

This section will briefly cover on the general performance and characteristics of CMR resonators including: frequency range, lowest attained losses, quality factors, and motional resistance.

Contour mode resonators have been fabricated with targeted modes ranging from 10's of MHz [5] to 10 GHz [25]. At low frequencies, parallel plate topologies dominate since mechanical wavelengths tend to be comparatively long, and favorable length-to-width ratio may be easily attained. When approaching the GHz range, interdigitated transducers (IDTs) are much more common. This is because the mechanical

wavelengths become shorter, generally on the same order of magnitude as the thickness of the thin film. The electrode area required to achieve a particular capacitance vs. wavelength requires utilizing higher harmonics in a single device, or multiple devices electrically in parallel.

Quality factor, an important performance metric when designing filters, varies across materials. Aluminum nitride and lithium niobate devices are reported with high quality factors generally between 1,000 to 2,000 [10]. PZT devices generally have lower Q closer to 200. Silicon is added to these devices to increase the quality factor [26]. While the quality factor is dependent on the amount of silicon relative to PZT, quality factors generally tend to be below 1,500.

The device impedance is important in determining the insertion loss as well as roll-off. Impedances as low as 3Ω in IDT topologies [26], and as low as 9Ω in parallel plate topologies [27] have been reported. For comparison, FBAR resonators typically have an impedance well below 1Ω . Ideally, the resonator impedance is zero near the mechanical resonance frequency.

In terms of coupling, the highest numbers that have been reported to date for k_{eff}^2 are around 4% [28] in aluminum nitride contour Lamé mode resonators. FBARs typically are in excess of 6.8% [8]. The Lamé mode resonators do not possess the coupling required to meet today's stringent RF front end requirements. Scandium doped aluminum nitride promises even higher coupling approaching double digits for FBARs [30].

Despite these performance metrics, CMR technology has not seen widespread adoption. Besides the coupling, one major reason for this is the spurious mode problem, which will be discussed in the next section.

1.2 Spurious Modes

1.2.1 Introduction to Spurious Modes

Any continuous elastic body is theoretically capable of supporting an infinite number of mechanical modes. While CMR devices are generally designed to excite only one mode, often the electric field shape is compatible with the modal strains of other modes, resulting in transduction of energy into and out of those modes. Such modes are called spurious modes. Depending on coupling and quality factor of the particular mode, this can appear as a large resonance in the frequency response. This kind of response is undesirable for several reasons. First, if significant spurious modes are within the passband of a filter, the group delay will be disrupted, therefore disrupting the filtered signal. Additionally, these spurs will increase the ripple of the passband. Ripple is a measure of the amplitude variation in the filter passband, which will result in distortion (Figure 1.4). Large out of band spurious modes can cause problems if the radio is placed near a high power antenna source. For military applications, this could be exploited to jam or damage radios.

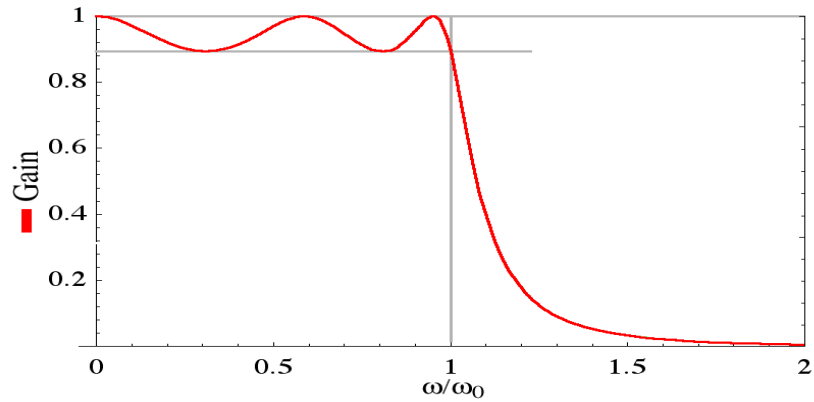


Figure 1.4 An example of ripple in the pass band [29]

1.2.2 The Spurious Mode Problem in FBARS

FBAR based filters are ubiquitous in consumer cellular handsets. However, before the commercial success, one of the biggest hurdles on the path to market was a problem with spurious modes [30]. FBARs have a very high aspect ratio, with the lateral dimensions being much greater than the thickness. Therefore, there are few, if any, modes propagating in the thickness near the fundamental thickness-extension modes. However, there are numerous plate waves propagating in the lateral dimension supported by this topology, namely various harmonics of Lamb modes [22]. In the practical design space, some harmonics of these modes can always propagate in the plates near the intended thickness-extension mode, degrading filter response. In a square plate, the sidewalls of the film provide a surface for these waves to reflect off of and constructively interfere. Any mode with approximately $\frac{Ln}{k} = i$ will resonate in this plate, where L is the plate length, k is the wave number of the fundamental harmonic, and n is the n^{th} harmonic, and i is any positive integer. If L is large compared to k , a large number of modes can be supported which will be spaced closely together in frequency. Real

devices require other considerations, but a similar idea holds true. The solution to this problem was to create non-parallel side walls in a process called apodization [31] (Figure 1.5). With non-parallel sides, the path length of any individual wave becomes very long before it returns to its starting state. The quantity of wave numbers that correspond to resonant waves now increases, and there may now be a situation more akin to a continuum of wave numbers rather than discrete well defined modes and frequencies. The energy is now “smeared” across frequencies, rather than primarily being stored at well-defined frequencies.

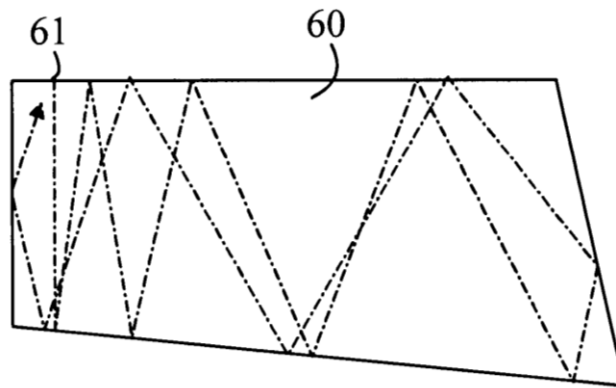


Figure 1.5 The path followed by the traveling wave of a spurious mode. Other spurious modes will have similarly long paths, increased the number of k vector and smearing the energy across these frequencies [31]

1.2.3 The Spurious Mode Problem in Contour Mode Resonators

Similar to FBARs, spurious modes are one of the largest obstacles on the road to widespread adoption of CMR technology. CMRs attracted attention due to the ability to lithographically define many frequencies on a single chip, a shortcoming of FBAR technology. However, this also creates challenges with regard to spurious modes. It is difficult for CMR designers to utilize lateral dimensions for spurious mode suppression without affecting the intended mode since CMR modes propagate in that direction.

Instead, the community has had to explore novel solutions to the various spurious modes that plague CMRs. These solutions include anchor design [32], electrode “apodization” [33], electrode design [34], and “mode conversion” techniques [35]. Not only this, but the FBAR community primarily investigated modes belonging to the Rayleigh-Lamb family. There is no commonly defined “CMR mode” as there is with FBAR; the CMR community has investigated modes in disks and rings [27, 1], beams [5], plate extensional modes [9], shear based modes [36], and Lamé modes [11]. While some of these topologies share types of spurious modes, there are some modes that are unique to each. Additionally, the spurious modes in CMRs tend to have wavelengths comparable to the resonators size and spaced further apart than FBAR spurs. This results in higher coupling and difficulty “blurring” the energy, respectively. The FBAR community was investigating Rayleigh-Lamb modes with wavelengths much shorter than the device size. This results in a large amount of current cancellation for these modes, and hence lower coupling. In contrast, piezoelectric MEMS devices generally have complex mode shape which are difficult to predict analytically, except for select simple cases.

Clearly, the community requires a generalized model to predict the severity of these spurs to inform design to mitigate their excitation and detection. This is one of the main impetuses of this work.

1.3 Common Piezoelectric Thin Films for Contour Mode Resonators

1.3.1 Introduction

Section 1.3 is intended to introduce the unfamiliar reader to the most commonly encountered piezoelectric materials in piezoelectric contour mode resonators. Extensive literature exists on the depositions, characterization, and integration of each of these materials. This work is primarily concerned with the use of these materials for resonator applications, and so these other subjects, if touched upon, will be done so lightly. For in-depth treatment, good starting points include the references in this section.

For comparison purposes, Table 1.1 includes typical values for the three most commonly encountered piezoelectrics for RF MEMS applications: lead zirconate titanate (PZT), aluminum nitride, and lithium niobate.

Table 1.1 A comparison of common thin film piezoelectric properties

	Relative Permittivity (ϵ_{33})	Density (kg/m^3)	Elastic Constants $\times 10^9$ (constant electric field)	$e_{31,f}$ (C/m^2)	d_{33} (pC/N)
PZT(53/47) [37]	1180-1650	7800	$Y_{11}=Y_{22} = 60.2$	-12 - -17	85
Aluminum Nitride [38]	10.7	3260	$C_{33} = 395,$ $C_{11}=345$	-1.05	3.92
Lithium Niobate (Z cut, 0° to +X axis [10])	29.16	4700	$C_{11}=C_{22}=C_{33}=203$		$e_{33}=1.33$

1.3.2 Aluminum Nitride (AlN)

Aluminum nitride based resonators have exhibited the highest contour resonator figure of merit (FoM) at frequencies above 500 MHz (147.7 at 725 MHz [11]), thanks in large part to the high quality factor of AlN (generally well over 2000). It exhibits excellent thermal conductivity for an electrical insulator, making it well suited for resonators handling a high power. Aluminum nitride is also quite stiff with low density, resulting in very high acoustic velocities, and therefore shorter wavelengths. The piezoelectric constants are lower than those of PZT (e_{31} -0.58 vs. -12 to -17 [39]), however the relative permittivity of AlN ranges from 9 to 10.7, two orders of magnitude lower than PZT (Table 1.1) [38]. Despite the lower piezoelectric constants, the low permittivity increases the achievable coupling due to the inverse proportionality of coupling with permittivity. One drawback is AlN devices must be larger than a comparable PZT device to achieve a desired shunt capacitance.

AlN has several processing advantages making it the most common piezoelectric MEMS resonator material when compared to the other two common piezoelectrics, PZT and lithium niobate. First, it is comparatively simple to obtain in thin film form via reactive magnetron sputtering and is highly reproducible [38]. Second, it is also more compatible with semiconductor-focused fabrications facilities, as it does not contain lead. Finally, the strong polar nature allows for highly oriented growth and, since it is not a ferroelectric piezoelectric, it does not face the aging challenges of PZT [38].

1.3.1 Lead Zirconate Titanate (PZT)

Lead Zirconate Titanate (PZT) is a ferroelectric with a successful history in bulk resonator applications due to its high piezoelectric constants [39]. PZT displays strong piezoelectric constants approximately one to two orders of magnitude greater than those of aluminum nitride, and as well as high coupling factors, with reported thin-film k_{31}^2 as high as 29.8% at low electric field [40]. However, due to its high mechanical loss and processing challenges in thin films, less interest has been shown in this piezoelectric material [39].

Ferroelectrics are subclass of piezoelectrics defined by the “reversibility in a polar crystal of the electric dipole by means of an applied electric field,” [14]. This polarizability exhibits hysteresis, as shown in the polarization-electric field graph in Figure 1.6.

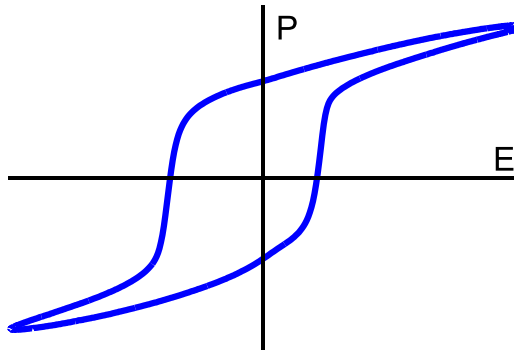


Figure 1.6 An example of the hysteretic response seen in ferroelectric materials. The polarization is a function of the applied electric field.

Two notable consequences arise from this with relation to device design. First, the piezoelectric constants vary with the voltage applied to the resonator. This effect is seen

in Figure 1.7, in which piezoelectric constants were extracted from cantilever test structures. Second, the dielectric constant is also modified by the applied electric field, which may be seen in Figure 1.8 in a capacitance vs. electric field chart for an unreleased capacitor. PZT has a very high relative permittivity of between 800-1200 at low oscillating and DC fields and at frequencies in the kHz range[39]. The variation of piezoelectric and dielectric constants with field will directly affect important resonator characteristics, such as the center frequency, coupling, and impedance. For this reason, PZT resonators are operated in a “small-AC-on-large-DC” condition, in which the radio signals are small, and the DC bias is applied to tune the operating conditions.

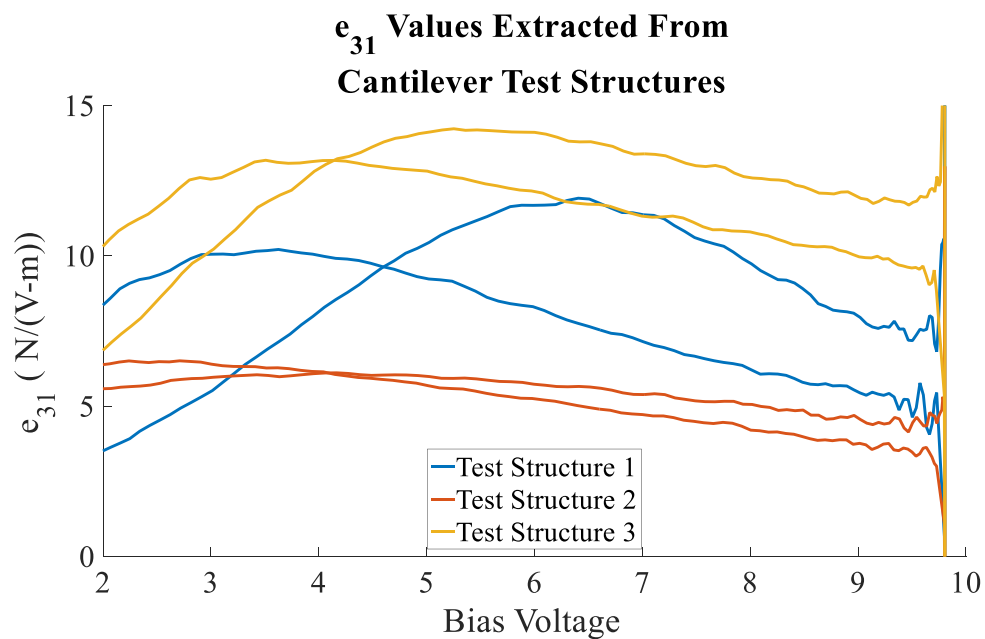


Figure 1.7 The piezoelectric constants extracted from cantilever test structures at various locations on a wafer. Not only do the constants vary as a function of voltage, they also varied as a function of location on the wafer.

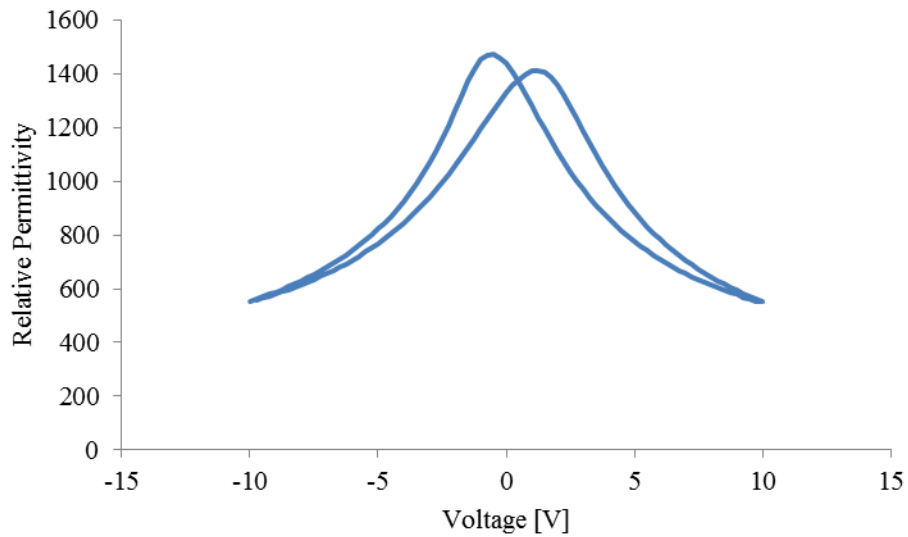


Figure 1.8 An example of the piezoelectric material's relative permittivity varying with the voltage applied to electrodes of a 0.5 μm thick film

Additionally, since ferroelectrics have at least two stable polarization states and PZT exhibits grains with distinct crystal orientations, regions exist with different polarizations and orientations within the same material. The orientations and interactions of these domains directly impact the macroscopic dielectric properties, piezoelectric properties, mechanical properties, and the losses. A detailed treatment is given in [41].

One important challenge when using ferroelectrics is the process of aging. In this process, the dielectric constants, dielectric loss, coupling factors, and resonant frequencies decrease constantly in log-time [14]. This makes ferroelectrics a poor choice for applications which require ultra-stable frequencies. This effect must also be considered when designing devices that will operate for long periods of time without re-poling.

To address the high mechanical loss, PZT-on-silicon technology has been developed [42, 37]. Silicon is a high quality factor material, and its addition increases the overall quality factor of the material. However, this comes at the expense of resonator k_{eff}^2 , although the FOM remains nearly constant across a wide range of thicknesses [39]. These enhanced Q s allow the use of resonators in filter topologies where the Q of PZT by itself would be too low, as filter roll-off is directly related the resonator Q .

1.3.2 Lithium Niobate

Lithium niobate is a highly anisotropic ferroelectric material with moderate piezoelectric constants and dielectric constants, and high quality factor. It is commonly utilized in SAW resonators. Lithium Niobate contour mode resonators have shown the highest FoM of contour mode resonators to date (280 at 500 MHz [4]), and have demonstrated quality factors up to 3000 [36] and electromechanical coupling factors above 20% [10]. The material properties of lithium niobate may be found in Table 1.1. Although lithium niobate is a ferroelectric, the coercive field tends to be so high that many MEMS resonator publications do not report a value.

Lithium niobate (LiNbO_3) is not easily deposited in thin film form, with most efforts failing to produce high quality single crystal lithium niobate on a wafer scale [36]. Instead, bulk lithium niobate is bonded to a handle wafer, and either processed via ion-slicing or mechanical polishing. Ion slicing involves bombarding the bulk material with H^+ or He^+ , creating defects at a desired depth, which are subsequently amplified under thermal conditions [43]. The resulting film is then polished down to reduce damage

effects [10]. Although these processing methods are time consuming and not easily scalable, there is one main advantage. The cut of lithium niobate may be chosen to optimally orient the strongest piezoelectric coefficients with the electric field, resulting in the high k_{eff}^2 demonstrated.

CHAPTER 2

MODELING PIEZOELECTRIC MEMS RESONATORS

2.1 The mBVD Model

Since the input and output signals from piezoelectric MEMS resonators are electrical in nature, it is possible to represent the entire system in terms of electrical components. The modified Butterworth van-Dyke (mBVD) model is a common lumped element circuit model preferred by designers for its simplicity and accuracy [44]. It reduces the complex distributed resonator system to lumped components which may be easily understood by a circuit designer with no background in piezoelectric MEMS operation. The following sections introduces the mBVD modeling technique and its relationship to modal analysis, and discusses the significance of the various components.

2.1.1 Modal Analysis

Before discussing the mBVD model, it important to discuss how distributed mechanical resonators can be “lumped,” or represented by simple mass-spring-damper systems. To understand this, the concepts of modal analysis are first discussed.

Modal analysis is concerned with the superposition of normal modes, and may be used to model low loss mechanical systems [45]. Normal modes in linear lossless systems have the property that all points in the system move in a sinusoidal pattern in time at a particular frequency with a fixed phase. Normal modes are linearly

independent and orthogonal, as the name implies. Mathematically, the inner product of non-identical modes is zero

$$\int_V u_p(x, y, z) \cdot u_q(x, y, z) dV = 0, p \neq q \quad (2.1)$$

Here, V is the volume of the resonant body, u is the displacement of the mode in spatial coordinates, and p and q are any two arbitrary positive integers corresponding to two arbitrary modes. Additionally, the strains of these normal modes are orthogonal as well. This arises from the fact that if the strain of normal mode A could be written as a linear combination of strain of two other modes, B and C, then a simple integration of the x, y, or z strain would show that mode A would also be a linear combination of modes B and C. This violates the property of a mode that it must be orthogonal to all other modes. Similar arguments apply to the shear strains.

Additionally, the general motion of an elastic body may be described by a superposition of all normal modes with appropriate magnitude. That is to say the motion of one mode is assumed to not affect the motion of any other modes.

$$u(x, y, z, t) = \sum_{p=1}^m \delta_p u_{n_p}(x, y, z) u_{t_p}(t) \quad (2.2)$$

Here u represents the general motion of a resonant body from an arbitrary excitation, u_{n_p} is the unity normalized mode shape of the p^{th} mode, δ_p is the contribution of the p^{th} mode to the frequency response and is a function of the excitation, and u_t is the temporal component of the p^{th} mode.

Therefore, the contribution of individual modes to the total energy may be analyzed. Since all points on the resonator body move at the same frequency and with the same phase for a particular mode, the total kinetic and potentially energies of each mode may be represented by a single, sinusoidal time varying quantity. This implies that a “modal” mass and spring may be defined relative to a point on the resonator. To find these modal properties, the energies of the distributed and lumped system are compared. To obtain the modal spring, the strain energy is compared to the energy stored in a linear lumped spring:

$$\frac{1}{2} \int_V \sigma \cdot S dV u_t^2 = \frac{1}{2} k_m \delta^2 u_t^2 \quad (2.3)$$

Here, σ and S are the six-dimensional compressed vector representation of stress and strain, respectively, in Voigt’s notation, k_m is the modal stiffness, and δ is the modal displacement. After choosing a proper point to track with δ (usually the point of maximum displacement of the distributed system), the modal stiffness may be derived.

To obtain the modal mass, the kinetic energies are compared

$$\frac{1}{2} \int_V \rho (\delta u_n u_t)^2 dV = \frac{1}{2} m_m (\delta \dot{u}_t)^2 \quad (2.4)$$

Where ρ the local density of the resonator, and m_m is is the modal mass.

Solving explicitly for the modal mass, modal spring, and modal damping gives

$$k_m = \int_V \mathbf{S}_n \cdot \mathbf{c} \cdot \mathbf{S}_n dV \quad (2.5)$$

$$m_m = \omega_n^2 \int_V \rho(x, y, z) u_n^2 dV \quad (2.6)$$

The modal mass and spring have been derived up to this point for an ideal lossless system. Systems with loss will experience a degree of coupling between modes, and the losses will alter the natural frequency [46]. However, for modes with low loss, these effects are negligible, and to good approximation the frequencies predicted by the modal mass and spring are the same as the frequencies of the lightly damped system. MEMS resonators often have Q in excess 1,000, well above the range where these effects are significant. The modal damping is given by

$$b_m = \frac{k_m}{Q_m \omega_n} = \frac{m_m \omega_n}{Q_m} \quad (2.7)$$

So far the lumped parameters for unforced vibration have been developed. The actuation from the indirect piezoelectric effect must be modeled as well. The forcing of the lumped system is performed by a “modal force”, F_m . This lumped force and the corresponding modal displacement represent work imparted to the system via piezoelectric stresses generating real strains in each mode. F_m had previously proven the most elusive portion of the problem to solve, as, unlike the other motional parameters, its magnitude is dependent upon the transduction efficacy as well as the mechanical and modal properties. It will be derived in section 2.2.3

Each normal mode will therefore have a unique modal force, mass, spring, and damper. This fully defines a forced, damped simple harmonic oscillator, and the basis for representing distributed mechanical systems as lumped mechanical elements has now been established.

2.1.2 Overview of mBVD

As mentioned previously, since the excitation and detection signals in RF piezoelectric MEMS resonators are both electrical in nature, the entire system may be represented as an equivalent electrical system. The commonly utilized modified Butterworth van-Dyke Model [44] is such a lumped-element mode (Figure 2.1). This representation is desirable due to the ease of use for circuit or filter designers [44]. The original Butterworth van-Dyke model contains only lossless components, and is an ideal resonator. The modified mBVD includes Ohmic, mechanical, and dielectric losses.

As discussed in section 2.1.1, the distributed resonant mechanical system, may be represented as a lumped mass-spring-damper system via modal analysis. These lumped mechanical parameters may in turn be represented as lumped electrical parameters through the inclusion of electromechanical coupling terms. After this transformation, the new elements are known as the “motional” capacitor (spring), inductor (mass), and resistance (damper). These are often abbreviated C_m , L_m , and R_m , respectively. These three parameters represent a single mechanical resonant mode, and their series combination is known as a “motional path.” Each motional parameter corresponds to a mechanical parameter, but with transduction incorporated to transform between the domains. This is similar to how the modal force models an applied stress. In later

chapters it will be shown that the electrical and associated mechanical quantities are directly or inversely proportional to each other, with a constant relating them determined by the electromechanical coupling.

For one port devices, the capacitor is placed in parallel with the motional path (Figure 2.1). This capacitor represents the real capacitance between the electrode of the port electrode and ground. It is inevitable that some energy will not be directly transduced to the mechanical domain, as some energy must remain in the electrical domain to create the electric field. As such, it can be inferred, and will later be discussed, how this capacitor is integral to determining the amount of energy coupled into the mechanical domain for a particular mode. Therefore, the motional parameters are indirectly a function of this capacitance.

Two port devices are represented by a slightly different arrangement (Figure 2.1b). The capacitors C_1 and C_2 represent the capacitance between the respective port electrode and ground. This is important, as each capacitance may be designed by changing the size of the electrode.

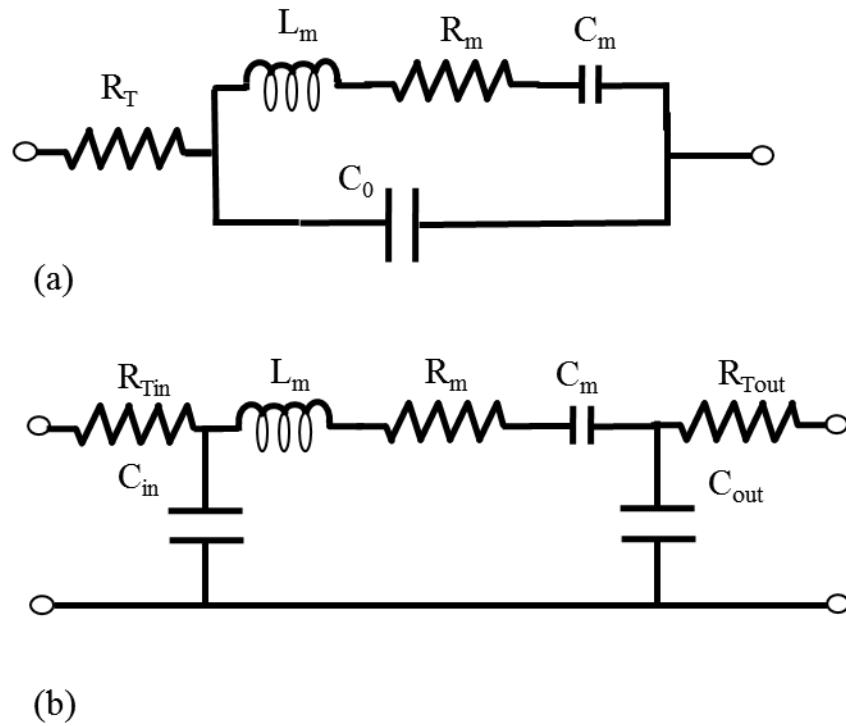


Figure 2.1 (a) The mBVD model for a one port resonator. (b) The mBVD adapted to model a two port resonator. Notice that in both cases, the only loss modeled is in the resonator

Figure 2.1a,b and represent a non-ideal resonator with tether resistances and mechanical loss. Often times there are other non-ideal parasitic resistances and capacitances. Figure 2.2a,b shows the mBVD with several parasitic components. First, the resistances placed immediately after the ports, R_T , represent the finite resistance of the routing to the device. Also, in some cases there may be a significant capacitance between the electrodes of a two-port resonator. In this case it is necessary to include a parasitic capacitor, C_p , in parallel with the motional arm. This capacitance is ideally zero, since the purpose of these devices is to filter the signal through a mechanical resonant response. A similar effect can occur in one-port devices in which, due to the fabrication process, the signal pad and ground plane can have significant capacitance.

This must be de-embedded to obtain the true performance of the device. The dielectric loss of the resonators is represented by the resistors R_b .

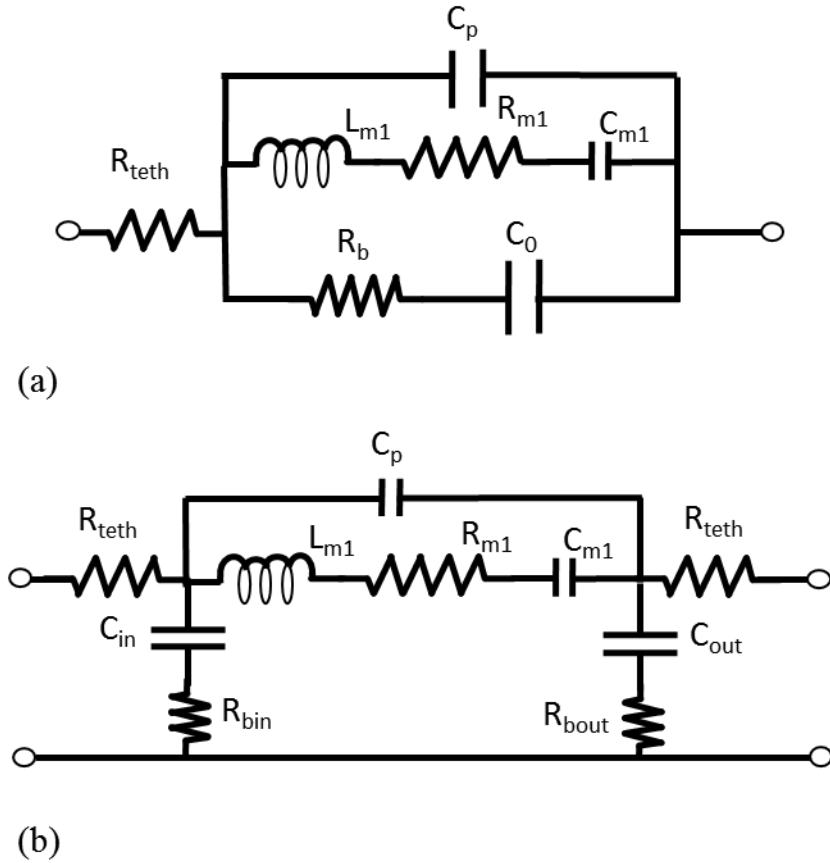


Figure 2.2 (a) The mBVD for a 1 port resonator with parasitic resistors and capacitors and (b) the mBVD of a two port resonator with parasitic resistors and capacitors.

When discussing the losses of a piezoelectric filter modeled by the mBVD, there are three important quality factors that are commonly presented. The first is the *mechanical* quality factor, Q_m , which as the name implies, represents losses in the mechanical domain.

$$Q_m = \frac{\sqrt{mk}}{b} = \sqrt{\frac{L_m}{C_m} \frac{1}{R_m}} \quad (2.8)$$

Where m , k , and b are the lumped equivalent mechanical elements from modal analysis, which were discussed in 2.1.1 .

For two-port resonators, the other two quality factors, the *loaded* and *unloaded* quality factors (Q_L and Q_U , respectively), incorporate the losses from mechanical and electrical effects, as well as the effect of coupling to an external load [47]. Q_U incorporate all mechanical and electrical loss sources between the two ports, including tether resistances, leaky capacitors, parasitic capacitances, and any factors which result in energy being dissipated or leaving the system through ground. Regarding Q_L , the resonator or filter circuit is connected to a load across which the output voltage is measured. The degree of coupling between the resonator and load alters the amount of energy leaving the circuit. A well-matched device will deliver more energy to the load, whereas a poorly matched device will have most of the energy reflected off the load. The well matched case would appear as a decrease in quality factor, since less energy is being stored in the resonator. This effect is incorporated into Q_L , which is the quality factor that may be directly extracted from S_{21} measurements. Q_U and Q_L are related for two port resonators by the expression [47]

$$Q_U = \frac{Q_L}{1 - \max|S_{21}|}$$

Where $\max|S_{21}|$ is the maximum amplitude of the 2-1 scattering-parameters in dB at electrical resonance. Q_U is often of more interest than Q_L because it contains information about loss mechanisms intrinsic to the resonator.

The mBVD allows designers a convenient expression for the electromechanical coupling, k_{eff}^2 , previously discussed in 1.1.1 .

$$k_{eff}^2 = \frac{C_m}{C_0 + C_m} \quad (2.9)$$

As stated previously, this performance metric informs designers how well energy couples into a particular mode, and is therefore important to model.

2.1.3 Optimal mBVD Values

Although designers of piezoelectric resonators must often deal with real world issues, it is useful to discuss ideal mBVD performance in the context of how the non-ideal situation will affect them. These issues, such as finite metal resistances, parasitic capacitances, and leaky capacitors, can require the inclusion of additional elements, such as the aforementioned parasitic capacitance between electrodes of a two-port resonator.

For a 50Ω terminated two-port device, the shunt capacitance is ideally approximately 50Ω . The magnitude of S_{21} as a function of the mBVD of Figure 2.2b is given by [48]

$$|S_{21}| = \left| \frac{2}{2 + \frac{Z_M}{Z_L} + \frac{2Z_L}{Z_S} + \frac{2Z_M}{Z_S} + \frac{Z_L Z_M}{Z_S^2} + R_T \beta} \right| \quad (2.10)$$

$$\beta = \frac{4Z_S + 2Z_M}{Z_S^2} + \frac{2R_T Z_S + Z_M R_T + 2Z_M Z_S + 2Z_S^2}{Z_L Z_S^2} \quad (2.11)$$

Where Z_m is the the total impedance of the motional path, Z_L is the load impedance, and Z_S is the total shunt impedance. The mBVD is assumed symmetric in this case.

Routing resistances are represented in Figure 2.2b by R_T . Ideally, routing resistances are zero. These resistances have been shown to be significant contributors

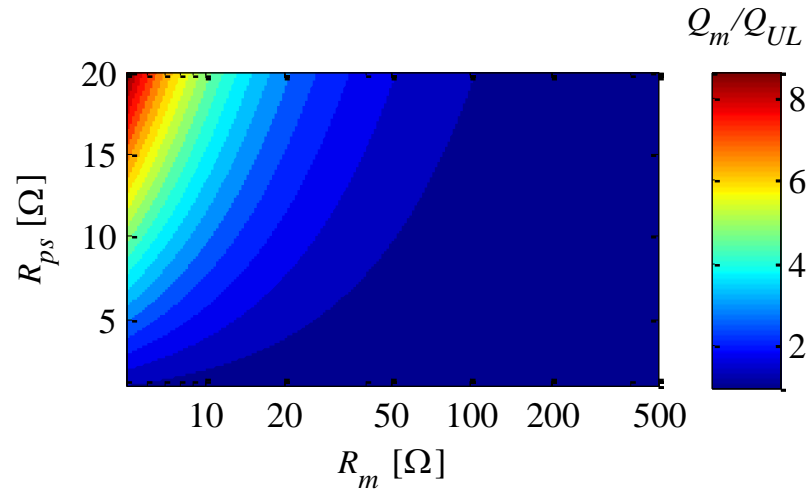


Figure 2.3 At low values of R_m , the additions of small tether resistance can have a dramatic effect upon the unloaded quality factor, and therefore loss, of the entire resonant system.

to the losses of piezoelectric MEMS resonators [48]. Even a few ohms of resistance can cause significant drops in the transmitted power for devices with low motional resistance. This is shown in Figure 2.3, where the shunt impedance is fixed to 50 Ω , and the ratio of the Q_m to Q_U is explored for various R_m and R_T .

Designers may include gold traces to reduce the resistance and improve the performance of their devices. However, gold is a low quality factor material factor, and the benefits of this must be weighed against the decrease in Q .

A naïve observer may suggest after looking at the two port mBVD may suggest that the shunt capacitance should be zero, so all transmitted energy passes only through the mechanical system. However, this would result in zero electric field through the piezoelectric layer, leading to zero stress generation, and therefore infinite R_m . Therefore, all incident energy would be totally reflected. This is the intuition for the fact mentioned earlier that the motional parameters of the mBVD are indirectly a function of the capacitance. This reasoning leads to the conclusion that there must be some shunt capacitance for transduction to the mechanical domain to occur, and the optimal value for a given termination and coupling should be analyzed.

Ideally, the motional resistance is zero as well. This is equivalent to stating that ideally there are no mechanical losses or the mechanical quality factor is infinite. This brings up an important distinction between Q_m and Q_U . Even with a perfect mechanical system with infinite Q_m , any electrical losses will result in a circuit Q_u which is finite.

2.1.4 Modifying the mBVD to Model Multiple Acoustic Modes

As previously stated mechanical systems modeled as linear, distributed, and can theoretically support infinite modes which are linearly independent. The general motion of such a system is a weighted, linear superposition of each of these modes. Energy is transduced to these modes through an electric field with identical shape across frequencies. In the mBVD, this means that each motional path is exposed to the same voltage. The motional parameters are determined partially by the mechanical lumped representations, as well as the coupling, which is reciprocal, i.e. the motional parameters are not affected by whichever port is the input and output, so $S_{21} = S_{12}$. Via the direct piezoelectric effect, energy is transduced back to electrical domain. All modes share a common output electrode, and therefore they must share a common node in the mBVD. At the resonance of a particular mode, the impedance of the corresponding motional path must be low, while all other motional paths should be generally (much) higher. These observations lead to the conclusion that an appropriate representation of multiple mechanical modes is to place each motional path in parallel Figure 2.4.

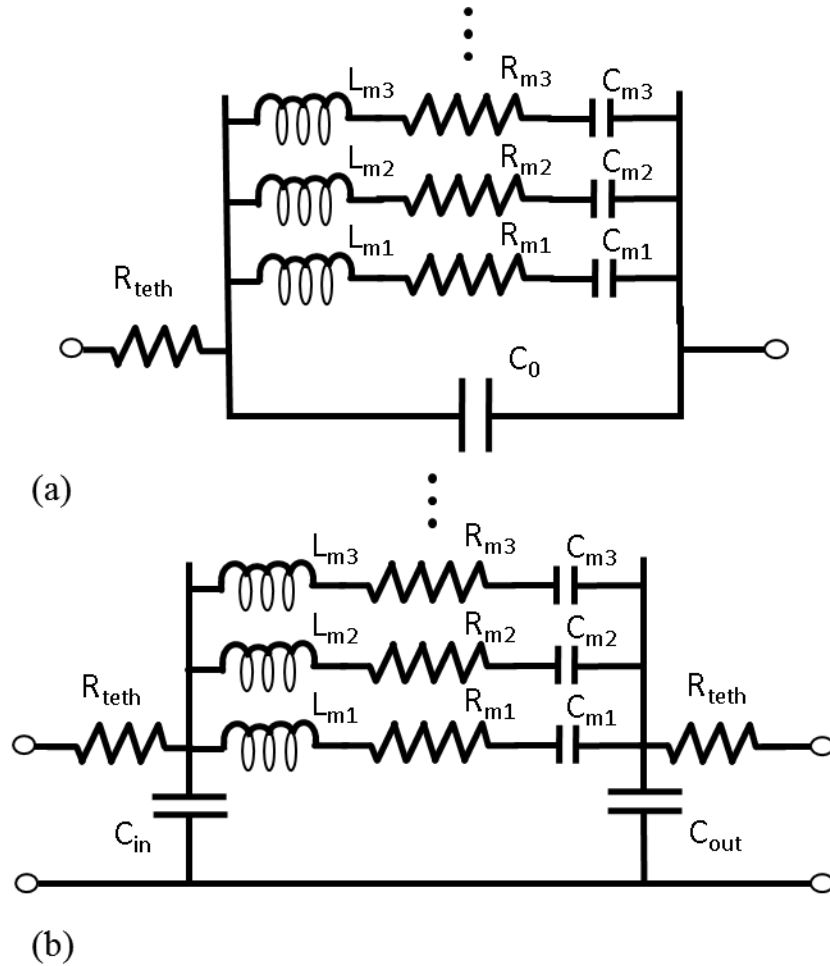


Figure 2.4 The mBVD model to modeling the response when the effect of several modes are included for (a) a one port resonator and (b) a two port resonator.

To analytically simulate the frequency response of a two port resonator, the most convenient method is to first convert to ABCD microwave network parameters [49], then convert once again to the desired network (usually scattering-, impedance-, or admittance-parameters). The impedance parameters of one port resonators are trivial to calculate.

2.2 The Motional Resistance

2.2.1 Introduction

Of all the parameters of the mBVD, the motional resistance has proven the most difficult to model, as well as the most important. The importance of R_m lies in the fact that, at mechanical resonance, R_m is the only motional parameter in the motional path, as L_m and C_m cancel out. The R_m is also the only parameter depending upon Q_m , which has proven notoriously difficult to model accurately. This means, disregarding parasitic capacitances, all transmitted energy for two-port resonators and desired filtered energy for one-port resonators passes through this loss mechanism. Therefore, the ability to predict performance and loss of a device before fabrication depends upon knowing the value of R_m .

Previously, the derivation of a generalized modal force was a challenge on the path to fully generalized expression for the motional parameters. As mentioned in 2.1.1, F_m , along with the output charge, is important in the fact that it depends not only upon the mechanical, modal, and material properties, but also upon the electric field. Without a modal force, the conversion of electrical to mechanical energy is not known.

2.2.2 Previous Efforts

Previously, there had been few efforts to derive a closed form expression for R_m . One excellent work analyzing piezoelectric ultrasonic motors provided useful sense and drive differential equations, which agree with expression presented later in this work with certain assumptions applied [50]. Other efforts mainly focused upon simple, one-dimensional modes. Both [18] and [51] included derivations for length/width extension

modes of two port resonators. These modes are both analytically described by harmonics of cosine. The terms “length” and “width” are used to specify if the mode is propagating primarily in larger or smaller dimension of a rectangular plate. From [18], the motional resistance expression is

$$R_m = \frac{n\pi(t_{si} + t_p)\sqrt{Y_c\rho_c}}{2e_{31}^2 w_{tot} Q_m} \frac{1}{\sin^2\left(\frac{n\pi L_e}{2L}\right)} \quad (2.12)$$

Where n is the harmonic, t_{si} is the thickness of the silicon, t_p is the thickness of the piezoelectric, Y_c is the composite modulus, ρ_c is the composite modulus, w_{tot} is the total width, Q_m is the mechanical quality factor, L_e is the length of the electrode, and L is the total length of the resonator. This expression is valid for the topology of Figure 2.5(a).

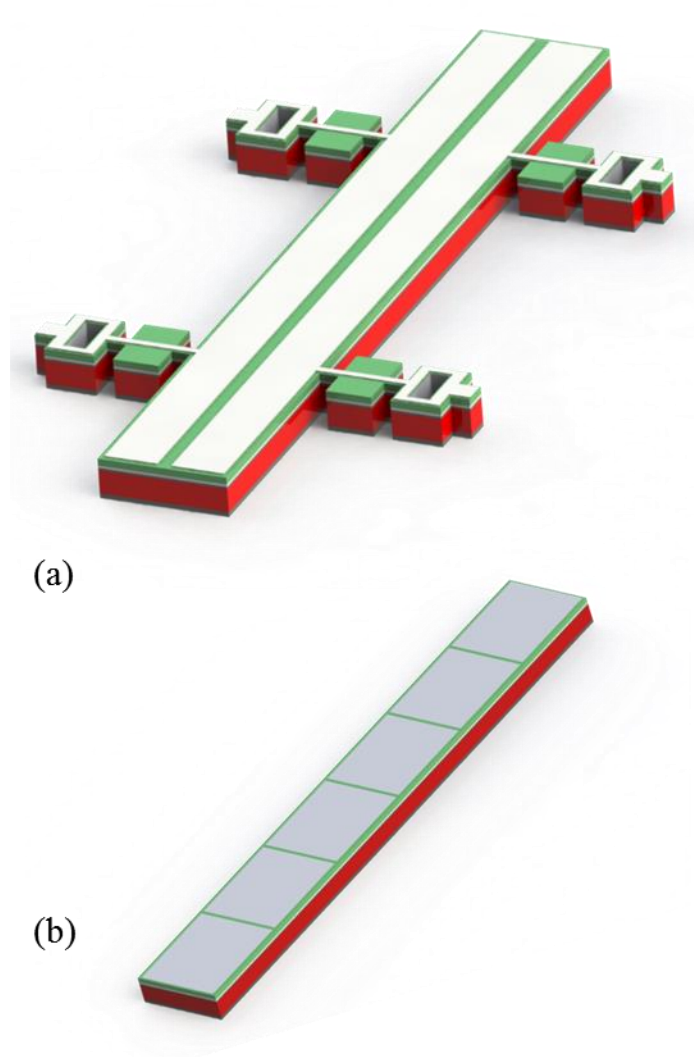


Figure 2.5 (a) The “full-length half-width electrode topology and (b) the “alternating electrode” topology. Each electrode section alternates connections to the first and second port.

The units are ohms, and the expression agrees with expression presented later in this work after applying simplifications. However, (2.12) is only presented for a two layer stack and assumes the electrodes are symmetric.

An expression for extensional modes with an “alternating electrode” topology (Figure 2.5b) from [51] is

$$R_m = \frac{n_{in} + n_{out}}{n_{in}n_{out}} \frac{\pi t_p \sqrt{Y_c \rho_c}}{8w_{tot} Q_m e_{31}} \quad (2.13)$$

Where n_{in} is the number of input electrodes and n_{out} is the number of output electrodes. This is the expression as presented in the work, however the units do not work out to ohms. This is likely a typo, as the problem is solved if the e_{31} is squared in (2.13). This expression is subject to similar limitations as the previous equation.

2.2.3 Derivation of the Generalized Motional Resistance, Capacitance, Inductance, and Electromechanical Coupling

The modeling methodology in the following sections employ comparisons of energy in lumped and distributed systems to arrive at a generalized expression for the motional resistance. The derivation is material, mode, and topology agnostic. It is therefore applicable to many systems. A generalized modal force, spring, mass, and capacitor are derived dependent on the strain fields, electric fields, geometric properties, and material properties. The modal force is obtained by comparing the work done by a force applied to a linear spring to the strain energy induced by an applied electric field through the piezoelectric material. The modal spring and mass are obtained by comparing the total modal mechanical energies of the fabricated system with the energy of the lumped mass-spring system, which is a precept of modal analysis. The charge due to the piezoelectric effect, and therefore current, on the output electrode is obtained by comparing the energy stored in a lumped capacitor with the energy stored by the induced dielectric displacement in the piezoelectric layer. A transfer function using these elements may be used to go from applied voltage to induced strain and finally to output current, or in other words, the motional resistance.

$$R_m = \frac{\Phi_{in}}{F_m} \cdot \frac{F_m}{\delta} \cdot \frac{\delta}{sQ_{out}} \quad (2.14)$$

Where Φ_{in} is the input voltage magnitude, δ is the quasi-static displacement magnitude, and Q_{out} is the charge out.

Modal analysis (section 2.1.1) allows the consideration of one mode, and the displacement of that mode may be written as a product of the time and spatially dependent components. It may therefore be expressed as

$$\mathbf{u}_q = \delta_q \mathbf{u}_{n_q} u_{t_q} \quad (2.15)$$

Where u_n is the unity normalized mode shape, δ is the zero-frequency displacement amplitude as well as the modal displacement of the lumped parameter system, and u_t is the temporal and frequency portion of the response. The variable q will be used to denote the fact that a single, arbitrary mode is being analyzed. This means the derivation is applicable to any mode, and specific expression for displacements and strains may be substituted in to obtain an expression for the mode under consideration. (2.15) describes the motion of any mode which is linear and orthogonal to other modes.

The zero-frequency displacement can arbitrarily be chosen to be any point on the resonator, and for this derivation is chosen to be the point of maximum displacement of the mode under analysis. u_t is the frequency response given by

$$u_{q_t}(t) = \frac{e^{j\omega t}}{\left[\left(1 - \left(\frac{\omega}{\omega_{n_q}} \right)^2 \right) + \frac{j\omega}{\omega_{n_q} Q_{m_q}} \right]} \quad (2.16)$$

Where ω is the excitation frequency, ω_{n_q} is the natural frequency of the q^{th} mode, and Q_{m_q} is the mechanical quality factor.

To obtain the modal force, the strain energy created by the applied electric field is compared to the strain energy of a forced spring under quasi-static conditions. This energy is sometimes referred to as the mutual energy, since it arises from electromechanical interactions. This energy may be expressed as

$$PE = \frac{1}{2} \int_V \mathbf{T} \cdot \mathbf{S} dV \quad (2.17)$$

Where T and S are the six dimensional condensed vector representations of stress and strain respectively in Voigt's notation, V is the volume of the resonator, and k_m is the modal spring, as obtained by the method of [52]. The stress in the piezoelectric may be obtained from the stress-charge form of the indirect effect piezoelectric constitutive equation [14]

$$\mathbf{T} = \mathbf{c}_E \cdot \mathbf{S} - \mathbf{e}^t \cdot \mathbf{E} \quad (2.18)$$

Here, c_E is the stiffness matrix at constant (zero) electric field, e is the matrix of piezoelectric stress constants, and E is the electric field. Of interest is additional energy introduced into the system from the applied electric field. The stiffness-strain term in (2.18) accounts for stress in the system before a change in electric field, and is therefore ignored, and the total energy in the resonator from the piezoelectrically applied stress is

$$PE_{total} = \frac{1}{2} \int_V \mathbf{T}_p \cdot \mathbf{S}_{real} dV \quad (2.19)$$

Where T_p is the total piezoelectric stress generated by the piezoelectric material when completely free, and S is the real strain of the resonator from the contribution of all modes.

The contribution of the applied piezoelectric stress to the strain of each mode may be found via mode superposition. The real strain due to the applied stress may be expressed as a superposition of all the individual real strains of each mode, S_q

$$S_{real} = \sum_{q=1}^{\infty} S_q \quad (2.20)$$

The real strain energy may then be written

$$PE_{total} = \frac{1}{2} \int_V \left(T_p \cdot \sum_{q=1}^{\infty} S_q \right) dV \quad (2.21)$$

Where T_p is the applied piezoelectric stress. Distributing the piezoelectric to stress shows that the energy of each mode from the applied piezoelectric stress is simply a dot product of the applied piezoelectric stress and the strain of that mode

$$PE_q = \frac{1}{2} \int_V (T_p \cdot S_q) dV \quad (2.22)$$

Now placing (2.18) with the first term ignored into (2.21) and comparing this to the energy stored in a lumped spring with an applied force gives

$$F_{m_q} \delta_q = - \int_V \mathbf{e}^t \cdot \mathbf{E}_{app} \cdot \delta_q \mathbf{S}_{n_q} dV \quad (2.23)$$

Where F_{m_q} is the modal force, S_{n_q} is the strain from the unity normalized mode shape of the q^{th} mode, and E_{app} is the applied electric field. The $\delta_q S_{n_q}$ product is the real strain of the analyzed mode. The first term of (2.21) is dropped since this term accounts for strain energy in the system not directly attributable to the applied force. Under quasi-static conditions, any strain energy in the resonator is directly attributable to piezoelectric work. The general modal force may be written

$$F_{m_q} = k_{m_q} \delta_q = - \int_{V_{in}} \mathbf{e}^t \cdot \mathbf{E}_{app} \cdot \mathbf{S}_{n_q} dV \quad (2.24)$$

The displacement caused by this modal force is then

$$\delta_q = \frac{F_{m_q}}{k_{m_q}} = - \frac{\int_V \mathbf{e}^t \cdot \mathbf{E}_{app} \cdot \mathbf{S}_{n_q} dV}{k_{m_q}} \quad (2.25)$$

For later convenience, may be rewritten with the applied voltage explicitly stated

$$\delta_q = \frac{F_{m_q}}{k_{m_q}} = - \frac{\Phi_{in} \int_V \mathbf{e}^t \cdot \nabla \phi_{in} \cdot \mathbf{S}_{n_q} dV}{k_{m_q}} \quad (2.26)$$

Where Φ_{in} is the magnitude of the applied voltage, and ϕ_{in} is the unity normalized electric potential field from the input capacitor, with the ground at 0 potential and the input electrode at a potential of 1. Note that the electric field is not a function of the mode shape.

The real strain may now be expressed as

$$\mathcal{S}_q = \delta_q \mathcal{S}_{n_q} u_{t_q} = - \frac{\Phi_{in} \int_V \mathbf{e}^t \cdot \nabla \phi_{in} \cdot \mathcal{S}_{n_q} dV}{k_{m_q}} \mathcal{S}_{n_q} u_{t_q} \quad (2.27)$$

This may be placed in the direct effect equation of the stress-charge form of the piezoelectric constitutive equation

$$\mathbf{D} = \mathbf{e} \cdot \mathbf{S} + \epsilon_S \cdot \mathbf{E} \quad (2.28)$$

Where D is the induced electric displacement in the piezoelectric layer. The permittivity-electric field term account for electric displacement already present across the physical output capacitor from purely dielectric effects. The concern is with additional electric displacement generated by the piezoelectric effect, and so the second term is ignored. The energy stored by the direct effect is compared to the energy stored in a “modal” capacitor. The term modal is used here to indicate that the magnitude of the capacitance depends directly on the modal strain. This capacitance, however, is not directly calculated, and instead the energy is computed using the modal charge and the electric field across the capacitor.

$$\frac{1}{2} \int_V \mathbf{D}_p \cdot \mathbf{E}_{out_q} dV = \frac{1}{2} Q_{out_q} \Phi_{out_q} \quad (2.29)$$

Where D_p is the electric displacement from the piezoelectric effect, E_{out} is the resulting electric field on the output electrode, Q_{out} is the charge on the output capacitor, and Φ_{out} is the magnitude of the voltage across the output port. After writing the electric field once again as the unity normalized potential and voltage magnitude, the charge on the output port may now be written

$$Q_{out_q} = \int_V \mathbf{e} \cdot \delta_q \mathbf{S}_{n_q} \cdot \nabla \phi_{out} dV \quad (2.30)$$

Now substituting (2.26) into (2.30) returns an expression for the charge on the output port dependent upon modal properties, geometry, and material properties only

$$Q_{out_q} = \frac{\Phi_{in} \int_V \mathbf{e}^t \cdot \nabla \phi_{in} \cdot \mathbf{S}_{n_q} dV \int_V \mathbf{e}^t \cdot \nabla \phi_{out} \cdot \mathbf{S}_{n_q} dV u_t}{k_{m_q}} \quad (2.31)$$

Taking a time derivative and setting the frequency to the natural frequency of the q^{th} mode, an expression for the current out of the resonator is obtained

$$I_{out_q} = \frac{Q_{m_q} \omega_{n_q} \Phi_{in} \int_V \mathbf{e}^t \cdot \nabla \phi_{in} \cdot \mathbf{S}_{n_q} dV \int_V \mathbf{e}^t \cdot \nabla \phi_{out} \cdot \mathbf{S}_{n_q} dV}{k_{m_q}} u_t \quad (2.32)$$

Reorganizing to obtain Φ_{in}/I_{out} and taking the magnitude returns the motional resistance

$$R_{m_q} = \frac{k_{m_q}}{Q_{m_q} \omega_{n_q} \int_V \mathbf{e}^t \cdot \nabla \phi_{in} \cdot \mathbf{S}_{n_q} dV \int_V \mathbf{e}^{\square} \cdot \nabla \phi_{out} \cdot \mathbf{S}_{n_q} dV} \quad (2.33)$$

This is the most general form of the motional resistance, and is valid for any topology, material, or mode, provided all assumptions have been met. It is valid for 1- and 2-port resonators. For a 1-port resonators, the electric potential fields are equal. This expression contains phase information for two port resonators, and therefore may be positive or negative. This arises from the fact that the charge produced on the second port may be positive or negative depending on the electrode location and mode shape, and hence there will be a 180 degree phase shift for some modes. This fact which must

be taken into account when utilizing this expression to obtain the frequency response including several modes, as charge cancellation can occur. Note that with parallel plate topology (i.e. $\nabla\phi = 1/t_{piezo}$, the thickness of the piezoelectric), (2.33) reduces to

$$R_{m_q} = \frac{k_{m_q}}{Q_{m_q} \omega_{n_q} \int_{A_{el1}} \mathbf{e}^t \cdot \bar{\mathbf{S}}_{n_q} dV \int_{A_{el2}} \mathbf{e}^t \cdot \bar{\mathbf{S}}_{n_q} dV} \quad (2.34)$$

Here, A_{el} is the area of an electrode, and $\bar{\mathbf{S}}_n$ is the strain from the unity normalized mode shape averaged through the thickness of the piezoelectric layer.

Since R_m is implicitly a quantity belonging to a single mode, the q will be dropped henceforth.

From (2.8), the mechanical quality factor relationship, the motional inductance and capacitance may be easily obtained.

$$L_m = \frac{m_m}{\int_V \mathbf{e}^t \cdot \nabla\phi_{in} \cdot \mathbf{S}_n dV \int_V \mathbf{e}^t \cdot \nabla\phi_{out} \cdot \mathbf{S}_n dV} \quad (2.35)$$

$$C_m = \frac{\int_V \mathbf{e}^t \cdot \nabla\phi_{in} \cdot \mathbf{S}_n dV \int_V \mathbf{e}^t \cdot \nabla\phi_{out} \cdot \mathbf{S}_n dV}{k_m} \quad (2.36)$$

The equation for C_m may be used in the electromechanical coupling factor equation to obtain an expression for k_{eff}^2 dependent upon geometry, material properties, and mode shape

$$k_{eff}^2 = \frac{1}{\frac{C_0}{C_m} + 1} = \frac{1}{\frac{\int_V c^E S_n^2 dV \int_V \varepsilon (\nabla\phi)^2 dV}{\int_V \mathbf{e}^t \cdot \nabla\phi_{in} \cdot \mathbf{S}_n dV \int_V \mathbf{e}^t \cdot \nabla\phi_{out} \cdot \mathbf{S}_n dV} + 1}} \quad (2.37)$$

Where C_0 is the shunt capacitance for a 1 port resonator, or the equivalent capacitance of C_{in} and C_{out} (Figure 2.4) when placed in series to create an equivalent 1-port resonator as in [53].

Note that the R_m , L_m and C_m and k_{eff}^2 equations are all symmetric. For two-port resonators, it does not matter on which electrode the excitation stimulus is placed or the resulting signal is detected. This is important, since the resonator is a passive, reciprocal component.

The derived equations for R_m and C_m provide important insight into how to identify modes which may have high performance. To understand how, the relationship between the shared integral of (2.34), (2.35), (2.36), and (2.37) and the modal stiffness must be considered.

$$\int_V \mathbf{e}^t \cdot \nabla \phi \cdot \mathbf{S}_n dV \quad (2.38)$$

(2.38) is a measure of transduction, and a higher value lowers R_m and increases C_m . It is maximized by having highly compatible mode and electric field shapes, and using modes with significant coupling from more than one piezoelectric constant. This agrees with a common observation from piezoelectric MEMS papers that utilizing more than one piezoelectric coefficient often leads to higher performance [11, 35, 36]. Interestingly, shear cannot be coupled to the integral of (15) for the thin film PZT and aluminum nitride, even if it physically exists in the mode shape. This is because PZT and aluminum nitride with the poled axis and electric field in the 3 direction do not have the piezoelectric constants to transduce shear. More generally, any piezoelectric

material will have certain strain components it cannot transduce directly. However, when modal stiffness is calculated, *all* components of stress and strain are represented. If a mechanical mode stores most of the strain energy in strain components which are not directly transduced, the mode will have high motional stiffness compared to the total coupling, low transduction, and therefore higher R_m and lower C_m , even if it transduces into multiple strain components. From (17), C_m is directly related to k_{eff}^2 . For maximum k_{eff}^2 , C_m must be maximized relative to C_0 . Therefore, it is not enough that the resonator simply use more than one piezoelectric coefficient to obtain a larger value of the transduction integral for a low R_m and high C_m . A more precise statement is that energy must be directly transduced into and out of strain components which store a majority of the mechanical energy for minimized R_m and maximized C_m . To this end, computational aide may be enlisted to quickly identify modes with high k_{eff}^2 (independent of Q_m) and potentially low R_m , which is dependent on Q_m .

2.2.4 Alternative Derivation of the Motional Resistance

In this section, the derivation of the motional parameters is performed via a distinct technique to that of the previous section. The same assumptions apply to this derivation as the previous derivations.

The quasi-static total internal energy of a system may be written [54]

$$U = U_c + 2U_m + 2U_d \quad (2.39)$$

Where

$$U_e = \frac{1}{2} \int_V \mathbf{S} \cdot \mathbf{c}^E \cdot \mathbf{S} dV \quad (2.40)$$

$$U_m = \frac{1}{2} \int_V \mathbf{e}^t \cdot \Phi \nabla \phi \cdot \mathbf{S} dV \quad (2.41)$$

$$U_d = \frac{1}{2} \Phi^2 \int_V (\nabla \phi) \cdot \epsilon^T \cdot (\nabla \phi) dV \quad (2.42)$$

S is the real strain written in six-dimensional vector notation, c^E is the stiffness matrix at constant electric field, Φ is the magnitude of the applied voltage, ϕ is the unity normalized potential field, ϵ^T is the permittivity at constant field, and V is the volume of the resonator (although the integral is only nonzero in the piezoelectric). U_e is the purely elastic energy in the resonator, U_d is the purely dielectric energy, and U_m is the mutual energy, which corresponds to energy transduced from piezoelectric activity.

The derivation is performed in the quasi-static case in which a voltage is applied to the electrodes of a completely free resonator. The frequency dependent equations may be generated by multiplying the relevant expressions by (2.16).

In the quasi-static case, the mutual energy is now understood to account for both the mechanical potential energy stored from the displacement/strain of the beam and the additional charge that is stored on the electrode due to the increased polarization caused by the displacement. U_e is zero, and U_d represents the energy that is stored purely from dielectric effects, and is accounted for by the shunt capacitor in the mBVD. Therefore, only the mutual energy is considered. From similar arguments in the previous section, the energy of each mode may be considered independently, and therefore expressions

from henceforth will be understood to apply to a single, arbitrary mode. The mutual energy is then modeled by a lumped modal spring with an applied modal force (to represent the electric field causing a displacement) *and* a lumped modal capacitor with an applied voltage (to represent the additional charge stored from the increase in polarization caused by displacement) storing equal amounts of energy. The energy from these lumped parameters is equated to the mutual energy

$$\frac{1}{2}F_m\delta + \frac{1}{2}Q\Phi = \Phi\delta \int_V \mathbf{e}^t \cdot \nabla\phi \cdot \mathbf{S}_n dV \quad (2.43)$$

Where F_m is the modal force and Q is the charge on the modal capacitor.

Dividing both sides of (2.43) by δ and Φ returns

$$\frac{1}{2}\frac{F_m}{\Phi} + \frac{1}{2}\frac{Q}{\delta} = \int_V \mathbf{e}^t \cdot \nabla\phi \cdot \mathbf{S}_n dV = \eta \quad (2.44)$$

η is the “turns ratio” for the transduction of voltage to force and displacement to charge on the same port, and is a parameter relating the lumped electrical and mechanical motional parameters. It is defined to be the ratio of modal force to voltage as well as the ratio of charge to displacement (or current to velocity) [18]. The equivalent circuit diagram may be seen in Figure 2.6. Note in this figure the “motional arm” values are now simply the lumped mechanical values since the coupling has been accounted for separately by the transformer.

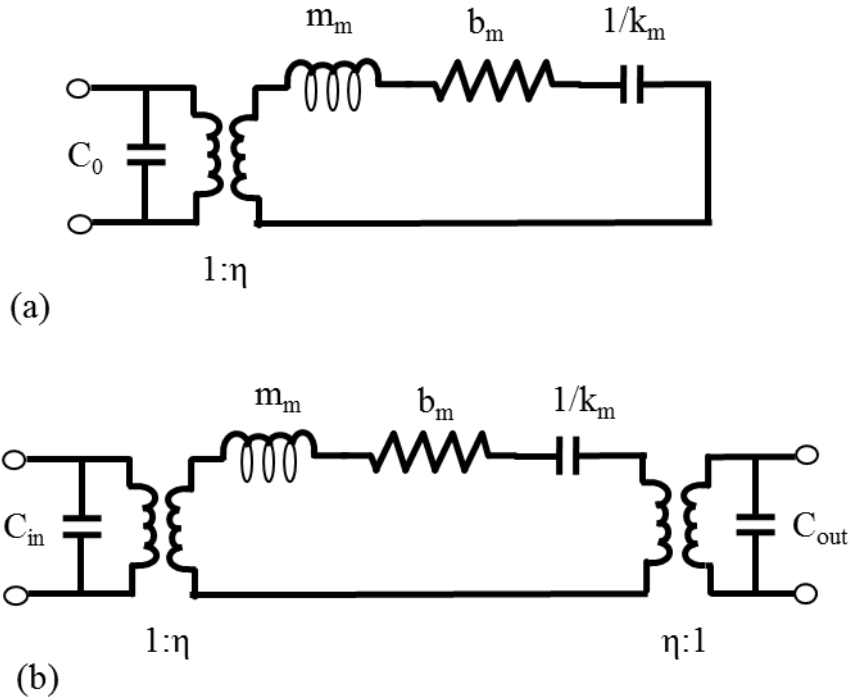


Figure 2.6 The equivalent circuit for (a) a one-port and (b) a two-port resonator with transduction explicitly accounted for by the inductors. Note the values of the motional arm are now simply the mechanical lumped parameters. The BVD/mBVD incorporates the coupling into the motional inductor, capacitor and resistor.

From [18], the motional parameters are

$$R_m = \frac{b_m}{\eta_1 \eta_2} \quad (2.45)$$

$$C_m = \frac{\eta_1 \eta_2}{k_m} \quad (2.46)$$

$$L_m = \frac{m_m}{\eta_1 \eta_2} \quad (2.47)$$

Where k_m , m_m , and b_m are the modal stiffness, mass and damping. The subscripts on η are used to distinguish the case where the input and output electrodes are different.

Subsequent expressions assume the general case in which the turns ratios are not equal, although for a one port resonator they are equal. The modal mechanical

parameters are given by (2.5) and (2.6). Using equation (2.7) and (2.44) in (2.45) returns the motional resistance, given by

$$R_m = \frac{k_m}{Q_m \omega_n \int_V \mathbf{e}^t \cdot \nabla \phi_{in} \cdot \mathbf{S}_n dV \int_V \mathbf{e}^t \cdot \nabla \phi_{out} \cdot \mathbf{S}_n dV} \quad (2.48)$$

In agreement with (2.35). The motional capacitance and inductance may be derived by using (2.44) in (2.46) and (2.47).

2.2.5 Specific Expressions for the Motional Resistance: Beam Extension, Beam Flexure, Disk Flexure, and the A0 Lamb Mode

Analytical expressions for commonly encountered resonant modes are presented in this section derived from (2.33). These modes include beam extensions, beam flexure, the (1,1) harmonic of disk flexure, and the A₀ Lamb mode. The motional resistances presented here will assume the use of 3 axis oriented PZT or aluminum nitride. Certain R_m expression in the following section for modes will use the parallel plate assumption, with the electric field oriented in the 3 direction. For PZT and aluminum nitride, only the e_{31} , e_{32} , and e_{33} piezoelectric constants of the \mathbf{e} matrix can contribute stress from a 3-direction electric field.

The beam extension mode has been studied thoroughly in the literature [20, 18, 5]. The beam displaces along its length, and the main stresses and strains are in the same direction. It tends to be a low frequency mode, since at higher frequencies, when the resonator thickness approaches the wavelength, the displacement is better described by the S₀ Lamb mode. Its analytically modeled unity normalized mode shapes that are harmonics of the cosine function

$$u_{beam} = \cos\left(\frac{q\pi x}{L}\right), 0 \leq x \leq L \quad (2.49)$$

Where q is the harmonic number, L is the length of the beam, and x is the coordinate in the directions of the length of the beam. The modal stiffness, modal mass, and natural frequency may be calculated via the method of [52] and are given by

$$k_m = \frac{q^2 \pi^2 Y_c w_t t_t}{2L} \quad (2.50)$$

$$m_m = \frac{\rho_c w_t t_t L}{2} \quad (2.51)$$

$$\omega_n = \frac{q\pi}{L} \sqrt{\frac{Y_c}{\rho_c}} \quad (2.52)$$

Where Y_c is the composite modulus of the stack in the axial direction of the beam calculated by the rule of mixtures [55], w_t is the total width, t_t is the total thickness, and ρ_c is the composite density [55]. For these parameters, the beam is assumed to be a perfect rectangular prism, which is usually approximately true. The strain is a simple derivative of the displacement. Beam resonators generally have a parallel plate topology, so placing (2.50) and the derivative of (2.49) into (2.34) returns the general motional resistance of the beam.

$$R_{m_{beam}} = \frac{q\pi w_t t_t \sqrt{Y_c \rho_c}}{2Q_m e_{31_{in}} \int_{L_{in}} \frac{du_n}{dx} w_{el_{in}} dx e_{31_{out}} \int_{L_{out}} \frac{u_n}{dx} w_{el_{out}} dx} \quad (2.53)$$

Where L_{in} and L_{out} are the lengths of the input and output electrodes respectively. In the case of a 1-port resonator, these are the same value.

There are two common two-port electrode patterns used for beam resonators that have already been discussed in section 2.2.2 .

For full-length half-width (FLHW) electrodes (Figure 2.5a) fully covering the resonator, the equation for R_m is

$$R_{m_{FLHW}} = \frac{q\pi t_{tot}\sqrt{Y_c\rho_c}}{2Q_m w_{tot} e_{31}^2}, q \text{ odd} \quad (2.54)$$

This expression agrees with the expression presented in [18]. For p even, the motional resistance is infinite. The expression for a 1-port resonator is obtained by dividing the above expression by 4. (2.54) represents the minimum possible R_m , since the electrodes are assumed to cover the entire surface of the resonator. In reality, this is not possible due to the short circuit it would create between the top electrodes. R_m increases with harmonic. This is because for harmonics 3 and above, there will be charge/stress cancellation under the electrode. To be more specific, some areas of the resonant mode will be in tension, while other will be in compression. The piezoelectric material, however, will apply a uniform stress of a single sign to the resonator. This means the applied stress is inhibiting the excitation of the mode in certain locations, and hence the increased R_m . The charge cancellation arises from a similar concept. The positive and negative stress areas will generate opposite charges via the direct effect along the electrode, and the charges will cancel out. This stress and charge cancellation will be a recurring theme, and will be harnessed to cancel the contribution of spurious modes to the electrical response.

In the other common topology for two-port resonators, alternating electrodes are utilized to optimally excite harmonics of beam extension. Higher harmonics may be thought of as being composed of several resonators operating in the fundamental harmonic “glued” together vibrating π radians out of phase. Therefore, these modes will

have approximately the same frequency as the single section. These higher harmonics are useful for controlling the aspect ratio of fabricated devices while maintaining 50Ω shunt impedance for matching purposes in a single device. Once the frequency is picked, the number of sections or the width is modified to obtain the desired capacitance. If the aspect ratio of fabricated beams becomes too low, the shape can be severely degraded. To optimally excite the q^{th} harmonic, there should be q electrode sections, with odd sections connected electrically and even sections connected electrically so as to avoid stress/charge cancellation discussed in the previous paragraph. The R_m of the q^{th} harmonic with q sections is given by

$$R_{m_{AE}} = \frac{(q_{in} + q_{out})t_t\sqrt{Y_c\rho_c}}{8Q_m w_t e_{31_{in}} e_{31_{out}} q_{in} q_{out}} \quad (2.55)$$

$$R_{m_{AE}} = \frac{t_t\sqrt{Y_c\rho_c}}{2Q_m w_t e_{31_{in}} e_{31_{out}} q}, q_{in} = q_{out} \quad (2.56)$$

Where q_{in} and q_{out} are the number of input electrodes and output electrodes, which may be different in the case of an odd harmonic. This expression is in approximate agreement with the expression presented in [51], however in the referenced work the units of the expression presented do not work out to Ohms likely due to a typo.

Transverse beam flexure (TBF) is another common mode. For non-symmetric material stacks, electrode shapes that excite beam extension will also excite some harmonics of TBF. This is because the piezoelectric stack is located off the neutral axis, and the induced stresses create a bending moment, exciting flexure. For this reason, it is considered spurious to the beam extension mode, and is therefore important to

characterize. TBF are also one-dimensional, with the analytical mode shape given by [56]

$$u_n = \frac{1}{2} \left[\cosh\left(\frac{\lambda_p x}{L}\right) + \cos\left(\frac{\lambda_p x}{L}\right) - \sigma_p \left(\sinh\left(\frac{\lambda_p x}{L}\right) + \sin\left(\frac{\lambda_p x}{L}\right) \right) \right] \quad (2.57)$$

Where λ_p and σ_p are frequency parameters, values of which may be found in [56]. In the case of TBF, the displacement is perpendicular to the beam axis, while stresses are in plane [56]. Using Euler-Bernoulli Beam Theory to model the strains, the modal masses, modal stiffnesses, and natural frequencies may be derived by the method of [52]

$$m_m = \frac{m_{tot}}{4} \quad (2.58)$$

$$k_m = \frac{Y_c I \lambda_i^4}{4L^3} \quad (2.59)$$

$$\omega_n = \frac{\lambda_p^2}{L^2} \sqrt{\frac{Y_c I_c}{\rho_c w_t t_t}} \quad (2.60)$$

Where I_c is the composite second moment of area. Using the Euler-Bernoulli Strain in (2.34) returns a general equation for the TBF R_m

$$R_m = \frac{\sqrt{Y_c I \rho_c w_t t_t}}{4L Q_m e_{31_{in}} h \int_{L_{in}} \frac{d^2 u_n}{dx^2} w_{el}(x) dx e_{31_{out}} h \int_{L_{out}} \frac{d^2 u_n}{dx^2} w_{el}(x) dx} \quad (2.61)$$

Where h is the distance from the neutral axis to the midplane of the piezoelectric layer.

For the case of the FLHW electrode, R_m is zero for even harmonics, like the beam extension case. However, for odd harmonics, the behavior is unique. The R_m expression in this case is

$$R_{m_{\square LHW}} = \frac{L\sqrt{Y_c\rho_c I t_{tot}}}{4Q_m w_{tot}^{3/2} [e_{31} h \sigma_p]^2} \quad (2.62)$$

It is interesting to note that the analytical model predicts motional resistance of TBF is directly proportional to the length of the resonator, and constant across harmonics, since the parameter σ_p is approximately one, and λ_p drops from the equation. Due to this constant scaling across harmonics, spurious TBF modes may be problematic in resonator design for length extension resonators across a wide range of frequencies. This expression also suggests it may be possible to fabricate low R_m resonators at high frequencies if Euler-Bernoulli assumptions are not violated.

As discussed previously, to optimally excite a particular harmonic of the one-dimensional beam flexure, all locations where the strain is of the same sign should be covered by the electrode belonging to one port [53]. To optimally pick off the signal from the harmonic, the electrodes of the other port should cover the parts of the resonator for which the strain is of the opposite sign.

Once again using (2.34) and numerically evaluating the integral for even order harmonics, the motional resistance is approximately

$$R_{m_{AE}} \approx \frac{L t_{tot} \sqrt{Y_c \rho_c I / A_{yz}}}{Q_m w_{tot} [e_{31} \sigma_p h [4 + \sqrt{2}(p-1)]]^2} \quad (2.63)$$

Where the $\sqrt{2}$ is approximated from numerical evaluation of contribution of terms from (2.57) to the strain, and A_{yz} is the cross-sectional area of the resonator. It is important to note that (2.63) is only valid for the mode that is being optimally excited, and would fail to describe different harmonics with the same electrode pattern. This contrasts with (2.62) which is valid for all harmonics using a single electrode design. Interestingly, this

expression states that R_m is inversely proportional to a quadratic function of harmonic, p^2 . Comparing this to the similar electrode designs for length extension, (2.57), the TBF motional resistance scales more favorably with harmonic, as the beam extension modes scale as $1/q$.

Since TBF is a spurious mode to beam extension, it is of interest to compare the two expressions for R_m . Taking their ratio gives

$$\frac{R_{m_{LE}}}{R_{m_{TBF}}} = \frac{2q\pi h^2 \sigma_p^2}{L} \sqrt{\frac{t_{tot} w_{tot}}{I}} \approx 4\sqrt{3} \frac{n\pi h^2}{t_{tot} L} \quad (2.64)$$

This equation is approximate, as the parameter σ_p is approximately 1 across harmonics, and the neutral axis is assumed to be at nearly the same location as the geometric XY midplane, (Figure 2.7). This suggests that for a single resonator with TBF as a spurious mode, for the LE R_m to be much lower than TBF R_m , the length should be large, the LE mode should be a low harmonic, and/or the devices should be made very thin. Large length and low harmonic correspond to low frequency for length extension beams. If considering two different beams, one designed for LE and one designed for TBF, to have comparable R_m to the LE resonator, the TBF resonator must have low length (higher frequency), and be thicker.

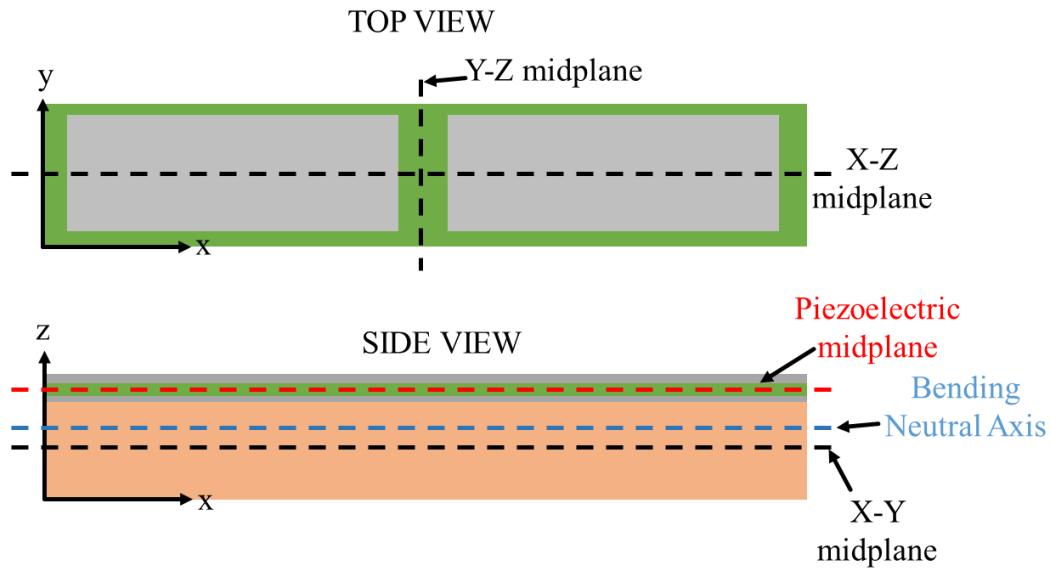


Figure 2.7 A schematic of the beam flexure resonator

Additionally, for low TBF R_m , the piezoelectric layer should be far from the neutral axis for h to be as large as possible. For material stacks symmetric about the XY midplane, the neutral axis coincides with the XY midplane, and the motional resistance is infinite. If TBF is considered a spur, it would be desirable exploit this effect.

Recent alternative designs at lower frequencies have taken advantage of flexure modes in circular plates [3, 53]. Specifically, the (1,1) disk flexure mode displayed -1 dB insertion loss at 20 MHz. In disk flexure modes, the primary displacements are out of plane, with characteristic nodal circles and diameters defining the mode. Stresses and strains are normal and primarily in plane. In contrast to TBF, DFRs have primary stresses in two orthogonal directions. Due to the demonstrated high performance of the (1,1) mode of disk flexure, a closed form expression for the motional resistance is desirable to analyze the dependence of resonator performance on geometric and material properties.

Annular disks in flexural modes of vibration have displacements generally described by [57]

$$u(r, \theta) = [AJ_p(kr) + BY_p(kr) + CI_p(kr) + DK_p(kr)] \cos(p\theta) \quad (2.65)$$

And natural frequency given by

$$\omega_{n_{pq}} = \frac{\lambda_{pq}^2 t_{tot}}{R^2} \sqrt{\frac{Y_c}{12\rho_c(1-\nu^2)}} \quad (2.66)$$

Where p and q are the number of nodal diameters and circles, respectively, λ_{pq} is a frequency constant, R is the outer radius of the disk, r and θ are the coordinates, J and Y are ordinary Bessel functions of the first and second kind, respectively, I and K are modified Bessel functions of the first and second kind respectively, A , B , C , and D are amplitudes, and ν is Poisson's ratio. Tabulated values of λ are given in [57]. The modal mass and spring may be calculated via the method of [52]. Amplitudes A , B , C , and D are determined by boundary conditions, which may be found in [58] for disks and rings. For unclamped disks, $B=D=0$. The ratio of A and C may be determined by the moment boundary conditions and ν , and must be computationally calculated. Since the maximum of (2.65) is not guaranteed to be 1, a unity normalization constant is introduced, $|u_{max}|$, which must be numerically determined. The (1,1) mode shape is now

$$u_{n_{11}} = [AJ_1(kr) + CI_1(kr)] \frac{\cos(\theta)}{|u_{max}|} \quad (2.67)$$

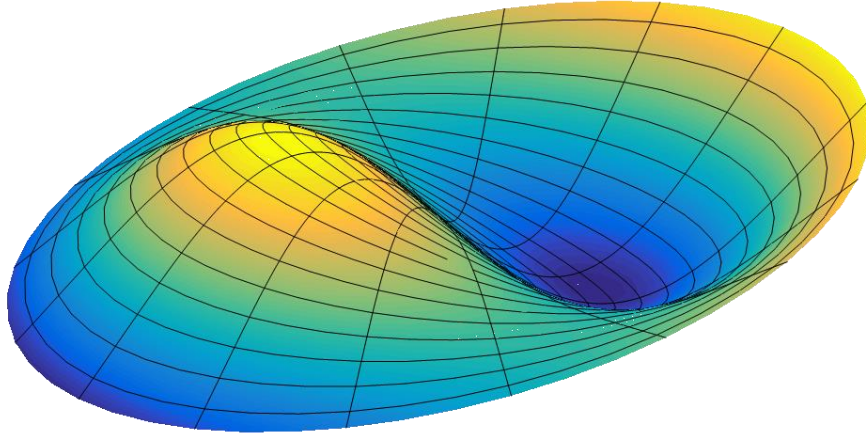


Figure 2.8 Analytical mode shape for the (1,1) mode of disk flexure

Since the three-direction strain is ignored for plates, the integral (2.38) turns into

$$h \int_{A_{el}} -e_{31} \frac{\partial^2 u_n}{\partial r^2} - e_{32} \left(\frac{1}{r} \frac{\partial u_n}{\partial r} + \frac{1}{r^2} \frac{\partial u_n}{\partial \theta^2} \right) dA \quad (2.68)$$

In the case where $e_{31} = e_{32}$ for PZT and AlN, this integral can be evaluated as

$$e_{31} h \int_{A_{el}} \frac{k^2 \cos(\theta)}{|u_{max}|} [AJ_1(kr) - CI_1(kr)] dA \quad (2.69)$$

The modal stiffness may be for calculated for a general mode, but the expression is quite complex. Instead it is more convenient to express the modal spring in terms of the modal mass and natural frequency, which is empirically determined to be $m_m \approx m_{total}/4$ for the (1,1) mode of disk flexure.

$$k_m = m_m \omega_{npq}^2 \quad (2.70)$$

Now placing (2.66), (2.69), and (2.70) into (2.34) return the analytical expression for R_m

$$R_m = \frac{\left(\frac{m_m}{m_{tot}}\right) \pi \lambda_{11}^2 t_{tot}^2 \sqrt{Y_c \rho_c} |u_{max}|^2 (12(1 - \nu^2))^{-\frac{1}{2}}}{Q_m \left[e_{31} h k^2 \int_{A_{el}} \cos \theta [AJ_1(kr) - CI_1(kr)] r dr d\theta \right]^2} \quad (2.71)$$

Where m_{tot} is the total mass. There are a few things to note. First, not only is R_m explicitly dependent on ν , but the parameters λ , k , A , C , $|u_{max}|$, and m_m are all dependent on ν as well. It was empirically determined for various values of ν that $m_m \approx 0.25m$. Second, although it is not explicit in (36), the in-plane strains are in phase, resulting in a larger value in the integral, and hence enhanced electromechanical coupling. The integral of (2.71) involves the use of hypergeometric functions, and requires the aid of a computer. Third, R_m expressions for other modes in the DFR family (both disks and annuli) may be derived by using appropriate boundary conditions on (2.65). Equations for calculating A, B, C, and D are supplied in [57, 58]. Finally, the motional resistance is predicted to be independent of disk radius. This suggest that resonators with similar performance may be fabricated across a wide range of frequencies.

The Euler-Bernoulli approximations no longer apply to resonators in which the plate thickness is of the same order of magnitude as the wavelength. These waves are better described by the Rayleigh-Lamb equations. Lamb waves are dispersive and are a superposition of both shear and longitudinal waves. Recent research has targeted the S_0 and SH_0 Lamb modes, with the A_0 mode being considered spurious [35, 26, 1]. Analytical expression for travelling asymmetric Lamb waves are given in [21]. Standing waves are obtained by superimposing two waves travelling in opposite directions along the x axis

$$u_x = -(A\xi \sin(\alpha z) - D\beta \sin(\beta z))\sin(\xi x)/|u_{max}| \quad (2.72)$$

$$u_z = (A\alpha \cos(\alpha z) + D\xi \cos(\beta z)) \cos(\xi x) / |u_{max}| \quad (2.73)$$

Where

$$\alpha^2 = \frac{\omega^2}{c_1^2} - \xi^2 \quad (2.74)$$

$$\beta^2 = \frac{\omega^2}{c_2^2} - \xi^2 \quad (2.75)$$

And ξ is the wave number, and c_1 and c_2 are the longitudinal and shear acoustic velocities, respectively. The ratio of A/D is found via the characteristic equation given in [21]. Dispersion is inherent to the characteristic equation, and therefore numerical methods must be used to calculate the natural frequency.

In contrast to the previous two modes analyzed, the Lamb waves have a component of strain in the 3 direction, and consequently there will be 3-1 shear strain. PZT and aluminum nitride with the poled axis and electric field in the 3 direction do not have piezoelectric constants to transduce shear, so the integral (2.33) becomes

$$\int_V e_{31} \frac{du_x}{dx} + e_{33} \frac{du_z}{dz} dV \quad (2.76)$$

(2.33) for the A_0 Lamb mode becomes

$$R_m = \frac{k_m |u_{max}|^2}{Q_m \omega_n \int_A (e_{31} \bar{f}(z) + e_{33} \bar{g}(z)) \cos(\xi x) dA} \quad (2.77)$$

$$f(z) = \xi(A\xi \sin(\alpha z) - D\beta \sin(\beta z)) \quad (2.78)$$

$$g(z) = A\alpha^2 \sin(\alpha z) + D\xi\beta \sin(\beta z) \quad (2.79)$$

Here, \bar{f} and \bar{g} are the functions f and g averaged through the thickness of the piezoelectric layer, and A is the area under the electrode. It is important to reiterate that (2.77) is only valid for modes with parallel plate electrode topologies in which the fringing field is negligible. (2.77)-(2.79) are rather opaque due to the dispersive nature of the mode. The treatment required of dispersion is beyond the scope of this paper, but is treated in [21].

For A_0 modes, mechanical energy is stored in shear, which will increase the modal stiffness. However, energy cannot be transduced directly into these strain components. This is undesirable, since the increased stiffness with decreased transduction leads to higher R_m , and decreased k_{eff}^2 . Other materials, such as certain cuts of lithium niobate, may be able to transduce energy into and out of the shear strain.

The problem of the A_0 mode lacking a tractable analytical solution, and more generally, any mode for which there does not exist an applicable analytical solution provides insight into how the methodology presented may be capitalized upon. By taking the modal strain and mechanical energy of a general mode (i.e. spurious modes) directly from FEA and numerically evaluating in the R_m , L_m , C_m , and k_{eff}^2 equations, the device performance may be rapidly predicted. This is because the electrical and mechanical *simulation domains* have been decoupled using modal analysis. To clarify, a computationally inefficient multi-physics simulation is not required; the mechanical

domain may be simulated independently and k_{eff}^2 calculated from the obtained information. This has implication for spur design. If the resonator performance parameters for individual modes may be rapidly simulated, then the spur suppression designed may be quickly generated.

CHAPTER 3

EXPERIMENTAL VALIDATION OF GENERALIZED MOTIONAL RESISTANCE EQUATION

3.1 Modeling and Extracting mBVD Parameters

3.1.1 Introduction

To successfully validate the generalized (section 2.2.3 and the specific (section 2.2.5 R_m expressions, it is necessary to know the values of the mBVD model with any parasitics, such as the parasitic resistances and shunt capacitances. This way the modeled microwave parameters may be compared to the measured microwave parameters, or the modeled R_m may be compared to an R_m extracted from measurement

3.1.2 Extraction from Measured Microwave Parameters

It is possible to extract the shunt capacitances and tether resistance from the microwave parameters. In the case of large resistances, it may be necessary to use a distributed model, as the applied voltage may vary across the electrode. The case of parasitic capacitance can also be quite complicated for two port devices, and as mentioned, this should be kept as low as possible to avoid routing energy around the mechanical domain.

The extraction of mBVD parameters from measurement is done by first comparing measured microwave parameters to the ideal mBVD microwave parameters away from resonance. This analysis is performed away from resonance because the impedance of all the motional arms will be quite high and can be approximated as an open circuit.

Therefore, the microwave parameters should only be a function of non-motional components. The first step is to write out the mBVD ABCD parameters [49] for the two-port resonator of Figure 2.4b

$$A = Y_{C1}Z_{T1} + Y_{C2}(Z_{T1} + Z_M(Y_{C1}Z_{T1} + 1)) + 1 \quad (3.1)$$

$$B = Z_{T1} + Z_M(Z_{C1}Z_{T1} + 1) + Z_{T2}(Y_{C1}Z_{T1} + Y_{C2}(Z_{T1} + Z_M(Y_{C1}Z_{T1} + 1)) + 1) \quad (3.2)$$

$$C = Y_{C1} + Y_{C2}(Y_{C1}Z_M + 1) \quad (3.3)$$

$$D = Y_{C1}Z_M + Z_{T2}(Y_{C1} + Y_{C2}(Y_{C1}Z_M + 1)) + 1 \quad (3.4)$$

Here Z_T is the tether resistance, Y_C is the total shunt admittance of each port, including dielectric losses, and Z_M is the total impedance of all the motional paths plus any parasitic capacitance. Converting to Z parameters for analysis results in

$$Z_{11} = Z_{T1} + \frac{(Y_{C2} + Y_M)}{Y_{C1} + Y_{C2} + Y_{C1}Y_{C2}Y_M} \quad (3.5)$$

$$Z_{12} = Z_{21} = \frac{1}{Y_{C1} + Y_{C2} + Y_{C1}Y_{C2}Z_M} \quad (3.6)$$

$$Z_{22} = Z_{T2} + \frac{(Y_{C1} + Y_M)}{Y_{C1} + Y_{C2} + Y_{C1}Y_{C2}Y_M} \quad (3.7)$$

Away from any resonances and with negligible parasitic capacitance, $Y_m \ll Y_{C1}, Y_{C2}, Z_{T1}, Z_{T2}$ and

$$Z_{11} \approx Z_{T1} + Z_{\square 1} \quad (3.8)$$

$$Z_{22} \approx Z_{T2} + Z_{C2} \quad (3.9)$$

Separating out the real and imaginary parts and substituting the circuit parameters into the impedance and admittances

$$real(Z_{11}) = R_{T1} + R_{B1} + \frac{\tan(\delta_{material})}{C_1\omega} \quad (3.10)$$

$$real(Z_{22}) = R_{T2} + R_{B2} + \frac{\tan(\delta_{material})}{C_1\omega} \quad (3.11)$$

$$imag(Z_{11}) = imag(Z_{22}) = \frac{1}{C_1\omega} \quad (3.12)$$

$$imag(Z_{22}) = imag(Z_{22}) = \frac{1}{C_2\omega} \quad (3.13)$$

Where R_B is the bottom tether resistance. Here $\tan(\delta_{material})$, called “tan delta”, loss tangent, or dissipation factor, is a measure of the ratio of the real component of permittivity to the imaginary part. The ideal capacitor expresses only the imaginary component. The real part appears as a resistor in series with the capacitor. For thin film PZT, the tan delta is generally less than 0.03 when measured at frequencies in the low kHz to MHz range. [39]. In measured frequency data, it may be separated out from the tether resistances due to its frequency behavior. At high frequencies, the curve will

asymptote to the sum of R_T+R_B . Examples curves of these types of extractions are shown in Figure 3.1 for a device with negligible parasitic capacitance.

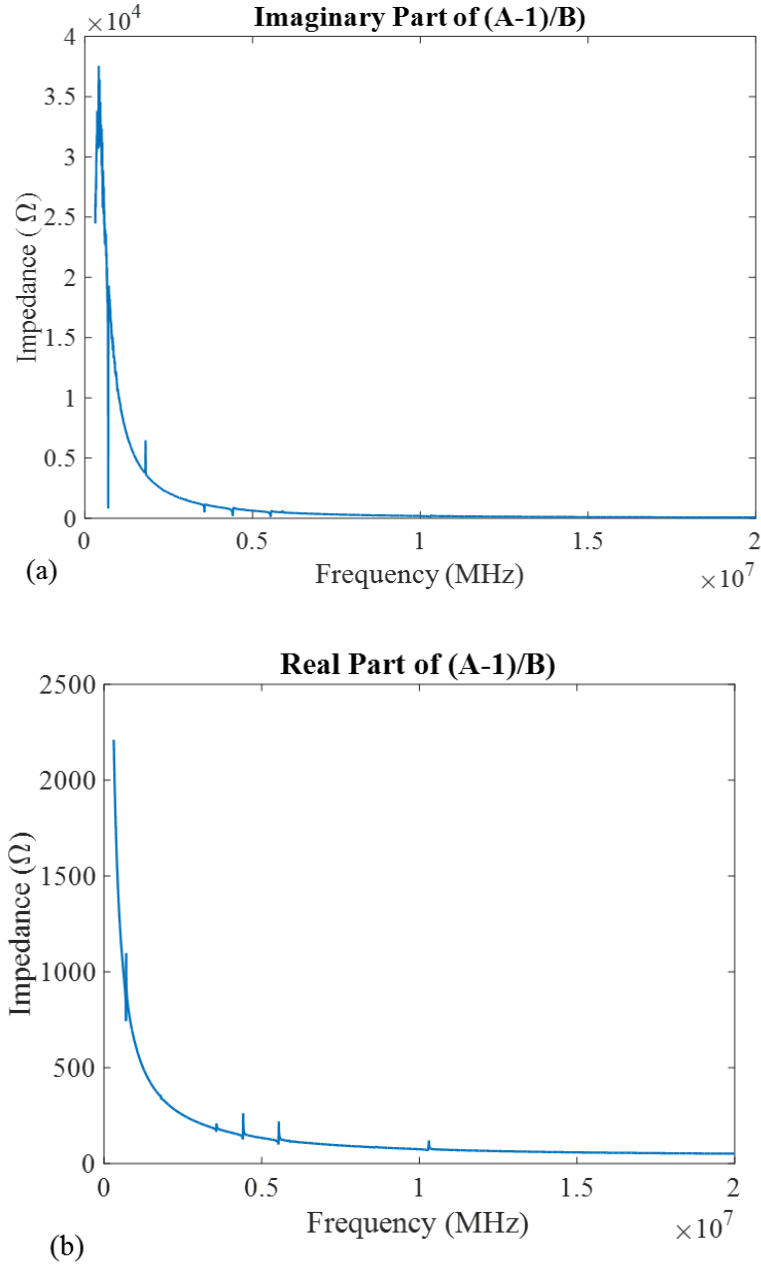


Figure 3.1 (a) The imaginary part of the impedance and (b) the real part of the impedance from a measurement. Note that away from resonances, the imaginary plot acts as an idea capacitor. For the real part of the impedance, the plot asymptotes to a non-zero value, which is the tether resistance. This behavior is due to the loss tangent, which behaves similarly to a capacitor.

The ratio of R_B to R_T may be found by comparing the expected resistances based on layer thickness, width, length, and resistivity.

The main advantage of this method is that no knowledge of the material parameters is required, save possibly resistivity if the value is expected to be different for the top and bottom electrodes. The capacitance and $\tan(\delta_{material})$ are found directly from fitting to measurement, and the ratio of the tether resistances may be assumed from design. One potential problem is that any significant parasitic capacitance complicates the analysis. In this case, the parasitic capacitance must be fit, which adds another degree of freedom to the analysis.

To extract the motional parameters, the simplest method is to use fitting software to match the scattering parameters to measured data after inserting the extracted non-motional parameters. This method is preferred because it simultaneously fits the three motional parameters independently. Another method outlined below uses relationships between R_m , L_m and C_m previous given in section 2.1.2 . This is problematic because the motional impedance changes very quickly near resonance, and its value is dependent upon the accuracy of the previously extracted capacitances and resistances. This means a small discrepancy in the previously extracted parameters can modify the point of zero imaginary impedance. Since the motional impedance changes so quickly near resonance, a small error in this value can cause significant error in the extracted L_m and C_m . However, if one were to pursue this method, the expression for the motional impedance is

$$Z_m = \frac{Z_{C1}Z_{C2}}{Z_{12}} - 2 \quad (3.14)$$

The mechanical natural frequency is the point where the imaginary part of Z_m is zero, which related the product of C_m and L_m . This is approximately true if there are no other nearby modes. In reality the impedance of all other modes will have a small contribution. Once this frequency is known, the motional resistance may be read directly from the real part of the impedance. The imaginary part of the impedance may then be fit using this known relationship.

3.1.3 Extraction from Test Structures

The tether resistances and shunt capacitances may also be obtained from test structures. For the tether resistances, a long serpentine test structure is fabricated for both the bottom and top electrodes. The resistance of this structure is measured, and the metal film thickness and width must be measured or taken from nominal values, and then the resistivity may be extracted from its relation to resistance.

For the capacitance, test capacitors of known area are fabricated with parallel plate topology. For a ferroelectric such as PZT, an impedance analyzer is used to generate curves of capacitance vs. voltage. The voltage signal applied is has a small AC component, typically in the low kHz range. This measurement will also give the dissipation factor. The relative permittivity of dielectrics is generally not constant across frequency [59], so care should be taken to ensure values obtained by this method are valid.

3.2 4.2 Validation of Motional Resistance Equation

Experimental results are presented for free-free beam flexure devices and disk flexure devices. All scattering (S) parameter measurements were taken on a PM5 RF

probe station (Cascade Microtech) at atmospheric pressure. 2 port S-parameters were extracted using a ZVB-8 Rhode & Schwarz vector network analyzer terminated to 50Ω . 2 port calibration using short, open, load, and through standards was performed on a GGB CSF-5 ceramic substrate. Wide and narrow band measurements were taken. The wide band measurements were used to extract shunt capacitance and tether resistance. The narrow band measurements were used to extract the loaded quality factor as well as motional parameters. As PZT is a ferroelectric piezoelectric, its piezoelectric constants and permittivity tune nonlinearly with bias voltages. Therefore, each device was tested at various bias voltages to confirm the veracity of the model. This allows more rigorous validation of the models presented here due the ability to test the devices at several operating conditions.

3.2.1 Beam Flexure Resonators

A total of 9 devices were tested at 13 bias conditions, and the first harmonic of beam flexure was analyzed (Figure 3.2).

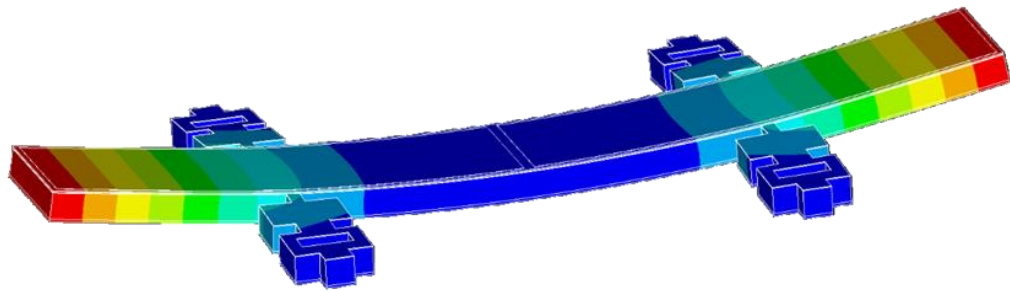


Figure 3.2 An FEA simulation of the total displacement for the first harmonic of beam flexure

Each device was located on a different die on the same wafer. Fabricated devices were all 368 μm long with a half-length full-width electrode configuration, a specific case of the alternating electrodes when the number of sections is two. Device widths were varied from 54 μm to 125 μm . The varied widths affected the shunt impedances and R_m , thereby impacting the resonator loss. These devices were designed for length extension, and were anchored at 25 and 75 percent of the beam length. For the first harmonic of beam flexure, the ideal tether locations are near 27 and 73 percent. However, the FEA models did not show the tether placement to have a significant effect on the displacement profiles.

Simulated resonator frequencies were compared to measured frequencies with good agreement. In both cases there was a modest dependence on the width of the resonator. However, analytical natural frequencies (2.60) were lower than measured frequencies, which were measured from 650 to 720 kHz, whereas the analytical model predicts frequencies from 636 to 647 kHz. Due to this frequency discrepancy, a scanning Polytech OFV laser Doppler vibrometer system was used to confirm modes were correctly identified as TBF by measuring out of plane displacement across the resonator. To find the source of discrepancy between analytical and measured frequencies, the modal mass and modal stiffness were calculated from FEA simulations. Modal masses were found to be within 3% of the analytical value. Therefore, the analytical modal spring value was increased until model and experimental natural frequencies agreed. The analytically calculated stiffnesses were increased significantly, ranging from a 17 to a 42% increase in stiffness due to analytical/measured frequency discrepancies

ranging from 8 to 20%. R_m is directly proportional to modal stiffness, so R_m increased as well.

As previously stated, the analytical R_m was validated via two methods: by independently extracting e_{31} as well as fitting for agreement between analytical and experimental R_m . For the first method, an example of good agreement and poor agreement may be seen in Figure 3.3. For this method, the average error across all devices and voltages was 25%. There are several possible sources of discrepancy. First, the previously discussed frequency effects from differences in resonator and extraction test conditions are important. Secondly, shear effects may have an effect, since the model assumes shear to be negligible. Tether effects due to their offset may stiffen the resonator, raising the motional resistance. For the second method of validation (fitting e_{31} to the measurement), the e_{31} values ranged from 5-12, which agrees with values extracted from cantilever test structures.

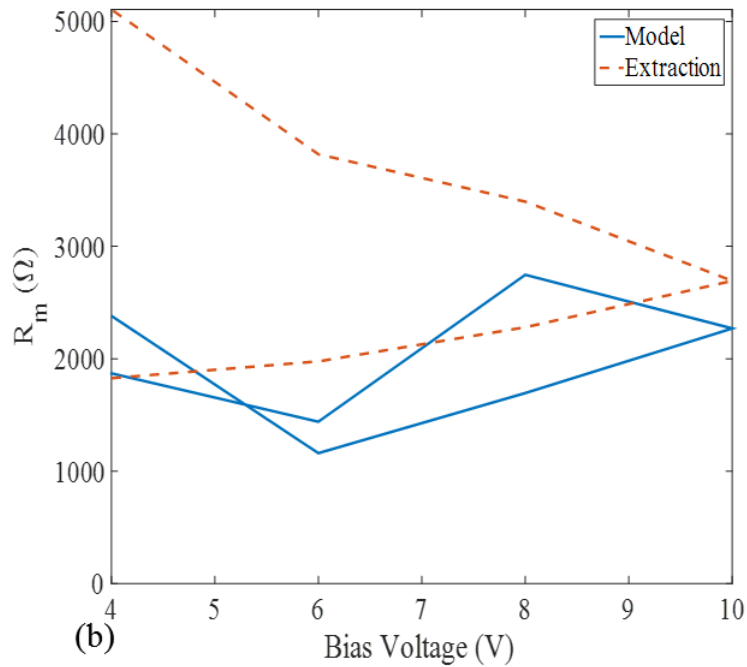
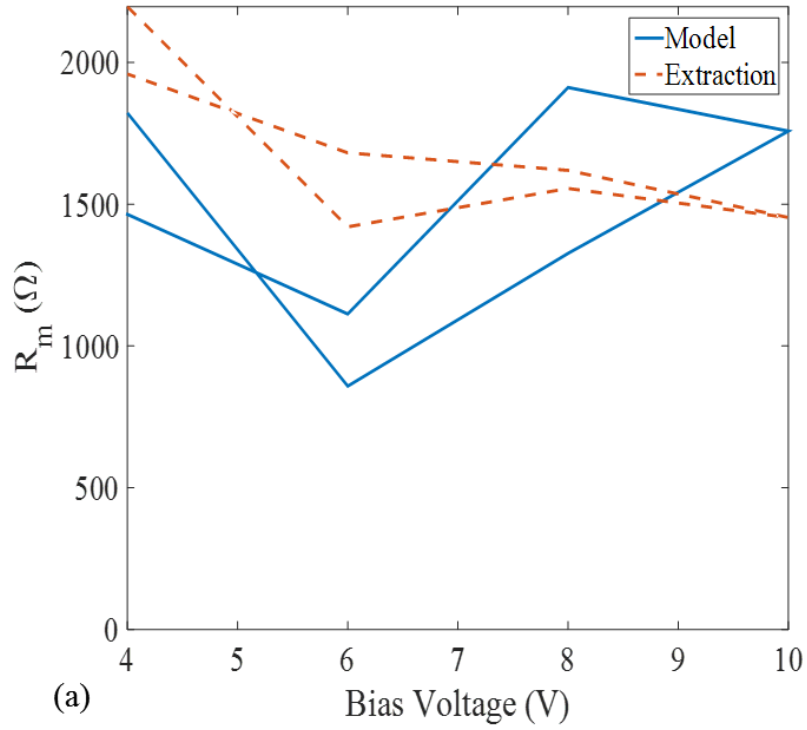
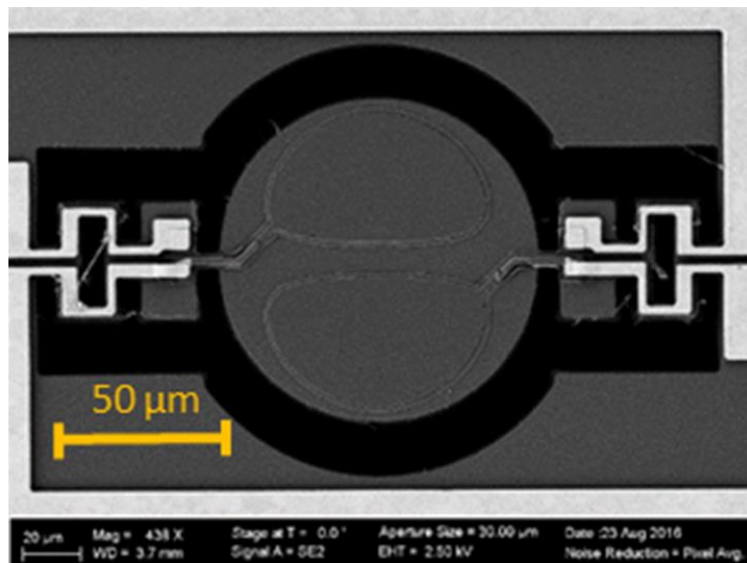


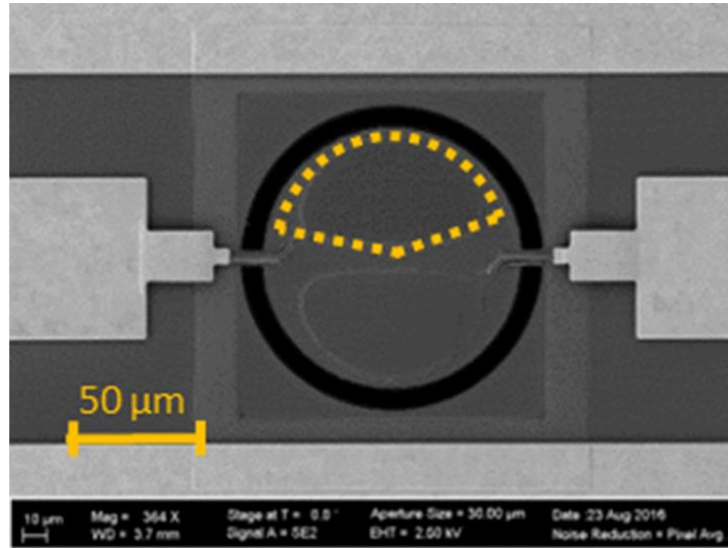
Figure 3.3 An example of (a) good and (b) poor agreement between the extracted and modeled motional resistances for the beam flexure resonator.

3.2.2 Disk Resonators

Fabricated disks had a radius of $56\ \mu\text{m}$ and an electrode shape which may be seen in Figure 3.4. The electrode shape was designed for optimum excitation via the method of [53]. The targeted (1,1) mode (Figure 3.5) has a nodal diameter, along which the device was anchored. As with the TBF devices, there was discrepancy in the predicted analytical natural frequency and measured natural frequency. Measured frequencies of around 22 MHz were 22-23% lower than predicted by analytical models. Modal masses calculated from FEA simulations were within 2% of analytical values, so the modal spring was decreased to match analytical and measured frequencies. This subsequently lowers the predicted motional resistance. Additionally, a modified electrode shape was utilized due to the difficulty in expressing the electrode shape in terms of analytical functions. The electrode shape may be seen in Figure 3.4b.



(a)



(b)

Figure 3.4 (a) An image of a disk with tethers intended to reduce the energy lost to the substrate and (b) a device with traditional straight tethers. The electrode shape used for analytical evaluation is traced over this image.

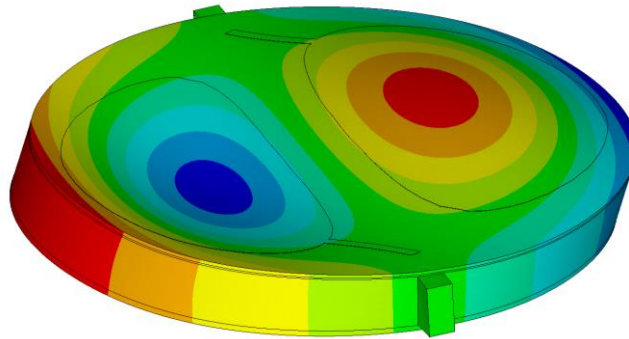


Figure 3.5 An FEA simulation of the mode shape a resonator with straight electrodes. The out-of-plane displacement magnitude is plotted.

Values of e_{31} extracted from cantilever test structures were also used in the R_m expression and compared to R_m values extracted from measurement. Using this

method of validation, the error between modeled and extracted motional resistance was 23% across all voltages. The sources of error are expected to be similar to the sources of error in the TBF analysis. As with the TBF devices, e_{31} values were fit to the data for agreement between extracted and analytical R_m , and fell within the range of values extracted from cantilever test structures. This indicates that the 23% error is likely dominated by lack of precision in the e_{31} extracted from cantilever test structures for actual device operation. Since the piezoelectric constant is squared, experimental error in its value of around 10% is sufficient to create the error seen in R_m . For FEA solutions, inaccuracy in the piezoelectric constants would yield similar errors.

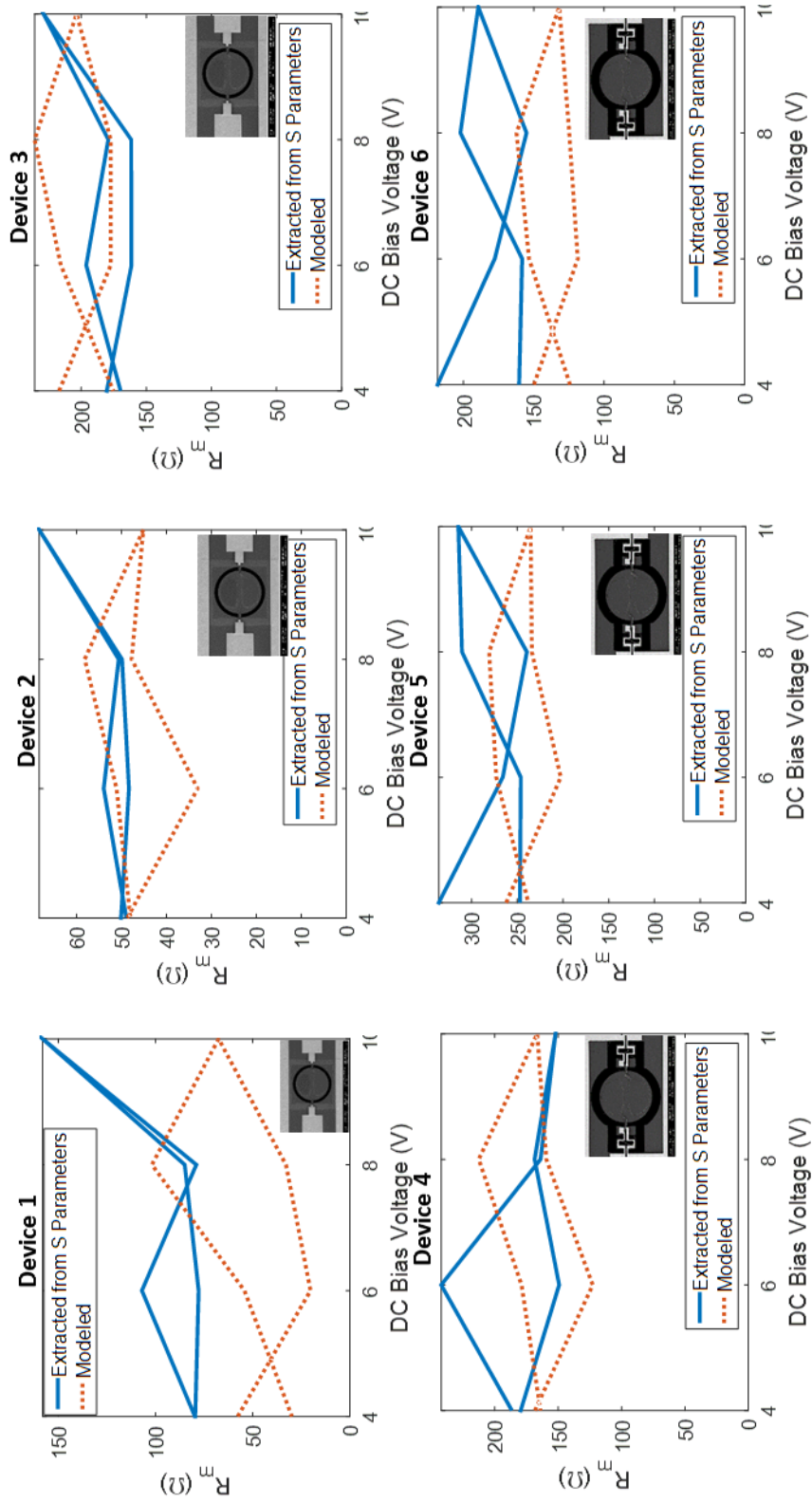


Figure 3.6 Extracted and modeled R_m for 6 disk resonators located on various die across the wafer

Recently a -0.92 dB insertion loss resonator was reported consisting of six of the single discs in parallel electrically [3].

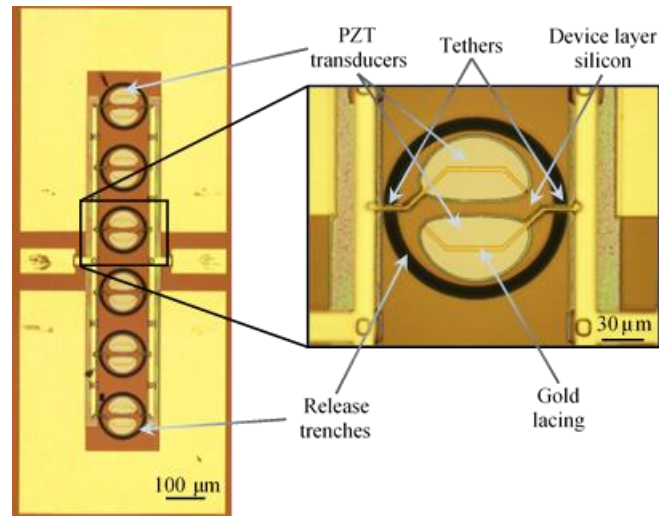


Figure 3.7 The device from [48] with -1 dB of loss

Device 2 from Figure 3.6 was located on the same die as this low loss resonator. Using the parameters extracted from the single device, its mBVD equivalent circuit was placed in parallel six times, simulated, and compared to the S-parameters of the actual device as seen in Figure 3.8. The comparison takes place at 8V and is frequency normalized due to a slight frequency difference between the two resonators. This comparison shows that the models can predict the performance of low loss resonators as well.

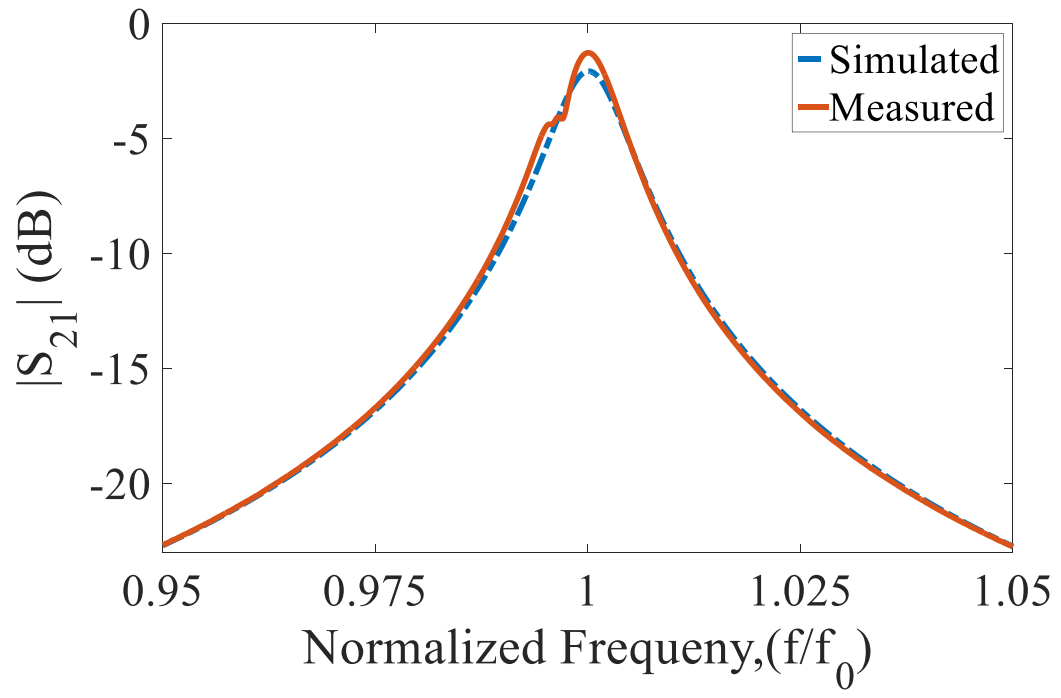


Figure 3.8 The comparison of the device from [3] and device 2 from Figure 3.6 when placed in parallel six times

CHAPTER 4

THE RAPID ANALYTICAL FEA TECHNIQUE

4.1 Overview of RAFT

4.1.1 RAFT Overview

The major components of the RAFT have been discussed: modal analysis, the mBVD, and the analytical equations for the motional parameters of the mBVD. This section will tie them together and discuss the difference between the conventional harmonic analysis. Figure 4.1 gives a graphical overview of the RAFT.

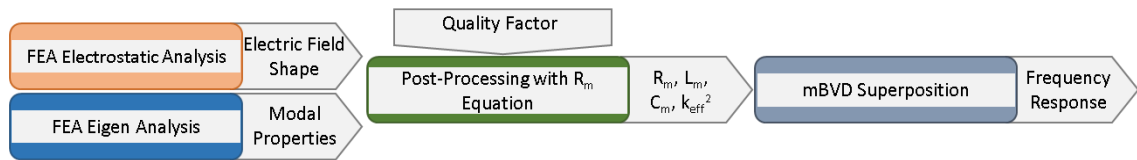


Figure 4.1 A graphical overview of the Rapid Analytical FEA Technique. An electrostatic and modal FEA analysis are run. The modal properties and electric field shape are inserted into the motional parameter equations, and the multi-mode mBVD is generated. The frequency response is then generated using an analytical software package.

For each mode, the relevant information (strain, electric field, frequency, and quality factor) for input to the motional parameters equation must be obtained. The mechanical modal properties are obtained via an Eigen analysis. This delivers the strain, natural frequency, as well as the total mechanical energy and maximum normalized displacement, which are used to obtain the modal stiffness ($k_m = 2U_e \delta^2$). An electrostatic simulation returns the shape of the applied electric field. This simulation can also return any shunt and/or parasitic capacitances for use in the mBVD model, and potentially any electrical resistances.

At this point, the only unknown information is Q_m , which must be measured, assumed, or modeled. The modeling of quality factor is outside of the scope of this work for good reason. There are a variety of mechanical loss mechanisms affecting the losses of MEMS resonators, including losses due to phonon-phonon interaction, viscous losses, and anchor losses. All of the losses are in parallel, described by

$$\frac{1}{Q_{tot}} = \sum_{n=1}^k \frac{1}{Q_n} \quad (4.1)$$

Where there are k total number of sources of loss considered, and n is the n^{th} source of loss. Since only the total Q_m of a resonator is measured or extracted, it is difficult to separate out the various sources of loss and accurately predict the quality factor. This remains an area of active research. Therefore this technique treats the modeling of Q_m as a problem to be separately addressed. Once Q_m is chosen, the other motional parameters are put into the mBVD. Next, analytical evaluation software is utilized to generate network parameters by either directly generating admittance/impedance or first evaluating the circuit into ABCD parameters, and then converting the parameter of choice.

4.1.2 Advantages of RAFT

The RAFT minimizes reliance on simulation by using the generalized motional parameters and mBVD model for analytical modeling. The analytical motional parameters effectively decouples the simulation of the mechanical and electrical domains (thereby reducing the total degrees of freedom), and the use of the mBVD

reduced the number of frequency points that the FEA software must analyze by only requiring information at frequencies where normal modes exist. Apart from the above, this approach has multiple additional major benefits over multi-physics harmonic analysis. First, the electrical component of the problem is only solved once to obtain the shape of the electric field, as opposed to harmonic analysis where it is effectively solved at every frequency step. Second, the completion time of the RAFT is proportional to the number of modes in the simulation band. With harmonic analysis, every single frequency point for which information is desired must be simulated. This results in the completion time being proportional to the number of frequency points. Third, the RAFT will not miss modes by the nature of Eigen analysis, provided a dense enough mesh is used. Harmonic analysis can potentially miss information if frequency points are not appropriately chosen. Fourth, designers may attribute contributions to the frequency response to individual modes. The motional resistance and coupling of every single mode is returned before frequency response generation. This allows the designer to pick out exactly which modes are interfering with the desired response. In harmonic analysis, the results obtained are a superposition of all modes at each frequency, and are difficult to decouple. For closely spaced modes, this can create difficulty in identifying modes, not to mention their individual contribution. Some modes may even be “blurred” out if the coupling is low and the frequency point spacing is not fine enough. Fifth, designers may distinguish between contributions to coupling from individual piezoelectric constants. For example, the RAFT allows designers to quantify the amount of coupling from e_{33} versus the overall coupling, or any other constant of interest. This is of interest in the cross-sectional Lamé mode resonators, since there is coherent coupling from the

e_{33} and e_{31} piezoelectric constants. Sixth, the RAFT allows the designer to set the Q and piezoelectric constants *after* all FEA simulations have been run. This is particularly useful for ferroelectrics for which the piezoelectric constants, dielectric constants, and the Q are dependent on an applied DC bias field. Additionally, the designer may assign Q based on whatever criteria or model they choose, and/or predict best/worst case performance. Finally, the RAFT returns the electromechanical coupling directly after the modal strain and electrostatic field is returned (equation (2.9)). This allows the rapid investigation of mode scaling as a function of geometric parameters *without* having to simulate a large frequency range around the intended mode to fit motional parameters or find the anti-resonance. These advantages allow the RAFT to complete orders of magnitude faster than harmonic analysis and/or give greater insight into device design.

4.1.3 Assumptions and Limitations

While many of the limitations and assumptions inherent in RAFT have been touched upon earlier in this work, it is prudent to dedicate a section to explicitly listing and discussing them.

One of the fundamental assumptions is one truly belonging to modal analysis. The mode shapes obtained by FEA Eigen analysis are done so for a conservative system via the principle of mode orthogonality. Generally, the inclusion of a damping matrix effectively couples the mass and stiffness matrices. In the special case of structural or viscous proportional damping, the damping is assumed to have a linear relationship with the mass and/or stiffness matrices, and is therefore diagonalizable at the same time as the mass and stiffness matrix. In the general case of a damped system with many degrees

of freedom, it is generally difficult or impossible to orthogonalize the matrices [45]. In any case, with the inclusion of damping, all points on the resonant body are no longer guaranteed to be exactly in phase; there will exist some phase lag between various parts of the resonator (i.e. the elastic and kinetic energies are no longer exactly the square of a single sinusoid term). The natural frequency of these modes shifts as well. For lightly damped systems, it is generally accepted that the undamped mode shape and natural frequency are an excellent approximation of the damped behavior, and any phase difference is negligible [60]. Contour mode resonators generally have low damping with Q_m in excess of 800 on the low end, and thus this approximation is generally a good one.

Since the modes are assumed to be linearly independent, the RAFT currently does not model modal coupling, in which energy from one mode is transferred to another mode via nonlinear effects or damping. Another method of energy transfer between modes is “mode conversion.” This can be understood by the fact that when a traveling wave strikes an interface with acoustic mismatch at a non-perpendicular angle, the reflected wave will consist of both shear and longitudinal waves. These waves can recombine with other reflected waves to form a new standing mode. These effects are inherently acoustic in nature that are not captured by modal analysis nor the RAFT. To be clear, the parasitic modes will be modeled, but acoustic coupling will not.

The mBVD parameters are by nature lumped element approximations of the various distributed resistors, capacitors, and inductors. At times, the use of a “distributed” lumped system may be necessary. Consider the case of a very long, narrow parallel plate with negligible fringing field and two electrodes of finite resistivity. The voltage signal

is applied at one end. Along the length of the electrode, the voltage drops due to the resistivity, which correspondingly will appear as a drop in electric field. This may be modeled by cascaded series resistances and shunt capacitances. The RAFT as discussed in this document does not account for the drop in the magnitude of the electric field as the voltage drops along the length of the electrodes. If this is significant, it is best to simulate the electrostatic problem with the resistivity of the electrodes included.

One last caveat when using the RAFT is that the effects of modes outside the simulation bandwidth are not modeled. If for example, there is a very low loss spur just outside the bandwidth simulated, in reality it will have a large effect on the response. However, the RAFT will be blind to such effects, since the mode was not modeled. One possible solution is to simulate just outside the frequencies of interest.

4.2 Wide Band Sweeps and Validation

This section will discuss the validation of wide band frequency simulations against device measurements.

4.2.1 Resonators, Material Properties, and mBVD Parameter Extraction for Wide Band Validation

The frequency response of four resonator geometries are analyzed. The first is a PZT-on-Si disk resonator, intended to excite the (1,1) mode of disk flexure. Devices based upon this mode have shown -1 dB of loss [3]. The second is a PZT-on-Si bar resonator intended to excite the 6th harmonic of length extension. Length extension modes are commonly utilized in MEMS resonators [18, 5, 51]. Both PZT resonators have a two-

port topology The third resonator is an AlN bar contour Lamé mode resonator (CLMR) with top and bottom interdigitated transducer (IDT) electrodes, which has demonstrated low impedance, high coupling and high quality factor [11]. The fourth resonator is an AlN ring CLMR. Both AlN resonators are one-port, but measured data is only available for the bar resonator, as the ring resonator was not fabricated. Therefore, data from the simulated rings is available in Appendix B.

The PZT-on-silicon resonators were tested using a ZVB-8 network analyzer terminated to 50Ω and calibrated using a through, open, short and load standard (GGB CS-5). The two-port scattering (S) parameters were measured. Non-motional mBVD properties were obtained via extraction, as detailed in 3.1.2

The material properties of the PZT-on-silicon resonators were independently measured [61]. The e_{31} constants were fit to the data, but fell within values extracted from on-after cantilever test structures [62]. Lateral device dimensions were taken from design, and modified slightly for frequency agreement, resulting in a $0.5 \mu\text{m}$ decrease in disk radius and beam width. Layer thicknesses were taken from nominal deposition values. The material stack consists of $1 \mu\text{m}$ buried silicon dioxide, $10 \mu\text{m}$ of silicon, 300 nm of silicon dioxide, 125 nm of platinum (modeling a platinum and thin TiO_2 adhesion layer), $0.5 \mu\text{m}$ of PZT, and 50 nm of platinum,

As stated previously, PZT-on-Si resonators generally show the best performance below 200 MHz . At these low frequencies, the electrodes generally have a parallel plate topology. As such, equation (2.34) is applicable. Since a constant electric field is assumed, no simulation of the electrical domain was performed.

The CLMRs were measured using an Agilent 5071C vector network analyzer and Cascade Microtech ground-signal-ground probes in air at room temperature. Calibration was performed on reference substrate using a short, open, and load standard. Additionally, pad capacitances were extracted to obtain performance attributable directly to the device [63].

Material properties were obtained from the default COMSOL material library. AlN thickness was obtained using a Nanospec Spectrophotometer, and the platinum thickness was obtained using a Dek-tak 3030/3St. These resulted in thicknesses of 0.3, 4, and 0.3 μm for the Pt-AlN-Pt stack.

4.2.2 PZT-on-Silicon Disk Resonator

A single PZT-on-silicon disk was simulated, similar to the device in [27]. The disk and model may be seen in Figure 4.2. For this simulation, the electrode shape was taken directly from computer design. The electrode shape was designed to optimally excite the (1,1) mode of transverse disk flexure via the method of [53]. The ends of the anchors were set to have zero displacement in x, y, and z direction. To achieve frequency agreement across the range modeled, the radius of the disk was reduced by 0.5 μm , which is within fabrication tolerances. A measurement was taken from 1 to 100 MHz, and this bandwidth was simulated. The results of this simulations may be seen in Figure 4.2.

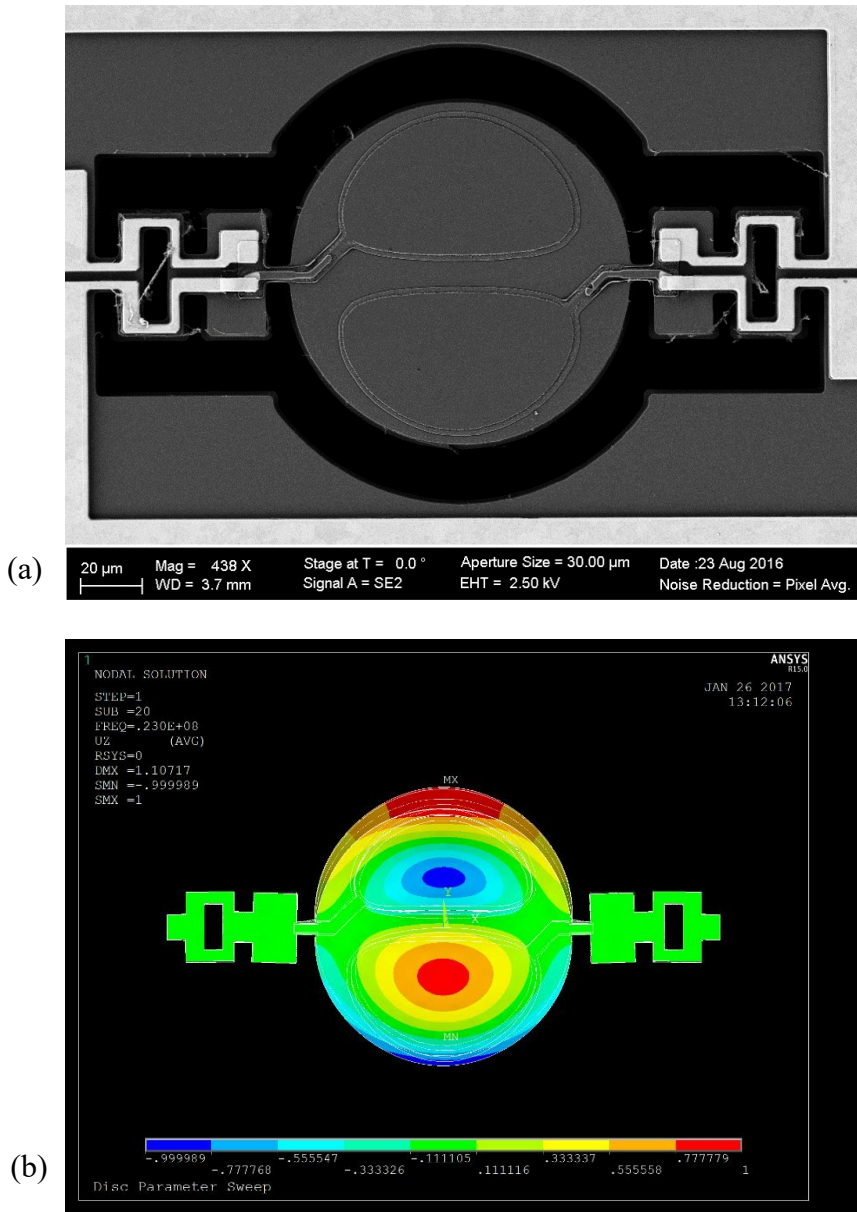


Figure 4.2 (a) A scanning electron micrograph of the disk flexure resonator and (b) the model used the RAFT.

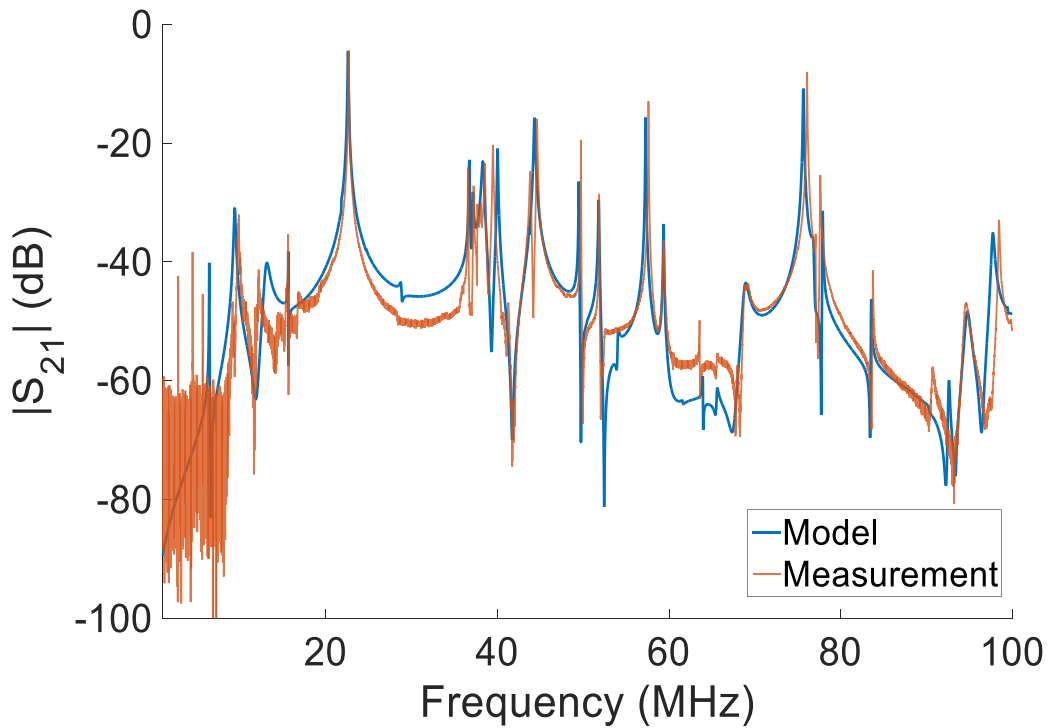


Figure 4.3 The simulated and measured bandwidths of the disk flexure resonator in the 99 MHz bandwidth from 1 to 100 MHz.

The RAFT model was able to accurately predict the device behavior across the bandwidth. The spurious modes in this simulation had measured and fitted Q_m ranging from 50 to 1700. Some modes had fitted Q_m due to measurement difficulty from loss/coupling or frequency spacing. However, extracted Q_m was utilized wherever possible. Across the lowest loss modes, the error in predicted S_{21} at resonance was 1.5 dB.

The time from simulation start to generation of S parameters for the disk was 11.7 minutes. The total number of degrees of freedom was ~460,000. In this frequency span there were 103 modes.

Table 4.1 Summary of simulation for the disk flexure resonator

Simulation Summary			
Frequency Span	1-100 MHz	Total Modes	103
Q_m Range	50-1700	Degrees of Freedom	460,000
Average Error	1.5 dB	Simulation Time	11.7m

4.2.3 PZT-on-Silicon Beam Resonator

The beam extension device was designed to optimally excite the 6th harmonic of length extension. To accomplish this, electrodes 1, 3, and 5 were connected electrically to port 1, and electrodes 2, 4, and 6 were connected to port 2. An image from FEA of the in-plane displacement along the length may be seen in Figure 4.4. The tethering scheme can also be observed in this image.

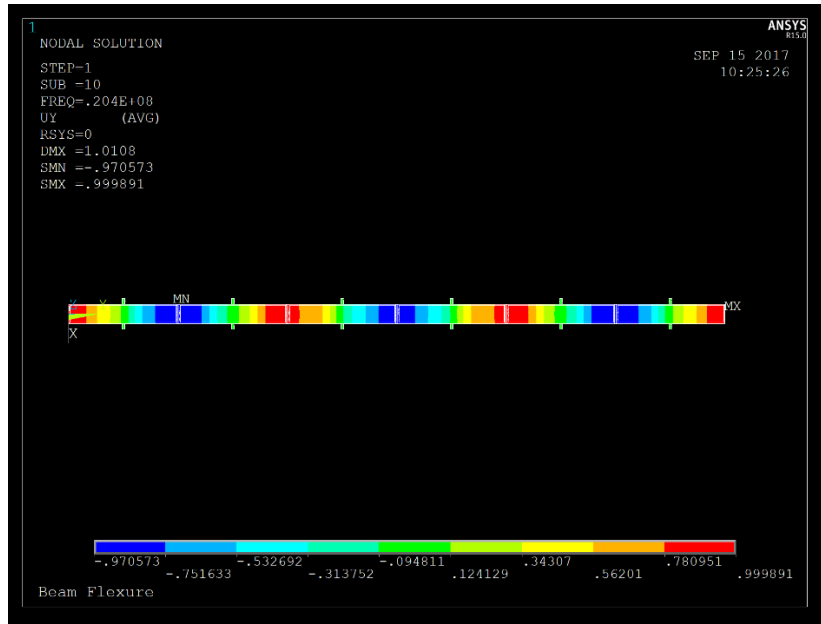


Figure 4.4 An image from FEA modal analysis of the intended mode of the length extension resonator at 20.4 MHz. The magnitude of the displacement along the length of the beam is plotted.

The measurement on the beam extension device was taken from 1-80 MHz, with the targeted mode at 20.7 MHz. Agreement between the measurements and the results from the analytical-FEA technique is presented in Figure 4.5. Fitted and measured Q_m for the beam ranged from 50 to 1500, and average error between measure and model across the lowest loss peaks was 1.8 dB. There were a total of 247 modes in this range, but relatively few show up in the frequency response due to their near-zero coupling.

Table 4.2 Summary of results for the length extension resonator

Simulation Summary			
Frequency Span	1-80 MHz	Total Modes	247
Q_m Range	50-1500	Degrees of Freedom	345,000
Average Error	1.8 dB	Simulation Time	9.9m

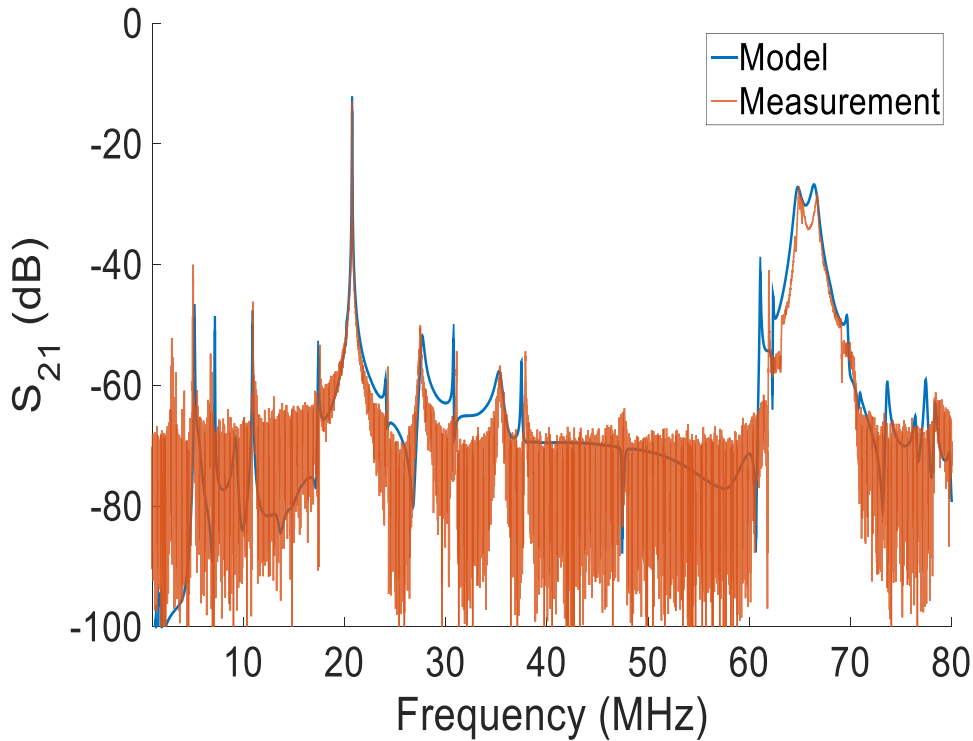
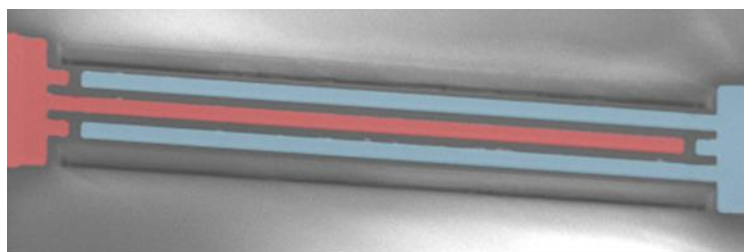


Figure 4.5 The RAFT and measured results of the length extension resonator from 1 to 80 MHz. There are a total of 247 mechanical modes in this bandwidth. However, many do not appear due to near-zero coupling.

4.2.4 AlN Cross-Sectional Lamé Mode Bar Resonators

Three separate beam CLMR designs which had previously been presented in [28] were analyzed with the primary difference between devices being the pitch of the IDT electrodes. The device characteristic may be seen in Table 4.3. All resonators consisted of 300 nm of bottom platinum with a thin TiO₂ adhesion layer, 4 μm of AlN, and 300 nm of top platinum. A schematic of this topology may be seen in Figure 4.6, along with a colorized scanning electron micrograph of the device with ground/signal electrodes highlighted.



(a)



(b)

AlN

Pt

Figure 4.6 (a) A scanning electron micrograph (colorized) of a beam CLMR and (b) a cross-sectional representation of the beam

Since the elastic moduli and densities were not measured, the simulated center frequencies were not well matched to the measured frequencies. Therefore, each simulation band was scaled by 8.29, 7.16 and 6.13 percent for device A1, A2, and A3 respectively. For the simulated results, all modes were set to have identical Q_m to that of the main resonance. This was done due to the difficulty in associating simulated modes with measured modes resulting from the error in the material properties. The results from these simulations may be seen in Figure 4.9a,b,c. An image of the simulated magnitude of displacement with a cross sectional cut may be seen in Figure 4.7.

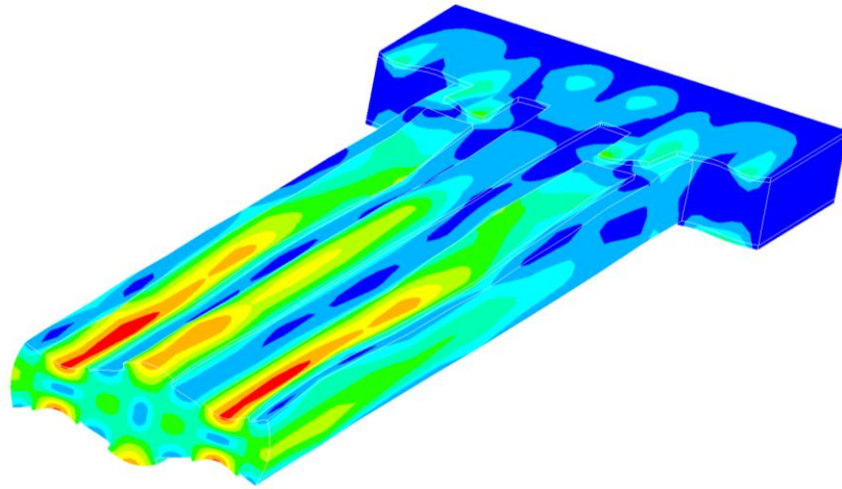


Figure 4.7 Simulated magnitude of displacement of a bar CLMR resonator

One advantage of the CLMR is that it can coherently transduce utilizing the larger e_{33} (~ 1.55 C/m²) and the smaller e_{31} (~ -0.58 C/m²) piezoelectric constants. The RAFT can distinguish between coupling contributions from the various piezoelectric constants. Images of a cross-section of the resonator, the 33 strain, 11 strain, and electric field may be seen in Figure 4.8a,b,c. The strain profile illustrates the coherent coupling that may be obtained (recall the e_{31} and e_{33} have opposite sign).

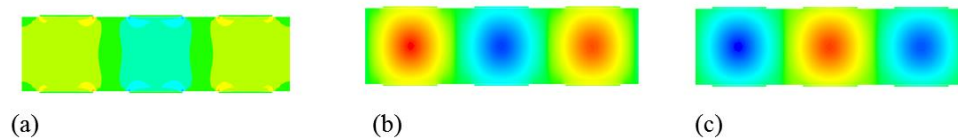
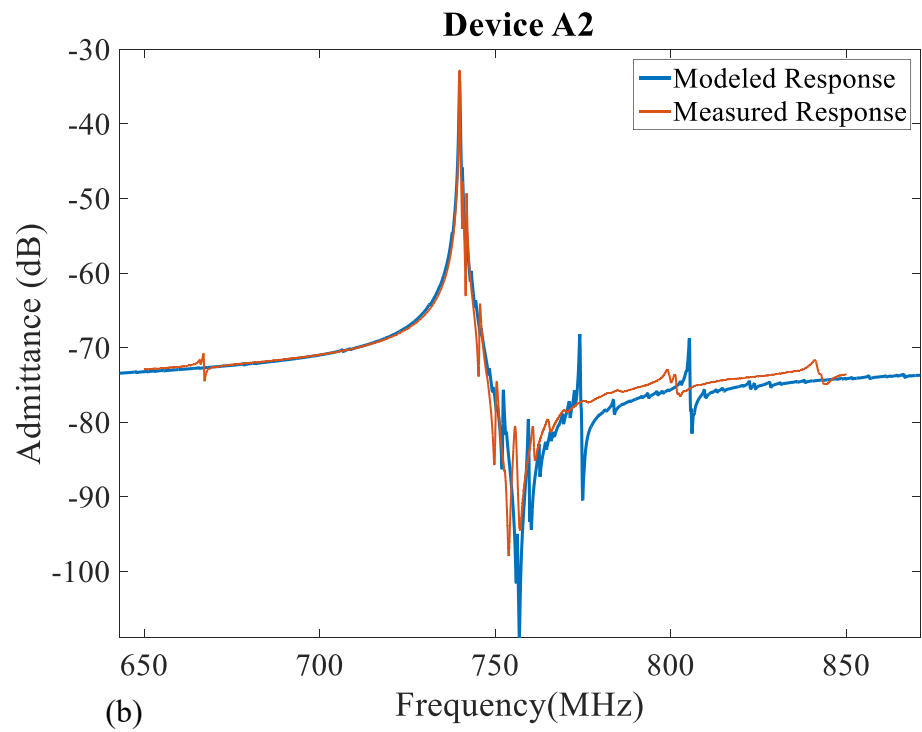
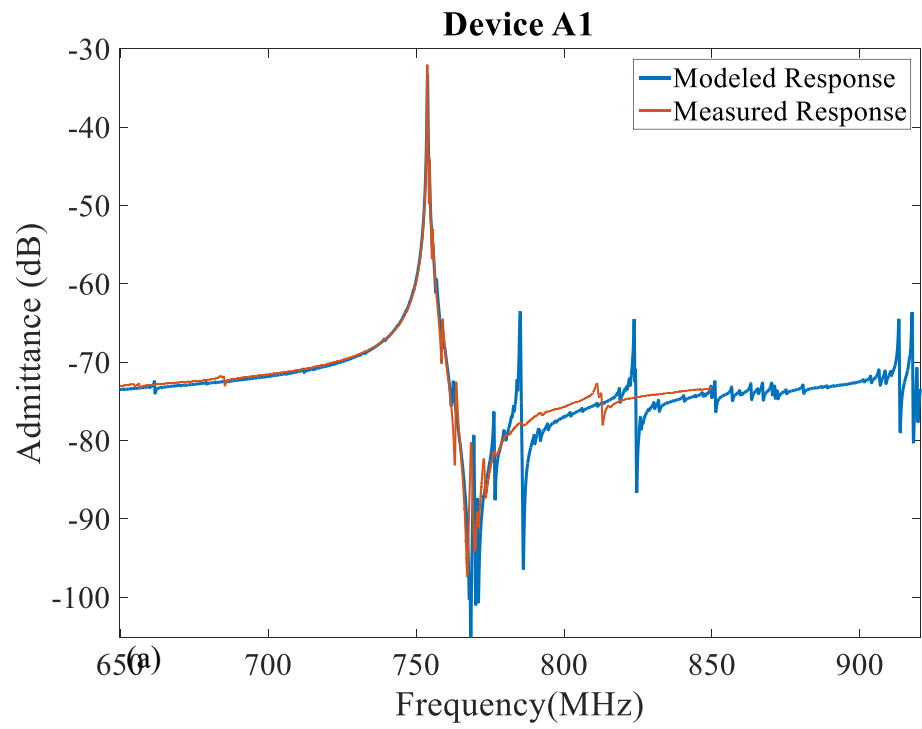


Figure 4.8 The (a) electric field, (b) 33 strain, and (c) 11 strain of a CLMR



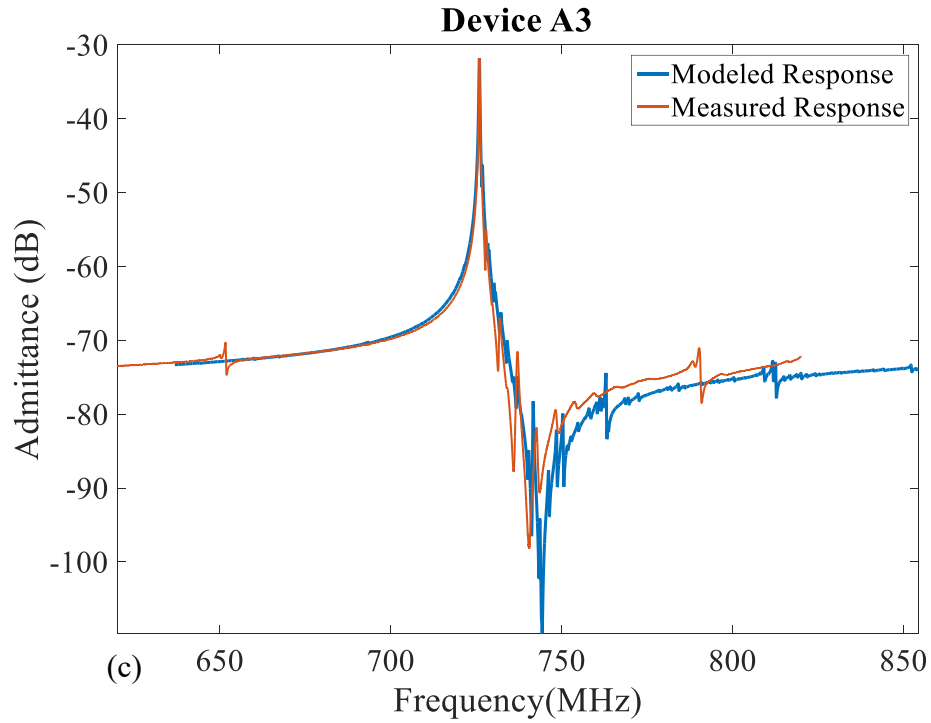


Figure 4.9 The measured and simulated frequency responses of the bar AlN CLMR resonators for (a) device A1, (b) device A2, and (c) device A3.

Table 4.3 Device characteristics and comparison of measurement and the RAFT

Name	Pitch (μm)	Q	Measured Min Impedance (Ω)	RAFT Min Impedance (Ω)	C_m Extracted from Meas. (fF)	RAFT C_m (fF)	RAFT k_{eff}^2
A1	5.0	2820	39.9	45.7	1.76	1.87	3.69
A2	5.2	2493	43.8	50.0	1.77	2.00	3.79
A3	5.4	2977	39.0	38.9	1.97	1.90	3.94

The simulations took an average of 26 minutes to complete from start to frequency response generation. As mentioned previously, the RAFT's completion time is proportional to the number of modes in the simulation bandwidth. At higher frequencies, the number of spurious modes increases drastically. This results in a decrease speed for

the RAFT in terms of bandwidth simulated per minute. To allow for rapid modeling, a mesh such as that show in Figure 4.10 was utilized. The mesh is coarse in the length, but fine along the width and the thickness. A similar approach to meshing was taken in [64].

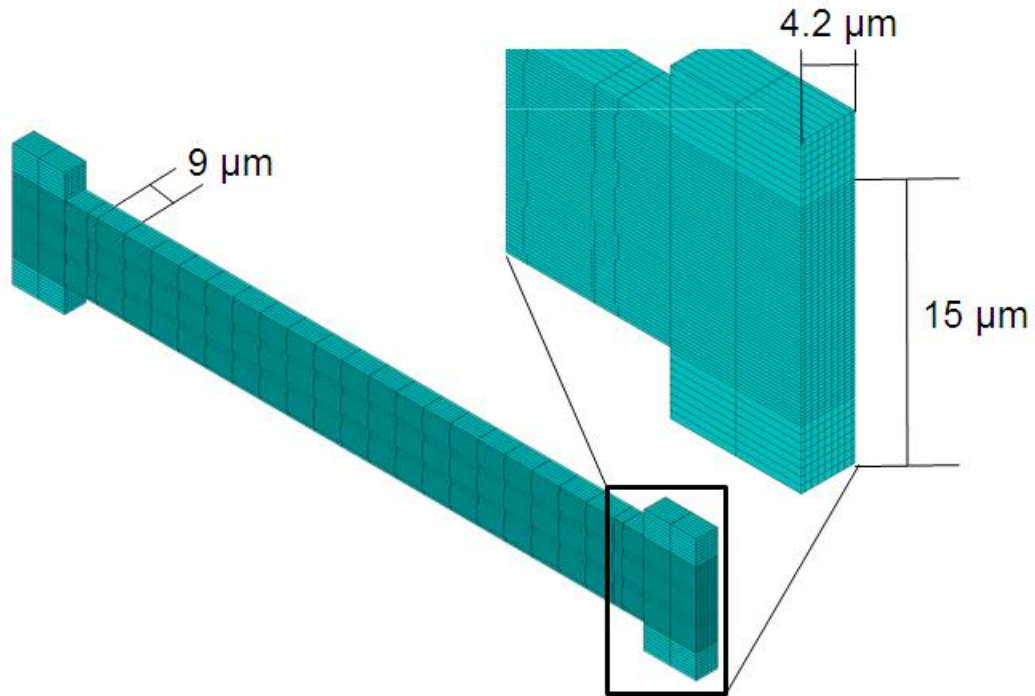


Figure 4.10 The mesh used for the CLMR resonators

After then center frequencies are aligned and the Q_m are set to the measured value, excellent agreement is seen between the measurement and simulation. As previously mentioned, it is possible to extract exactly what portion of the coupling is attributable to each piezoelectric coefficient. One of the reported benefits of CLMRs is the ability to coherently transduce using both e_{31} and e_{33} . RAFT confirms this numerically. The RAFT predicts e_{31} contributes 17.3, 19.0, and 21.2 percent of the total coupling for devices A1, A2, and A3, respectively. The coupling was calculated using two methods, namely (2.9) and from [14]

$$k_{eff}^2 = \frac{f_a^2 - f_r^2}{f_a^2} \quad (2)$$

Where f_a is the anti-resonance frequency, and f_r is the resonance frequency. Both methods agreed within half a percent. The calculated results from measurement and simulation may be seen in Table 4.3. The values from measurement were extracted by fitting an mBVD model to measured data.

The inability to associate spurs between measurement and simulations creates difficulty in drawing a conclusion about the accuracy of the modeling of the spurious modes.

4.3 5.3 Other Modeling Capabilities Enabled by RAFT

4.3.1 Wide Band Spur Suppression

One technique to completely suppress spurious modes is to have equal and opposite polarity charges accumulate on the electrode, or equivalently produce stresses that will interact destructively with the modal strain field. An alternative description is there is no modal force (an electric field produces no net stress) and no modal charge (a strain field produces no net charge). By looking at equations for the modal force and charge, (2.24) and (2.31), this condition is given by

$$F_m, Q_{out} \propto \int_V \mathbf{e}^t \cdot \nabla \phi \cdot \mathbf{S}_n dV = 0 \quad (4.3)$$

Topologies meeting this condition may also be said to have infinite R_m or a k_{eff}^2 of zero, since this integral also shows up in both expression. An R_m of infinity corresponds to an open circuit in the mBVD at the mechanical resonance. It is important to understand that the mode still exists mechanically, but no energy is coupled into and/or out of the mode piezoelectrically.

To understand this concept intuitively, it is useful to consider a mode with a simple mode shape such as beam extension. The extensional mode shapes of a beam much longer than its width or depth may be described by cosine harmonics, as discussed in 1.1.2 Therefore, the normalized strain is given

$$S_n = \frac{du}{dx} = \frac{n\pi}{L} \sin\left(\frac{n\pi x}{L}\right), 0 \leq x \leq L \quad (4.4)$$

For a uniform field, the (4.3) reduces to

$$F_m, Q \propto \int_L \sin\left(\frac{n\pi x}{L}\right) dx = 0 \quad (4.5)$$

Where Q is the charge appearing on the output electrode. Here L is used to denote locations along the beam which have an electrode region, and therefore non-zero electric field. Now, consider the second harmonic with an electrode along the entire length. The stress produced by the electric field is constant ($T = e E$). However, the mode shape has equal portions of positive and negative strain. The constant stress/electric field therefore does not have a net interaction with this mode as it produces stresses incompatible with the mode shape. Equation (4.5) quantifies this, and is trivial to see there will be no modal force. Similarly, if the beam is assumed to be vibrating purely in the second harmonic, one half of the beam will produce positive charge at the same time

the other half is producing an equal amount of negative charge, resulting in no net charge on the electrode.

To demonstrate the ability of RAFT to perform an analysis resulting in the suppression of spurious modes using the charge/strain cancellation previously described, a simpler technique was employed targeting odd harmonics of length extension. It may be seen from (2.56) that if the resonator is electroded symmetrically about the mid-plane defined in Figure 4.11, even harmonics are completely suppressed. One simple way to suppress a particular mode is to place electrodes at $L/(2n)$ and $L(1-1/(2n))$. It can trivially be shown that electroding in this manner to cancel the n^{th} harmonic will also cancel the $2n, 3n, 4n$, etc. harmonic. For example, electroding at $1/6L$ and $5/6L$ will suppress the 3rd, 6th, 9th, 12th, 15th etc. harmonics. The issue here becomes the prime number harmonics. It is not possible to use this scheme to cancel out the 5th, 7th, 11th, 13th, etc. modes at the same time as multiples of the 3rd harmonic. Therefore, it is necessary to consider an alternative topology to simultaneously suppress multiple modes.

To achieve this, the device is still fabricated with electrodes symmetric about the mid-plane. However, there is no longer one continuous electrode region, and instead the electrodes are arranged at location a, b , and c as shown in Figure 4.11.

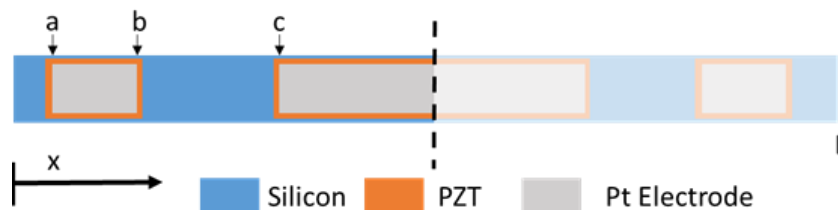


Figure 4.11 The electrode pattern used to design for spurious mode suppression.

From (4.5) the condition for complete cancellation now becomes

$$\cos\left(\frac{an\pi}{L}\right) - \cos\left(\frac{b\pi}{L}\right) + \cos\left(\frac{c\pi}{L}\right) - \cos\left(\frac{0.5\pi}{L}\right) = 0 \quad (4.6)$$

This equation is not analytically solvable, and describes a hypersurface. The solution space of several harmonics are shown in Figure 4.12.

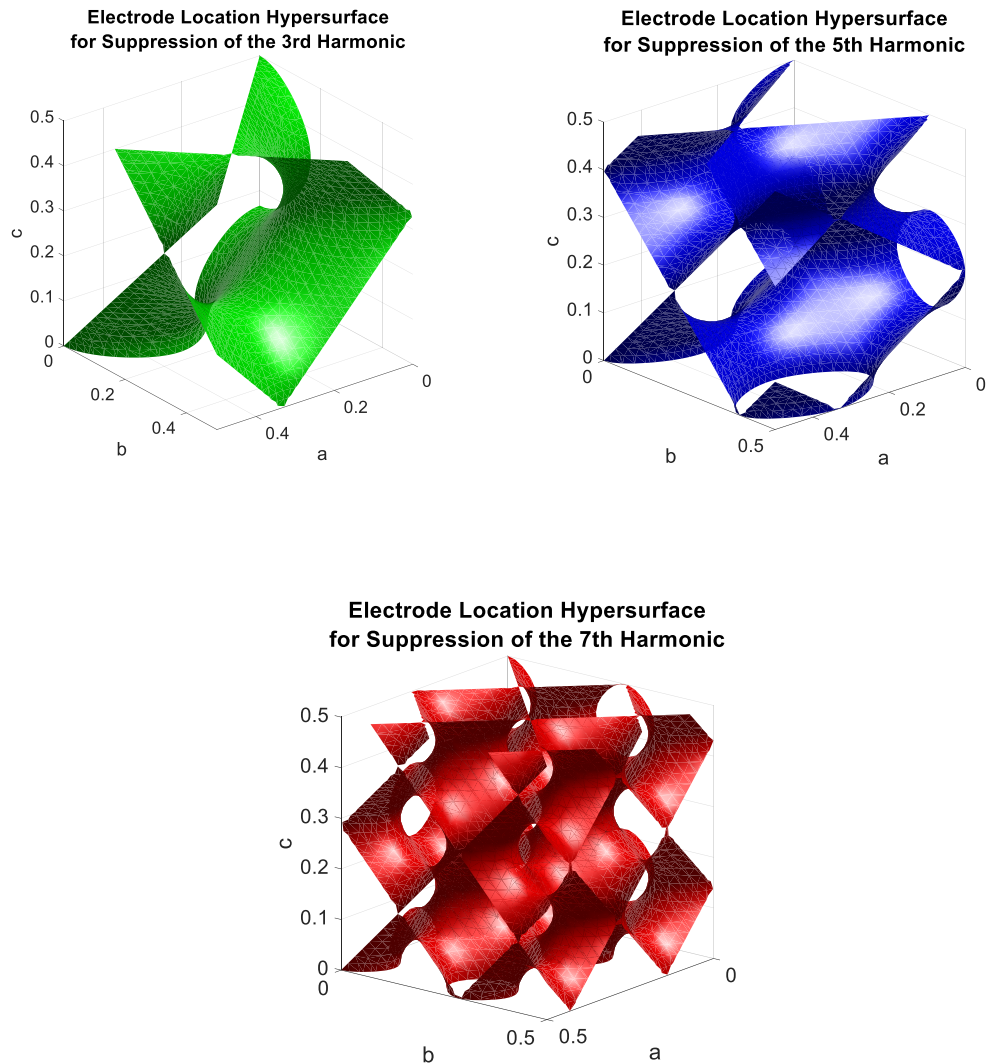


Figure 4.12 The solutions to the analytical condition for complete suppression

To simplify the analysis, the location c was fixed, and the a, b locations for complete suppression were graphed. This is equivalent to “slicing” planes of Figure 4.12 at a c

location parallel to the a - b plane and plotting the results on the same axis. Two examples of the plots produced by this technique are plotted in Figure 4.13.

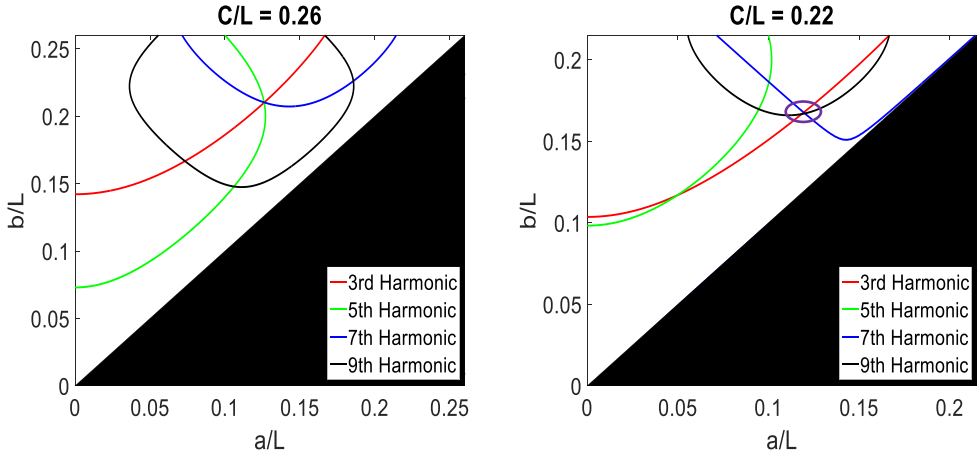


Figure 4.13 An example of the "slices" of the hypersurfaces are two difference c locations

Each curve represents the a, b locations which will completely suppress a mode. The intersection of these curves represent designs which will completely suppress multiple modes. For example, in Figure 4.13, there is a location which will completely suppress the 3rd, 5th, and 7th mode which is outlined in purple. Graphical representations of the integration of the strain/charge at this design point are shown in Figure 4.14.

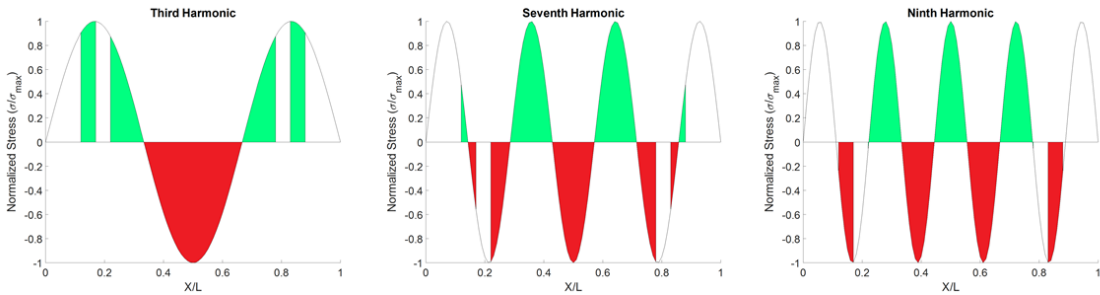


Figure 4.14 Graphical representations of the point circles in purple of Figure 4.13

Real devices tend to exhibit non-idealities in the mode shape, and therefore these devices were simulated in the ANSYS FEA package. Slight deviation was seen in the

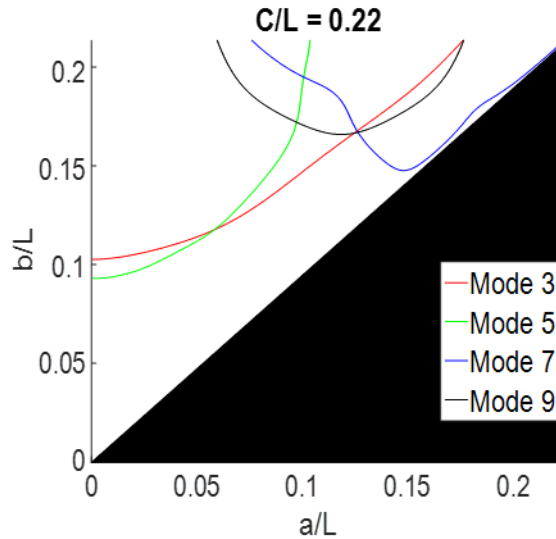


Figure 4.15 Mode suppression design space generated using FEA simulation

curves. Figure 4.15 shows the same a, b, c values from Figure 4.13, but with the curves generated from RAFT simulations. The devices simulated had the same mechanical material properties as those of the devices in 4.2.2 and 4.2.3. Since the silicon and silicon dioxide layers are ~ 20 times thicker than the PZT and electrodes, the removal of these layers were assumed to have negligible effect on the designed devices, and was not simulated. Additionally, very thin traces must be run to connect the middle section to the two outer sections. These were assumed to have negligible effect on the coupling, and thus not simulated.

Two port devices were designed based on these simulations. Each port was designed to not excite/detect two modes, for a total of four suppressed modes. A scanning electron micrograph of a more conventional full-length half-width design and a spur suppression device and is seen in Figure 4.16.

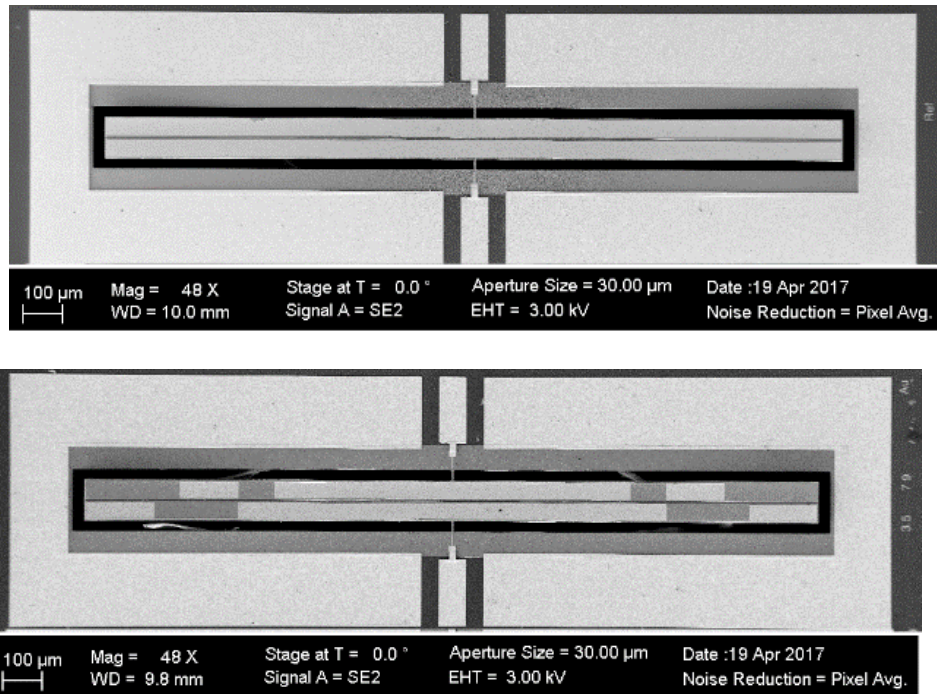


Figure 4.16 Scanning electron micrographs of the (a) conventional full-length half-width electrode and (b) a spurious mode suppression design

The traces in Figure 4.16 connecting the section are quite thin and difficult to see. They are laced with gold to reduce the resistance between sections. If the resistance here is too great, the voltage may drop severely across the narrow section, resulting in a smaller magnitude electric field in the end sections. This would reduce the cancellation effects, resulting in incomplete suppression. Results from the devices in Figure 4.16 may be seen in Figure 4.17 and Figure 4.18, with the suppressed modes enhanced to reveal detail.

The intended mode has experienced virtually no reduction in magnitude. This is due to the highest strain points of the first harmonic still being covered by the electrode. The integral of the first harmonic is graphically represented in Figure 4.19. Clearly, there is not much degradation in coupling due to the locations of the electrodes. Meanwhile, harmonics 3, 5, 7, and 9 have all been suppressed heavily. Some of these modes are not

as well suppressed as others. This could occur for several reasons. First, there may be some electrode misalignment. Second, it was assumed that removing PZT and platinum from the resonator did not affect the mode shape much. Third, the effect of the resistance between electrode sections was not modeled, possibly resulting in a reduced coupling effect. However, all modes exhibited a significant amount of suppression, demonstrating the effectiveness of this technique, although further modeling may be required.

It is apparent that there are still significant spurs in the response. The most serious spurious modes are harmonics of width flexure. With an asymmetric stack and non-trivial electrode design, it is not possible to completely suppress the fundamental width flexure mode, since all strain is of the same sign. Additionally, despite targeted modes being suppressed, the magnitude of some spurious modes increased. Worse still, new modes appeared, such as the modes around 3 MHz in the spur suppression design. This points to the problem discussed earlier: when making changes to electrode design for spurious mode suppression, the effect on *all* modes must be considered. This suggests the use of RAFT over conventional simulation techniques, as the modification of electrodes is quite quick to analyze with the assumption that changing electrodes is a perturbation to the mechanical mode shape.

The RAFT may be used to implement this technique for more complex resonators. Resonators often are not easily described analytically due to complex fields, such as S_0 based resonators with lateral field electrodes, or PZT-on-silicon resonators with multiple elastic layers. RAFT directly calculates R_m for complex modes, and may be used to design devices which do not exhibit chosen spurious modes. This suggests the

use of an algorithm. The use of an algorithm is in part required since there are many electrode patterns that may perfectly suppress a given mode. Consider the example of the second harmonic of length extension: an electrode from $(0.5L-a)$ to $(0.5L+a)$ will completely suppress the mode according to (4.5). Here a is any positive real number less than $0.5L$. Other modes, such as the fundamental harmonic of extension, cannot possibly be suppressed with a non-trivial electrode design, since the strain of the mode is all the same sign. Finally, consider that in the process of adding or removing electrode to suppress a particular spurious mode, every other spurious mode is also affected by this addition or subtraction. Practically, this can lead to the excitation of previously non-problematic spurious modes. The complexity of strain fields, electric fields, and interdependence of all modes on the electrode shape points towards a computational solution.

Here the author would like to suggest one possible approach to this problem. First, the resonator is simulated with electrode coverage designed to optimally excite the intended mode. Then, the electrode volume is discretized into many smaller domains, similar to a mesh with only one element through the thickness, while quite dense in the width and length directions. A genetic algorithm is then used to add and remove these domains to the resonators, and the electric field is re-simulated. The mechanical domain is not re-simulated during this process as the electrodes, being generally much thinner than the rest of the resonator, are considered a perturbation to the mode shape. The electrostatic simulations are generally even faster than the Eigen analysis, taking on the order of seconds to tens of seconds to complete. Once a solution is reached, then the

mechanical domain is re-simulated to refine the design. These devices may then be arrayed in parallel to obtain the desired shunt impedance, as was done in [3].

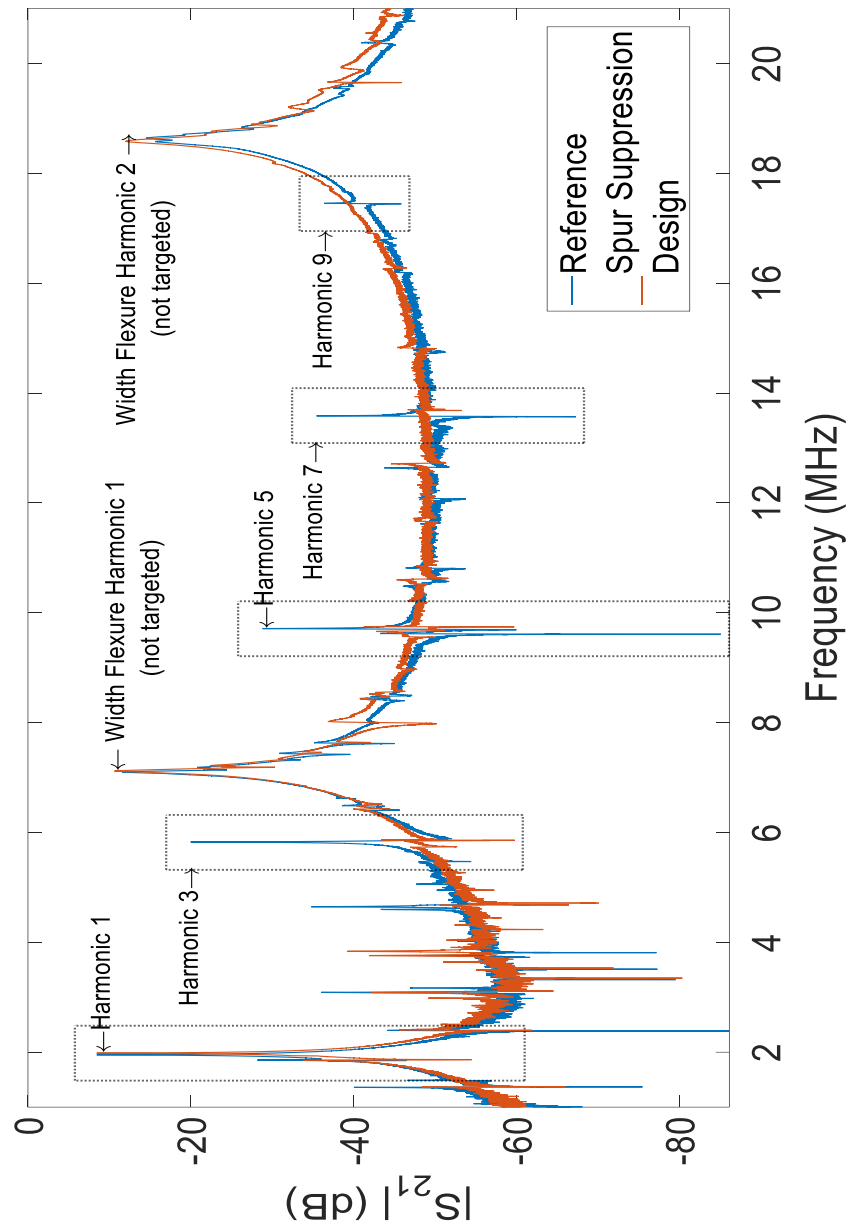
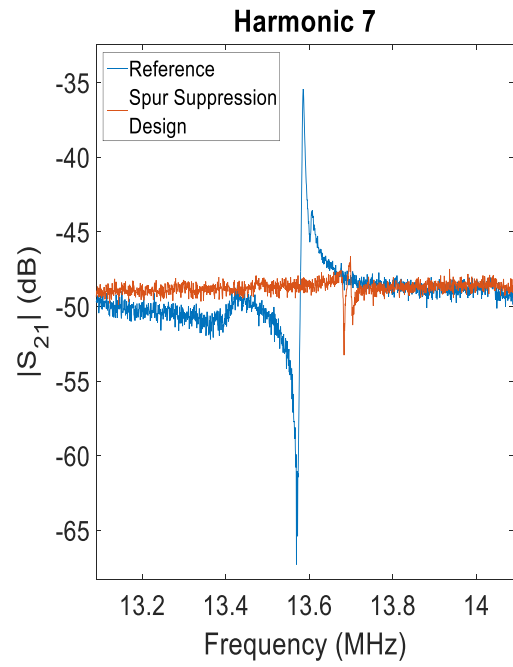
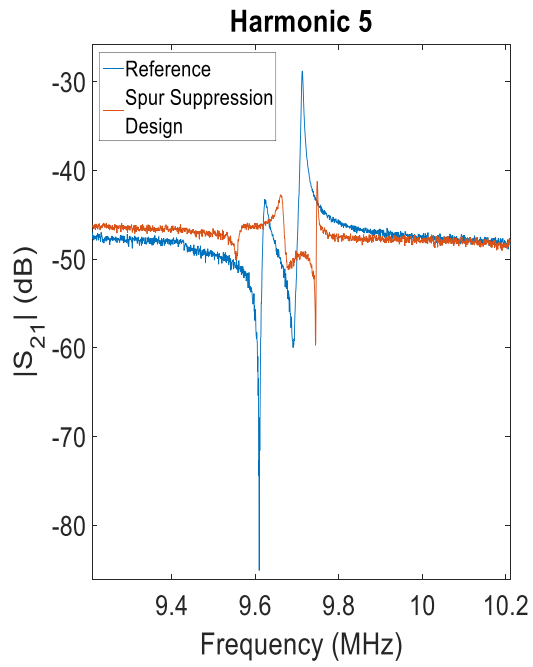
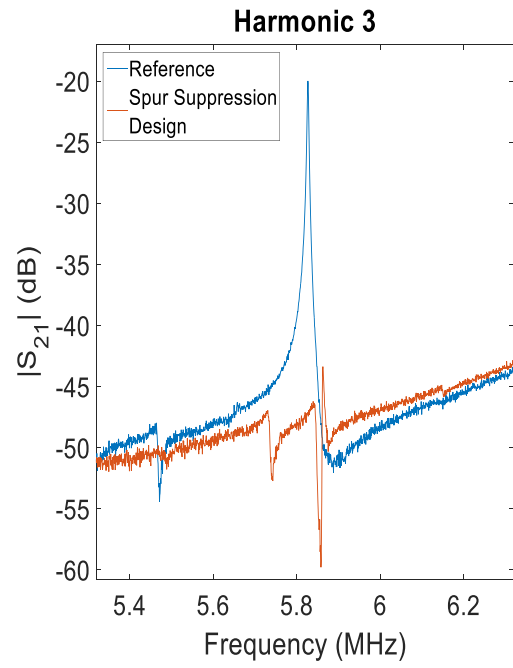
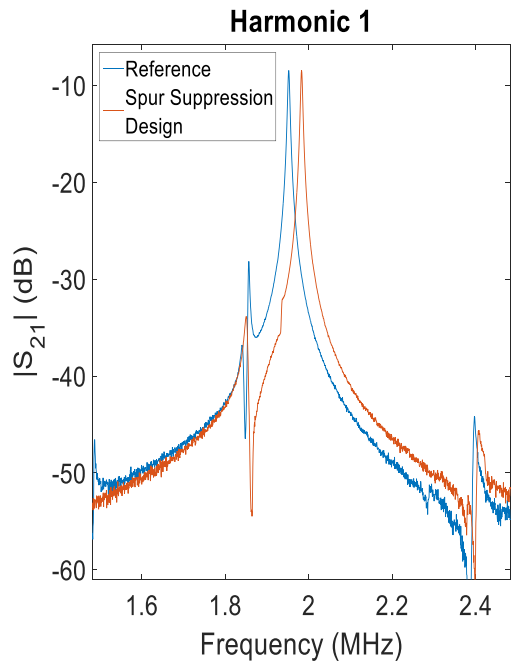


Figure 4.17 Wide Band sweep of the conventional design and the spur suppression design



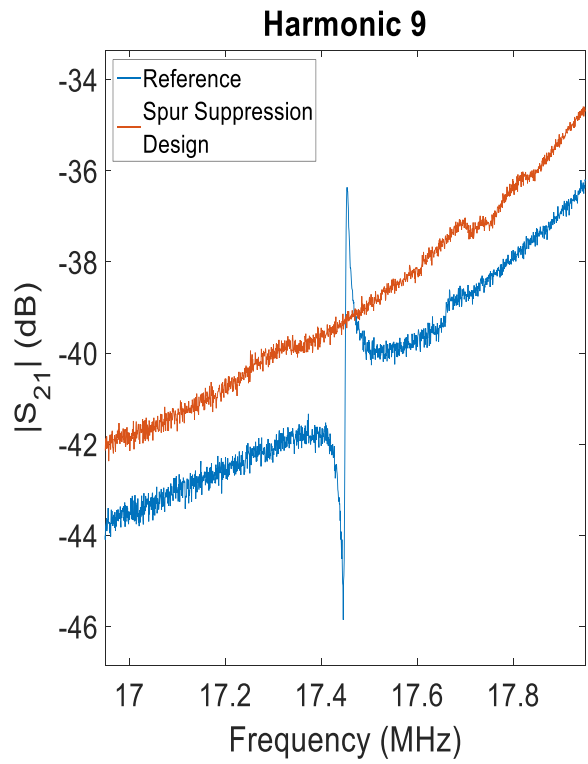


Figure 4.18a,b,c,d,e Zoom ins on the frequency responses of the targeted modes

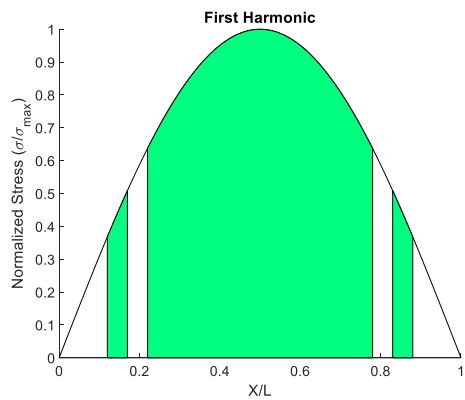


Figure 4.19 Graphical representation of the coupling of the first harmonic

4.3.2 Parametric Device Design

The ability of the RAFT to return coupling without simulating the frequency response to obtain the anti-resonance frequency makes this technique ideal for parametrically investigating the scaling of modes with design. The results of a parametric study of the scaling of R_m , $\max |S_{21}|$, k_{eff}^2 , resonant frequency f_r , and figure of merit (FOM) with disk radius (r_{disk}) and the silicon thickness (t_{Si}) are presented for a disk flexure resonator (DFR) [65].

The model was validated against measurements of devices consisting of six electrically parallel DFRs using measured Q_m and extracted on-wafer e_{31} (Figure 1.7). Since this work is only concerned with the (1,1) disk flexure mode, spurious modes were not modeled in these measurements, and are the largest source of discrepancy.

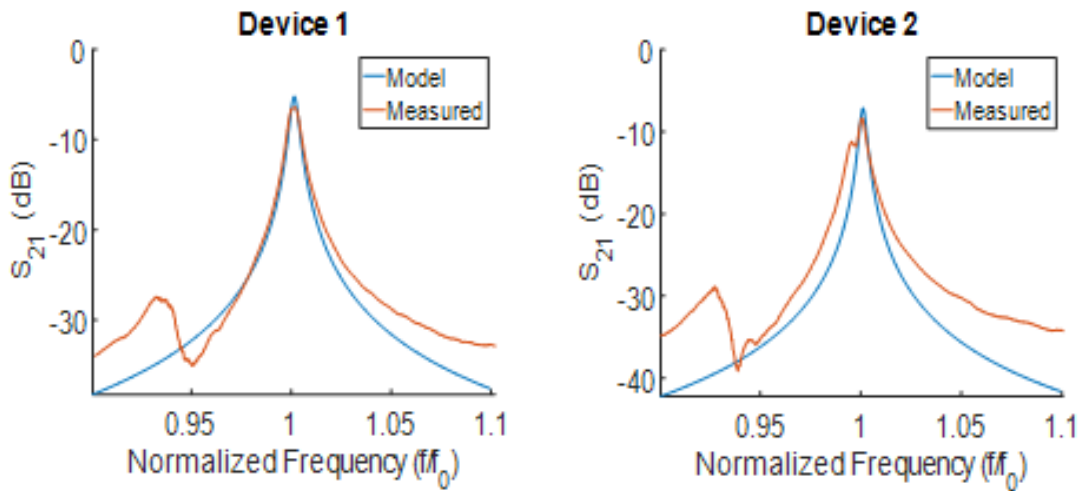


Figure 4.20 Validation of the model against 6 disk flexure resonators electrically in parallel

To address the fact that mechanical quality factor is often not known before fabrication, a “volumetric” material quality factor (Q_{mat}) was derived dependent on material loss, thickness, and stress profile and is given by

$$Q_{mat} = \frac{Y_1 y^3|_{h_0}^{h_1} + Y_2 y^3|_{h_1}^{h_2} + \dots + Y_n y^3|_{h_{n-1}}^{h_n}}{\frac{Y_1}{Q_1} y^3|_{h_0}^{h_1} + \frac{Y_2}{Q_2} y^3|_{h_1}^{h_2} + \dots + \frac{Y_n}{Q_n} y^3|_{h_{n-1}}^{h_n}} \quad (4.7)$$

Where Y_n is the elastic modulus of the n^{th} , y is the distance from the neutral axis, h_n is the distance of the top of the n^{th} layer from the neutral axis, and Q_n is the material quality factor of the n^{th} layer. A schematic of the geometric parameters for a PZT on silicon stack may be seen in Figure 4.21.

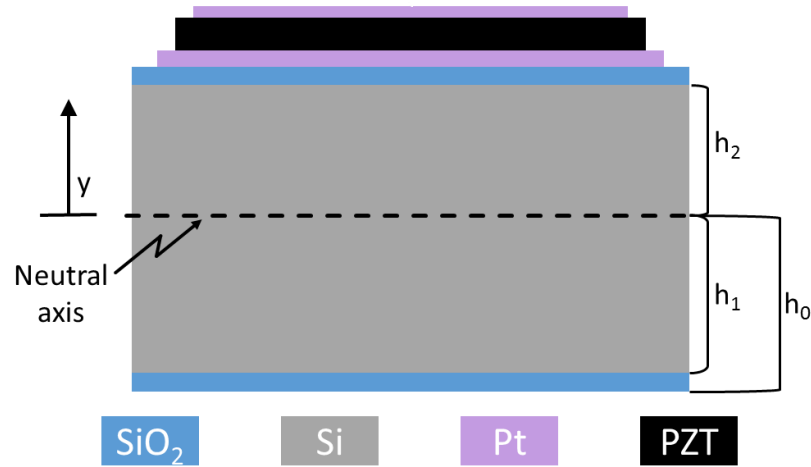


Figure 4.21 A schematic of the PZT-on-silicon stack

Assigned material quality factors for silicon dioxide, silicon, platinum and PZT in that order were: 100, 1e5, 100, and 200. In addition, a “limiting” Q_{lim} of 750 was added to the resonator to avoid abnormally high Q_m .

$$Q_m = \frac{Q_{mat} \cdot Q_{lim}}{Q_{mat} + Q_{lim}} \quad (4.8)$$

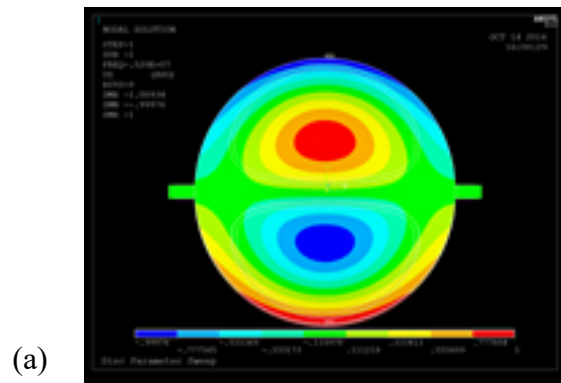
For accurate and realistic simulation, required parameters were measured, extracted from test structures, or taken from design for use in the tether, and shunt impedances of the mBVD. The elastic moduli of the material stack were independently measured [61], and densities were taken from bulk measurements. Piezoelectric coefficients were set to 10 C/m^2 , a value within the range extracted from on-wafer cantilever test structures. Tether resistances were derived from designed dimensions and resistivity test structures, and permittivity was extracted from fabricated devices. Lateral dimensions for model validation were taken from design, and layer thicknesses were taken from nominal deposition thicknesses.

To parametrically explore the design space of DFRs, 250 simulations to generate S parameters were run at various r_{disk} and t_{Si} for a total simulation time of 27 hours, or 6.5 minutes per simulation. r_{disk} varied from 12 to 60 μm , and t_{Si} varied from 1 to 10 μm .

Contour plots of the performance parameters extracted from the simulations versus t_{Si} and r_{disk} may be seen in Figure 4.23. Figure 4.23c,d,e indicate that $\max|S_{21}|$, R_m , k_{eff}^2 , and FoM are all primarily determined by the t_{Si} , and nearly constant across r_{disk} . This agrees with the result from (2.71), in which an analytical expression for the R_m of the (1,1) mode of disk flexure is presented. Given this, devices with similar performance parameters may be designed across a wide range of frequencies by adjusting r_{disk} (Figure 4.23f). Figure 4.23b indicates that for single resonators, the lowest R_m and $\max|S_{21}|$ that may be obtained are at higher t_{Si} . However, when disks are placed electrically in parallel to obtain approximately 50Ω shunt reactance, the lowest loss of $\sim 0.5 \text{ dB}$ occurs at $\sim 2.5 \mu\text{m}$ t_{Si} across all r_{disk} (Figure 4.23c). This region coincides with the region of optimal FoM in Figure 4.23e. This result stems from properties of the PZT-on-silicon stack and

flexure based resonators. By adding silicon, a high Q_m material, to PZT, a low Q_m material, the resonator coupling is reduced, while the overall resonator Q_m increases. At zero t_{Si} , there should be no coupling since the neutral axis would coincide with the mid-plane of the piezoelectric layer, and no bending moment would exist. At large t_{Si} , most of resonator would be a non-piezoelectric, and coupling would be minimized. Therefore, there must be an optimal t_{Si} for maximized FOM , which simulations suggest are $\sim 2.5 \mu\text{m}$ and 35, respectively, with a Q_m of 580.

The upper frequency limit for high performance disks occurs around 100 MHz. At these frequencies, the r_{disk} is less than 2.5 times t_{Si} . The mode transforms and begins to store more energy in in-plane shear, which is not directly transduced by PZT. The effects of this may be seen in the upper left hand corner of Figure 4.23a,b,c,d,e, where the performance metrics sharply dip. A comparison of the displacements of a mode with favorable and unfavorable r_{disk}/t_{Si} is shown in Figure 4.22.



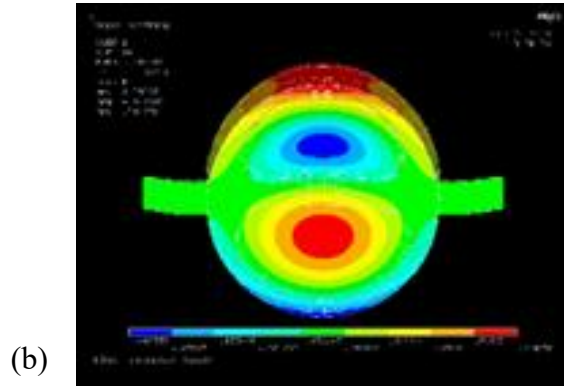


Figure 4.22 (a) a mode which as a favorable thickness-to- radius ratio and (b) a disk with unfavorable thickness-to-radius ratio. The effects of these unfavorable characteristics may be seen in Fig. 4.23a,b,c,d,e, which are largely the result of the increased presence of shear in the mode.

The RAFT accurately predicted the performance of the device from [3] despite using a nominal e_{31} of -10 C/m^2 and an analytically modeled Q_m , with an included limiting Q , to predict R_m . The relative permittivity was also set to a typical value of 440, which is valid up to several gigahertz. Resonator performance parameters for the simulated and fabricated device may be seen in Table 4.4. This shows that the RAFT can effectively predict the performance of low loss devices, even without properties extracted from test structures.

Table 4.4 Comparison of fabricated -1 dB resonator and the simulated RAFT resonator

	<i>Fabricated Device</i>	<i>Simulated Device</i>
Maximum S_{21} (dB)	-1	-1.28
k_{eff}^2 (%)	2.09	1.95
Q_m	815	741
Figure of Merit ($k_{eff}^2 \cdot Q_m$)	16.9	14.73
R_m (Ω)	9	7.5

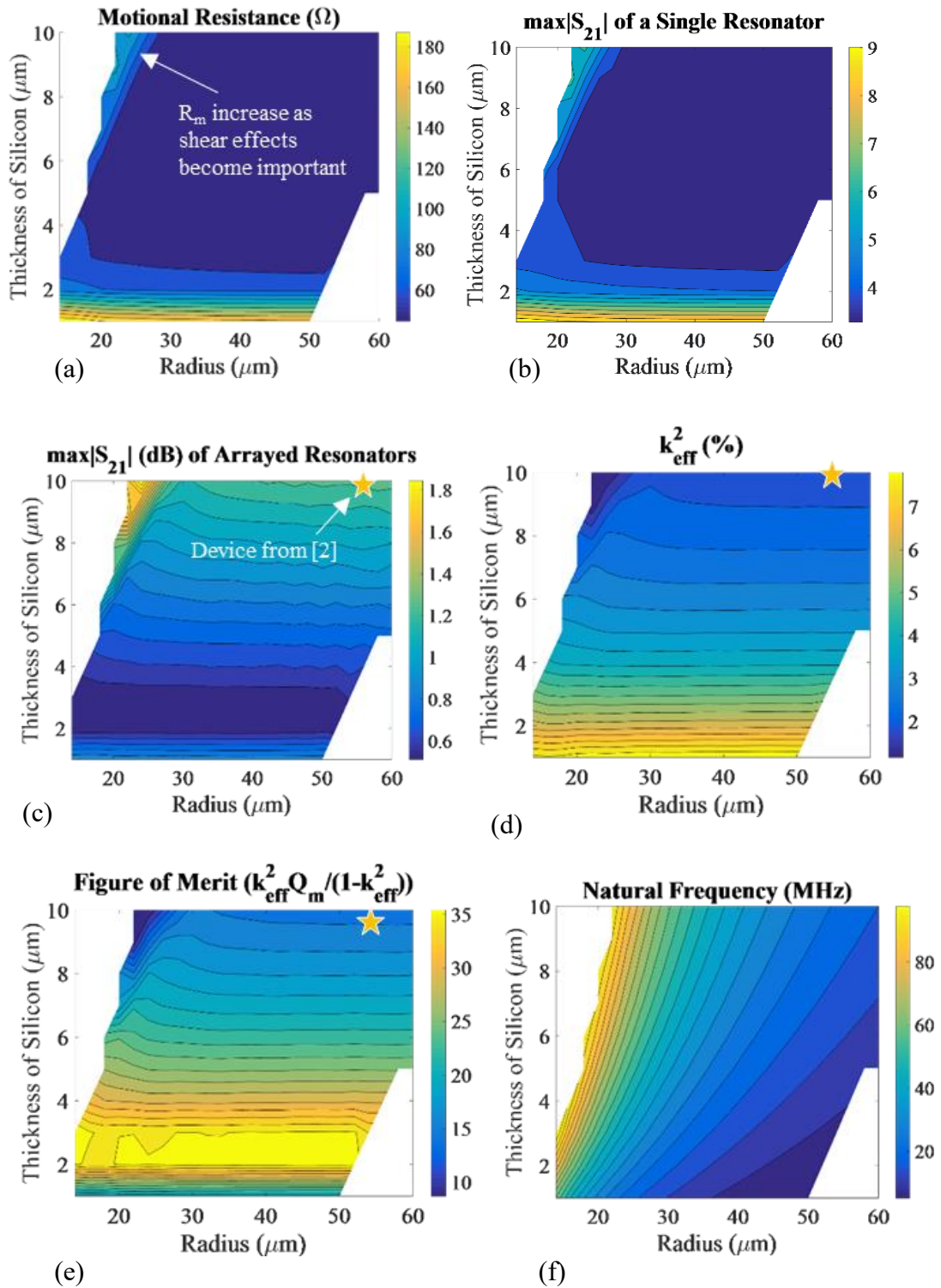


Figure 4.23 Contour plots of the behavior of disc resonators as radius and silicon thickness are varied

4.4 RAFT Discussion

4.4.1 Comparison to COMSOL®

The RAFT has been demonstrated to accurately model the frequency response of piezoelectric resonators in impressively short times. However, so far there have been no direct comparisons to conventional FEA software. To establish a baseline comparison, a COMSOL simulation with a similar number of degrees of freedom to the disk flexure FEA model presented in section 3.2.2 Running a full frequency comparison in COMSOL would have taken a prohibitively long time and potentially filled up the hard drive. Instead, several short runs were run of less than 20 frequency points, the time per frequency point was calculated, and the results were linearly extrapolated. It was assumed that each frequency point takes the same amount of time to simulate, since they are approached in a serial manner by the solver. This represents a low-end estimate of the total time the simulation would take. This is because as the simulation memory requirements become larger than the available RAM, the program write information to the hard drive, which is a much slower process. The results of the analysis are presented in Table 4.5. At the lower end of these simulations, the RAFT is ~1200 times faster than harmonic analysis.

Table 4.5 A Comparison of COMSOL and RAFT Simulation Times

<i>Points</i>	<i>Frequency Resolution</i>	<i>COMSOL Simulation Time</i>	<i>RAFT Simulation Time</i>	<i>t_{COMSOL}/t_{RAFT}</i>
9900	10 kHz	~10d 5h 30m	11.7m	1259
49500	2 kHz	~54d 10 h	11.7m	6697
99000	1 kHz	~112d 7h	311.7m	13820

For reference the simulation with 9900 points taking 10 days would place approximately 3.5 frequency points in the 3 dB bandwidth of the intended mode of Figure 4.5.

4.4.2 Qualitative Comparison to Coventorware®

Coventorware ® , an FEA modeling package which claims to improve harmonic simulations times of piezoelectric devices significantly as well, was not available for direct comparison. Coventorware takes a different approach to the simulation. An Eigen analysis is first run, and these are subsequently used to reduce the dimension of the mass and stiffness matrices using an algorithm involving the Eigen vectors. The effect of this is to exclude simulation of any modes which are not electrically excited or detected. This significantly reduces the computational load, as these matrices tend to be much smaller. Finally, using knowledge of the locations of the natural modes to select frequency points, a harmonic analysis is run with the reduced mass and stiffness matrices. More details may be found in [66]

4.4.3 Gyroscopes

The transfer function from applied voltage to output charge is

$$\frac{V}{F_m} \cdot \frac{F_m}{\delta} \cdot \frac{\delta}{u} \cdot \frac{u}{S} \cdot \frac{S}{sQ} \quad (4.9)$$

This transfer function can be modified to include the Coriolis Effect. The displacement, and therefore velocity, is obtained from (2.25). The velocity is then turned into a force on the sense mode through the Coriolis force, $F_C = -2\Omega \times v$,

where Ω is the angular velocity, and v is the velocity. The sense mode then produces charge, and the overall transfer function is

$$\frac{V}{F_m} \cdot \frac{F_m}{\delta} \cdot \frac{\delta_1}{su_1} \cdot \frac{su_1}{F_c} \cdot \frac{F_c}{\delta_2} \cdot \frac{\delta_2}{S_2} \cdot \frac{S_2}{sQ} \quad (4.10)$$

Utilizing the RAFT in a similar manner here, but with the additional transfer functions for the Coriolis force, could result in a dramatic speed up of the simulation of piezoelectric MEMS based gyroscopes.

4.4.4 Ultrasonic Motors

Ultrasonic motors are of interest as actuators due to their small size, low speeds and high torques. They can produce both linear and rotatory motion [67].

Often, designers are interested in the real displacement of the ultrasonic motor. Equation (2.25), with the temporal portion of the displacement included, predicts the displacement directly from an applied electric field and a known strain mode shape. Excellent work has been done in [50] presents expression for the unloaded and loaded motor's displacement. These expressions agree with the expression presented in this work when appropriate modifications are made.

4.4.5 Strain Sensors

Piezoelectric strain sensors work by creating an output current after the object being sensed transfers some strain to the piezoelectric material. Equation (2.30) can directly be used to predict the charge and relate it directly back to the strain that produced it.

Strain sensors present several challenges that required further modeling, such as bond layers to the substrate distorting the transmitted strain.

4.4.6 PMUTs

Piezoelectric Micromachined Ultrasonic Transducers (PMUTs) are generally based upon lower frequency flexural modes for acoustic impedance matching to air and fluids. Air coupled PMUTS have applications such as gesture recognitions, ranging, autofocusing, and gas metering. Fluid coupled PMUTs are applicable towards medical imaging and fingerprint sensing. Equation (2.25) can be used for the modeling of the displacement of these resonators.

4.4.7 Energy Harvesters

Equation (2.30) can be used to model the charge created by a piezoelectric energy harvesting element. The strain caused by an inertial forces must first be modeled, but is fairly straight forward to find computational via modeling.

CHAPTER 5

CONCLUSION

5.1 Future Work

The RAFT has shown promising results for the rapid simulation of linear piezoelectric MEMS resonators, and applications to other systems have been discussed, such as ultrasonic motors and PMUTs. This has opened avenues of exploration for the maturation of this technology.

The RAFT has yet to be tested on bulk acoustic wave and surface acoustic wave resonators. Bulk acoustic waves tend to operate at frequencies above 1 GHz, and there may be some unforeseen challenges in simulation in the domain. However, there are no obvious reasons why the RAFT should not model bulk acoustic resonators.

The original spirit of the RAFT is towards a computational solution to the spurious mode problem in piezoelectric MEMS resonators. Proof-of-concept fabricated resonators point in the possible direction of rapid electrode design with the aid of the RAFT. An algorithmic approach to spurious mode suppression would be the ideal use case for RAFT.

The RAFT could also potentially be used to model thermal effects. Dielectric losses, viscous losses, thermo-elastic losses, and Ohmic losses contribute to heating of resonators. Running a thermal simulation to model the stresses induced on the resonator would allow designers to quickly predict the frequency shifting effects on the frequency bandwidth.

Piezoelectric stiffening has yet to be incorporated in the RAFT [68]. Piezoelectric stiffening is a result of electrical boundary conditions. The deformation of the piezoelectric results in charge accumulation on the electrodes. In the case where the electrodes are electrically separated, the Coulombic forces resist compression of the piezoelectric. This results in an increase in apparent stiffness. In the shorted case, there is no net potential between the top and bottom electrodes, and the resulting stiffness is from purely elastic effects. An illustration of these two cases may be seen in Figure 5.1. The stiffening in a resonator is not quite as straightforward as these simple cases, as a perfect short or perfect open is not obtained in actual device operation.

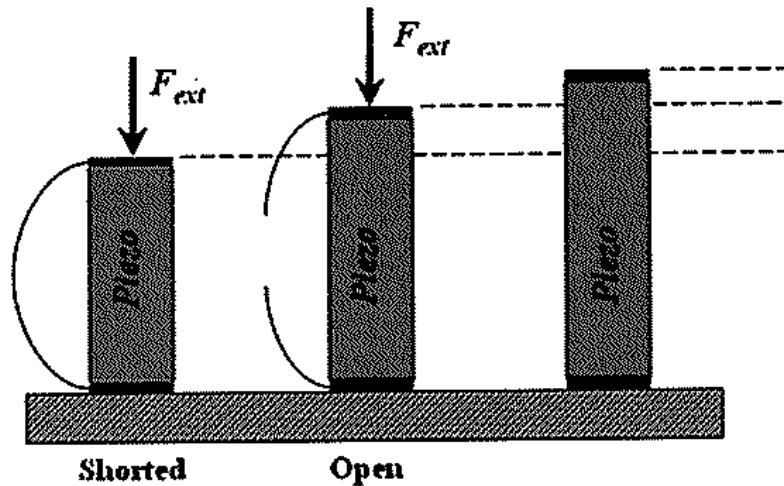


Figure 5.1 Illustration of the effects of piezoelectric stiffening [37]

5.1.1 Applicability to Other Transduction Methods

The methodology of the RAFT may also be used to model other methods of transduction for which energy enters the mechanical domain. These include piezomagnetically and capacitively transduced systems. The conversion of voltage to force and displacement to charge equations were derived via energy methods. Similar

analysis may be applied to other systems. In fact, this is how electrostatic MEMS devices are modeled; the force from a capacitive plate, and the current out are derived in a similar fashion [69]. In general, the first and last transfer functions in (4.10) must be replaced with the proper conversion from the input forcing parameter to modal force and strain to the output sense parameter.

5.1.2 Quality Factor Modeling

In the preceding work, quality factor was generally treated as its own variable and not modeled with good reason. There are several important loss mechanisms in MEMS resonators discussed in 4.1.1 and reasons were given for quality factor not being modeled in this work. However, in the future techniques for the modeling of quality factor can be included. Damped modal analyses exist using viscous and structural damping. Structural damping is proportional the amplitude of displacement, but 90 degrees out phase (i.e. in phase with the velocity). Viscous damping is proportional to the velocity of vibration. Thermoelastic damping can also potentially be modeled for each mode. Another common technique for anchor loss modeling is to use perfectly matched layers (PMLs). These layers ideally absorb all energy incident on them in an attempt to imitate an infinite medium. An alternative implementation for modeling anchor loss conducive to modal analysis may be included in the RAFT. In this analysis, the released regions are modeled and fully clamped at the edge. The energy leaving the resonator is compared to the energy stored in the resonator, and a loss due to the anchors is calculated.

5.2 Summary of Contribution to the Body of Work

This work has presented a new methodology for modeling of the frequency response of piezoelectric MEMS resonators. This was enabled by generalized expressions for the motional parameters of the mBVD model and coupling, which have been presented by this author for the first time. The expressions are material, mode and topology agnostic. These parameters were validated using analytical mode shapes, as well as validated in the RAFT by comparing to measurement.

To obtain the frequency response in the RAFT, the mode shape, mechanical material properties, piezoelectric properties, electric field shape, and quality factor must be known. The material properties are generally taken from measurement, or are known in advance. The mode shape and electric field shape were obtained through FEA simulation in the RAFT. A modal analysis and electrostatic analysis are run, respectively, to obtain these. The quality factor is not modeled in this work.

Electrostatic and modal analyses are run, and typically complete much faster than a multi-physics analysis. The principles of modal analyses are used along with the motional parameters in the mBVD to decouple the simulation of the electrical and mechanical domain, and simulate the frequency response. Two factors contributing to the speed up by the RAFT are: the full piezoelectric equations are not solved and only frequency points where modes exist are simulated from modal analysis rather than all frequency points for which information is desired. Apart from this, the RAFT also has several other advantages: it will not miss modes, the contribution of individual modes may be extracted, the contribution of each piezoelectric constant may be extracted, the simulation may be re-run after only re-simulating the electric field if the addition or

removal of electrodes is considered a negligible perturbation, and the electromechanical coupling may be obtained without having to generate a frequency response. All the above allow the RAFT to complete much faster than conventional harmonic analyses,

The RAFT has been used to accurately simulate the wide band response of resonators when compared to measurement, explore the parametric design of resonators, and several other potential applications have been suggested. These simulations were performed orders of magnitude faster than conventional analyses, and have advantages over other fast solvers. However, there are still developments required for the model to be fully plug-and-play, such as the inclusion of piezoelectric stiffening. The future look promising for this novel, low-cost simulation technique to heavily impact how piezoelectric MEMS resonators, and other systems, are designed and analyzed.

APPENDIX A – CODE

This portion of the code is run in ANSYS APDL. Exclamation points denote comments. The /input function requests a file. The layer thicknesses, geometry, material properties, etc. are all stored in separate text files.

```
! Jonathan Puder
! September 7, 2018

FINISH          ! Exit all processors
/CLEAR,START    ! Clear the database

*get,timel,active,,TIME,WALL          ! Get
the wall time at the start of the simulation

  /MKDIR,'C:\ANSYS\Example Code\'      ! Make
a directory for saving
  /CWD,'C:\ANSYS\Example Code\'       !
Change to the created directory

/FILNAME,Full Raft_struc,1            !
Changes file name
/Prep7                                  ! Enter
preprocessor
/TITLE, Structural Simulation

et,1,solid95                            ! Element
type for structural analysis
et,2,solid122                            ! Element
type for electrostatic analysis

!!!!!! GEOMETRY PARAMETERS

  /INPUT,'Thicknesses','txt','C:\ANSYS\Run Files\',,,0
    ! Read layer thicknesses from input file

!!!!!! DRAW GEOMETRY

  /INPUT,'Geometry','txt','C:\ANSYS\Run Files\',,,0
    ! Read file to draw geometry

    allsel                                !
Select all entities
    vovlap,all                            ! Use
VOVLAP if model has overlapping volumes
```

```

!VGLUE,ALL ! Use
VGLUE if volumes do not overlap

!!!!!! MATERIAL ASSIGNMENT

      /INPUT,'MaterialAssignStruc','txt','C:\ANSYS\Run
Files\',,0 ! Assign Structural Material Properties

!!!!!! MESHING

      /INPUT,'Meshing','txt','C:\ANSYS\Run Files\',,0
! Meshes the model

!!!! BOUNDARY CONDITIONS AND LOADS

ASEL,S,Loc,X,Rou+5 !
Select Areas to be anchored. Rou is a variable created in
geometry text file
ASEL,A,LOC,X,-Rou-5 !
Select additional areas to be anchored

DA,all,ux,0
DA,all,uy,0
DA,all,uz,0 ! Set
fixed boundaries in X, Y, and Z on selected areas

nummode = 200 ! Set
the maximum number of modes to look for
fstart = 870e6 !
Set the starting frequency
fend = 1300e6 ! Set
the ending frequency

/SOLU ! Enter "Solution"
Processor (need to be in this processor to issue most
"solution" commands)
ANTYPE,2 ! Analysis type "2" = modal
analysis
EQLV,SPAR ! Set sparse solver
MXPAND,nummode, , ,1 ! "Expand" modes
LUMPM,0 ! Turn off Lumped mass
approximation
PSTRES,0 ! Turn off "prestress"
option

```

```

MODOPT,LANB,nummode,fstart,fend, ,ON          ! Solve for
modes between start and fend, ON refers to unity
normilzation (I think)

/sol                                           ! Enter solution processer
solve
/OUTPUT                                       ! "Solve" command
initiates

/POST1                                        ! Enter "General Post
Processor" (need to be in this processor to review
results)

*get,time2,active,,TIME,WALL                 ! Get the total
time at completion of solution

save,'FullRaft1','db','C:\ANSYS\Example Code\\' ! Save
the database file for later viewing

!!!! EXTRACTING AND SAVING DESIRED RESULTS

SET,1,1                                       ! Read the first mode
data
WPSTYL,DEFA                                  ! Rest the location of
working plane

VSEL,s,loc,z,tBotPt,tBotPt+tAlN             ! Select the
volume piezoelectric material
ESLV,S                                       ! Select the elements
associated with the currently selected volume

*del,EARRAY                                  ! Delete and previous
instances of EARRAY
*get,ENUMMAX,ELEM,,COUNT                    ! Get the maximum
number of the elements currently selected
*dim,EARRAY,array,ENUMMAX,5                 ! Creat and
dimension and array called EARRAY

ETABLE,VV,Volu                               ! Creates table with
information about volume and centroid location of all
selected elements
ETABLE,CX,CENT,X
ETABLE,CY,CENT,Y
ETABLE,CZ,CENT,Z

```

```

*VGET,EARRAY(1,2),ELEM,1,ETAB,VV          ! Reads the
infomration from the element table and writes into the
columns of EARRAY
*VGET,EARRAY(1,3),ELEM,1,ETAB,CX
*VGET,EARRAY(1,4),ELEM,1,ETAB,CY
*VGET,EARRAY(1,5),ELEM,1,ETAB,CZ

*CFOPEN,'E:\ANSYS\Test EMODIF
Function\Ring_teth_findfreq\ElemData',txt
! Creat/open file called "ElemData.txt"
*VWRITE,EARRAY(1,2),EARRAY(1,3),EARRAY(1,4),EARRAY(1,5)
          ! Write the columns of EARRAY into a
text file
      %G %G %G %G                               !
Format specifier for data
*CFCLOSE                                     ! CLOSE
the opened file

*DO,nn,1,nummode      ! DO loop to step through modes,
starting from mode

      /MKDIR,'C:\ANSYS\Example Code\mode%nn%' ! Make a
directory for mode 'nn'
      /CWD,'C:\ANSYS\Example Code\mode%nn%'  ! Change
directory to newly created folder

      !!!! READ STRAIN INFORMATION

      *del,SARRAY          ! DELETE any previous
instances of SARRAY
      *dim,SARRAY,array,ENUMMAX,5    ! Dimension SaRRAY

      ETABLE,EPX,EPEL,X          ! Get strain information
from currently selected elements and put in ETABLE
      ETABLE,EPY,EPEL,Y
      ETABLE,EPZ,EPEL,Z
      ETABLE,EPYZ,EPEL,YZ
      ETABLE,EPXZ,EPEL,XZ

      *VGET,SARRAY(1,1),ELEM,1,ETAB,EPX ! Get X, Y, Z,
YZ, and XZ strain information from ETABLE and write to
SARRAY
      *VGET,SARRAY(1,2),ELEM,1,ETAB,EPY
      *VGET,SARRAY(1,3),ELEM,1,ETAB,EPZ
      *VGET,SARRAY(1,4),ELEM,1,ETAB,EPYZ
      *VGET,SARRAY(1,5),ELEM,1,ETAB,EPXZ

```

```

        *CFOPEN,'C:\ANSYS\Example Code\mode%nn%\strain',txt
! Open file called "Strain.txt"

        *VWRITE,EARRAY(1,1),EARRAY(1,2),EARRAY(1,3),EARRAY(1
,4),EARRAY(1,5)                ! write strain
information to newly created file
        %G %G %G %G %G
                                ! Format specifier
        *CFCLOSE

        !!!!! ENERGY !!!!!!!!!!!!!
        ALLSEL                    ! Select all entities
        ESLV,S                    ! Select elements associated
with those entities
        *get,ENUMMAX,ELEM,,COUNT ! Get the maximum
number of the elements currently selected

        *del,EARRAY                ! Delete and
previous instances of EN
        *dim,EN,array,ENUMMAX,1    ! Dimension
EN to include all elements

        ETABLE,KE,KENE            ! Write KE of all
elements to the element table
        *VGET,EN,ELEM,1,ETAB,KE   ! Get the
kinetic energies of all elements and write to EN
        *VSCFUN,TotKE,SUM,EN     ! Sum up EN
to get total kinetic energy

        *GET,fn,ACTIVE,0,SET,FREQ ! Get the
natural frequency of current mode

        *cfopen,'C:\ANSYS\Example Code\mode%nn%\FreqEn',txt
! Open file called "FreqEn.txt"

        *vwrite,TotKE,fn          ! Write ToKE and fn to
file
        %G %G                    ! Format specifiers
        *cfclos                  ! Close file

        SET,next ! Move onto next mode

*ENDDO                ! END the do loop

```

```

*get,time3,active,,TIME,WALL      ! Get wall time for
the total amount of time the simulation took

*CFOPEN,'SimTime','txt',        ! Open a text file callsed
SimTime
*VWRITE,time1,time2,time3      ! Write the saved times to
this file
    %G %G %G                  ! Format specifier
*CFCLOSE                        ! CLOSE the opened file

!***** START CMATRIX CODE
*****
***
!*****
*****

! The beginnign part of this code reads many of the same
files as the structural code. This is purposefully done
to avoid
! Any errors and ensure the geometry and mesh are exactly
the same

FINISH        ! Exit all processers
/CLEAR,START  ! Clear the database

*get,time1,active,,TIME,WALL      !
Get the wall time at the start of the simulation

    /MKDIR,'C:\ANSYS\Example Code\'
    ! Make a directory for saving
    /CWD,'C:\ANSYS\Example Code\'
    ! Change to the created directory

    /FILENAME,Full Raft_cap,1
    ! Changes file name
    /Prep7                                     ! Enter
preprocessor
    /TITLE, Electrical Simulation

    et,1,solid95                               !
Element type for structural analysis
    et,2,solid122                               !
Element type for electrostatic analysis

!!!!!! GEOMETRY PARAMETERS

```

```

/INPUT,'Thicknesses','txt','C:\ANSYS\Run Files\',,,0
    ! Read layer thicknesses from input file

!!!!!! DRAW GEOMETRY

/INPUT,'Geometry','txt','C:\ANSYS\Run Files\',,,0
    ! Read file to draw geometry

allsel
vovlap,all                                ! Use
VOVLAP if model has overlapping volumes
!VGLUE,ALL                                ! Use
VGLUE if volumes do not overlap

!!!!!! MATERIAL ASSIGNMENT

/INPUT,'MaterialAssignElec','txt','C:\ANSYS\Run
Files\',,,0    ! Assign Structural Material Properties

allsel

!!!!!! MESHING

/INPUT,'Meshing','txt','C:\ANSYS\Run Files\',,,0
    ! Meshes the model

!!!!!!!!!!!!!!!!!!!!

NUMCMP, VOLU ! compress the volume numbering
allsel

VSEL,S,VOLU,,19 ! Select volume associated with input
electrode
VSEL,A,VOLU,,16
VSEL,A,VOLU,,7
VSEL,A,VOLU,,5
VSEL,A,VOLU,,6
VSEL,A,VOLU,,8

VSEL,A,VOLU,,71
VSEL,A,VOLU,,72
VSEL,A,VOLU,,41
VSEL,A,VOLU,,43
VSEL,A,VOLU,,42
VSEL,A,VOLU,,44

```

```

NSLV,S,1 ! Select nodes associated with selected volumes

cm,cond1,node ! Assign node component to 1st
conductor

!!!!!!!!!!!!!!

VSEL,S,VOLU,,10 ! Select volume associated with
ground electrode
VSEL,A,VOLU,,13
VSEL,A,VOLU,,3
VSEL,A,VOLU,,1
VSEL,A,VOLU,,2
VSEL,A,VOLU,,4

VSEL,A,VOLU,,69
VSEL,A,VOLU,,70
VSEL,A,VOLU,,37
VSEL,A,VOLU,,39
VSEL,A,VOLU,,38
VSEL,A,VOLU,,40

NSLV,S,1 ! Select nodes associated with selected volumes

cm,cond2,node ! Assign node component to 2nd
conductor. Must have same label (i.e. cond) as previous
conductor

/solu ! Enter solution processor
cmatrix,1,'cond',2,0 ! Compute capacitance matrix
coefficients. 'cond' is name of conductors, 2 is number
of conductors,
! and 0 indicates that ground is one of
the conductors
/POST1 ! Enter postprocessor

!!!!!!!!!!!!!!!!!!!!!!!!!!!! INTERROGATE THE RESULTS

WPSTYL,DEFA
SET,1,1 ! Set first solution step

VSEL,S,loc,z,tBotPt,tBotPt+tAlN ! Select pizeoelectric
material
ESLV,S

```

```

ETABLE,VV,Volu      ! Write store volume, electric field
components, and element centers in ETABLE
ETABLE,EFX,EF,X
ETABLE,EFY,EF,Y
ETABLE,EFZ,EF,Z
ETABLE,CX,CENT,X
ETABLE,CY,CENT,Y
ETABLE,CZ,CENT,Z

*get,ENUMMAX,ELEM,,COUNT ! Get maximum number of elements

*del,EARRAY          ! Delete any previous instances
of EARRAY
*dim,EARRAY,array,ENUMMAX,7    ! Dimension EARRAY

*VGET,EARRAY(1,1),ELEM,1,ETAB,VV
*VGET,EARRAY(1,2),ELEM,1,ETAB,CX
*VGET,EARRAY(1,3),ELEM,1,ETAB,CY
*VGET,EARRAY(1,4),ELEM,1,ETAB,CZ
*VGET,EARRAY(1,5),ELEM,1,ETAB,EFX
*VGET,EARRAY(1,6),ELEM,1,ETAB,EFY
*VGET,EARRAY(1,7),ELEM,1,ETAB,EFZ

/MKDIR,'C:\ANSYS\Example Code\EFIELD'      ! Make a
directory for the file
*cfopen,'C:\ANSYS\Example Code\eFieldFile',txt      !
OPEN a file called eFiledFile

*vwrite,EARRAY(1,1),EARRAY(1,2),EARRAY(1,3),EARRAY(1,4),E
ARRAY(1,5),EARRAY(1,6),EARRAY(1,7) ! WRITE the data to
file
      %G %G %G %G %G %G %G
*CFCLOSE          ! CLOSE the opened file

/eof      ! END OF FILE

```

The program has now created a series of folders with information about the strain and electric field at the center of each elements, as well as total energies and natural frequencies. This is then read into MATLAB, example code of which is given below.

% denotes comments.

```

clear all
close all
home = cd;
for num = 2

path1 = % string containing folder with all mode
data
path2 = % string containing folder with electric
field data
cd(path2)
EField = importdata('eFieldFile.txt',' ');
C0 = importdata('Cmat.txt',' '); % Import value of
ground capacitor from electrostatic simulation
    Data.Vol2 = EField(:,1); % Volume data from
electrostatic(ES) simulation
    Data.cx2 = EField(:,2); % center x coordinate from
ES
    Data.cy2 = EField(:,3); % same as above, but y
    Data.cz2 = EField(:,4); % same as above, but z
    Data.Ex = EField(:,5)/100; % X electric field data
normalized by the magnitude of 100
    Data.Ey = EField(:,6)/100; %same as above, but for
Y
    Data.Ez = EField(:,7)/100; same as above, but for
Z

    e31 = -0.58;e32 = -0.58;e33 = 1.55;e24 = -
0.48;e15 = -0.48; % piezoelectric constants of
aluminum nitride

cd(home)
h = getSubFolders(path1); % Custom function which
retrieves the name of all subfolders
cd(path1) % change current directory to modal data

ElemData = importdata('ElemData.txt',' '); % import
text file with element data

    Data.Vol = ElemData(:,1); % data about volume of
each element form modal analysis, should be the same
as Data.Vol2 from ES simulation

```

```

    Data.cx = ElemData(:,2); % should be same as
Data.cx2
    Data.cy = ElemData(:,3); %'' '' '' cy2
    Data.cz = ElemData(:,4); % '' '' '' cz2
    Data.C0 = C0*1e-12;

for i = 1:length(h)

    if h(i).name(1:4) ~= 'mode' % make sure the folder
will contain modal data
        continue
    end

    c = str2double(h(i).name(5:end));

    cd([path1 sprintf('mode%d',c)])
    Data.mode(c).modenum = c; % save the mode number
to a structure

    strain = importdata('Port1.txt',' '); % import the
strain data from the relevant text file

    epX = strain(:,1); % save the strains to
descriptive variable name
    epY = strain(:,2);
    epZ = strain(:,3);
    epYZ = strain(:,4);
    epXZ = strain(:,5);

    FreqEn = importdata('FreqEn.txt',' '); % get
frequency and energy

    Data.mode(c).maxdisp = FreqEn(3); % store max
displacement
    Data.mode(c).f = FreqEn(2); % store frequency

    aa = importdata('Energy.txt');
    Energy = str2double(aa.textdata{5,4}); % get
value of total energy

cd(home);

```

```

Data.mode(c).KE = Energy;
Data.mode(c).km = 2*Data.mode(c).KE; % compute modal
spring

% calculate the transduction from each
piezoelectric constant for each element
comp1 = e31*epx .*Data.Ez;
comp2 = e32*epy .*Data.Ez;
comp3 = e33*epz .*Data.Ez;
comp4 = e24*epyz.*Data.Ey;
comp5 = e15*epxz.*Data.Ex;

% Add up the transduction from each element
Data.mode(c).comp1 = sum(comp1.*Data.Vol);
Data.mode(c).comp2 = sum(comp2.*Data.Vol);
Data.mode(c).comp3 = sum(comp3.*Data.Vol);
Data.mode(c).comp4 = sum(comp4.*Data.Vol);
Data.mode(c).comp5 = sum(comp5.*Data.Vol);

% get the total transduction from each element
Data.mode(c).int =
sum((comp1+comp2+comp3+comp4+comp5).*Data.Vol);
% Multiply by 1e12 to convert from microMKS to
MKS
% This is the Rm without quality factor
Data.mode(c).Rm =
1e12*Data.mode(c).km/(2*pi*Data.mode(c).f*(Data.mode(
c).int)^2);

Cm = ((Data.mode(c).int)^2)/(Data.mode(c).km);
Data.mode(c).keff = Cm/(C0+Cm); %
electromechanical coupling

end
fname =
(sprintf('Wide_n3_R70_deg0_4.8_pitch_BUS.mat',num))

save(fname,'Data'); % name the data set and save the
file
close(hand)

cd(home)

```

end

A data structure has now been created which contains all of the R_m , L_m , C_m , C_0 and K_{eff}^2 of the resonator. The next step is to simulate the mBVD, an example of which is given in the following code.

```
clear all
close all
home = cd;

    load(string with file name goes here)

    freq = 865e6:3e3:909e6; % Simulation bandwidth of
interest
    om = 2*pi*freq; % change hertz to rad/s

    C0 = .6e-12; % set the shunt cap value
for ind = 1:length(Data.mode) % step through all
modes

    St = Data; % rename structure for convenience

        Qm = 3000; % set the Qm of all modes. It is
possible to set the Qm for each individual mode, or
take this value from simulation

        Zm = 0; Rm = 0; Cm = 0; Lm = 0; % initialize
values
        Rm = St.mode(ind).Rm/(Qm); % calculate Rm with Qm
included

        Cm = 1./(2*pi*St.mode(ind).f*Qm.*Rm); % calculate
Cm and Lm. This can also be read directly from the
file
        Lm = Qm*Rm./(St.mode(ind).f*2*pi);

        Zm = Rm + 1./(1i*Cm.*om) + 1i*Lm.*om; % calculate
the impedance of the motional arm
        Ym(ind,:) = 1./Zm; % convert to admittance
```

```
end
YC0 = 1i*C0*om;
    Ytot = sum(Ym); Sum up all the parallel motional
arms

    Yall = Ytot+YC0; % add in the shunt capacitance
admittance

    Ydb = 20*log10(abs(Yall)); % convert to dB

    plot(freq/1e6,Ydb,'LineWidth',2)% plot the
simulated data

home = cd;
```

The above code outlines important commands and the procedure to go from FEA simulation to frequency response.

APPENDIX B – Disk Cross-Sectional Lamé Mode Resonators

Ring CLMRs are of interest due to their potential for a lower spurious response than their bar-like counterparts. As such, the designs were investigated using the RAFT in collaboration with the Northeastern Sensors and Nano Systems Laboratory. The parameters investigated include pitch of electrodes, the number of rings, the percentage of the pitch covered by electrode, and the inner radius of the ring (Figure A.1). Simulations were run with perfectly symmetrical rings and electrodes, and example of the spurious-free response may be seen in Figure A.2. In reality this topology is not possible due to the need to create electrical connections and avoid shorts. The results are included in the tables below. All simulations were performed with 100 nm bottom and top platinum electrodes and 4 μm of AlN. Interestingly, the designs with the highest coupling were single ring devices. They should also produce much smaller spurious mode response due to their symmetry, and the fact that the electrodes form complete rings, which is not true of higher order harmonics. Additionally, it may be advantageous to cover a larger portion of the resonator with electrode since there is no issue with fringing capacitance. This possibility was not investigated. These devices were not investigated due to the sidewall angle issues in the aluminum nitride fabrication process.

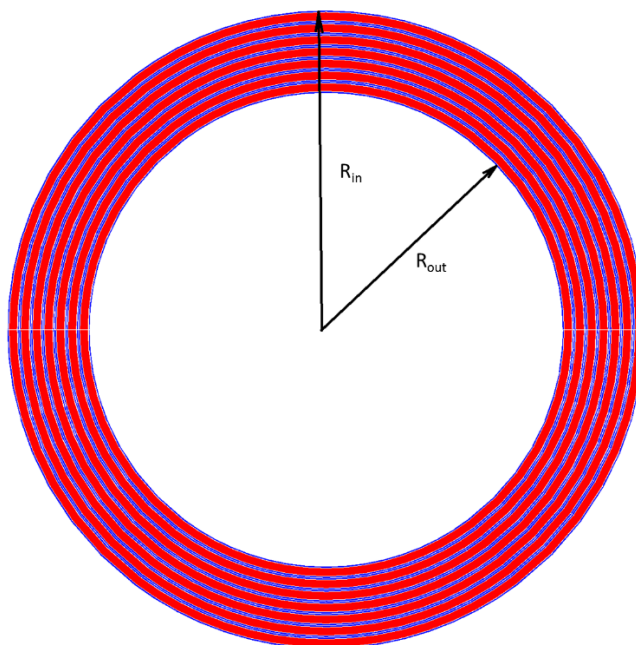


Figure A.1 Top view of ring resonator with 7 rings. The inner and outer radii are indicated. The red areas are the locations of the electrodes, and the blue areas are aluminum nitride

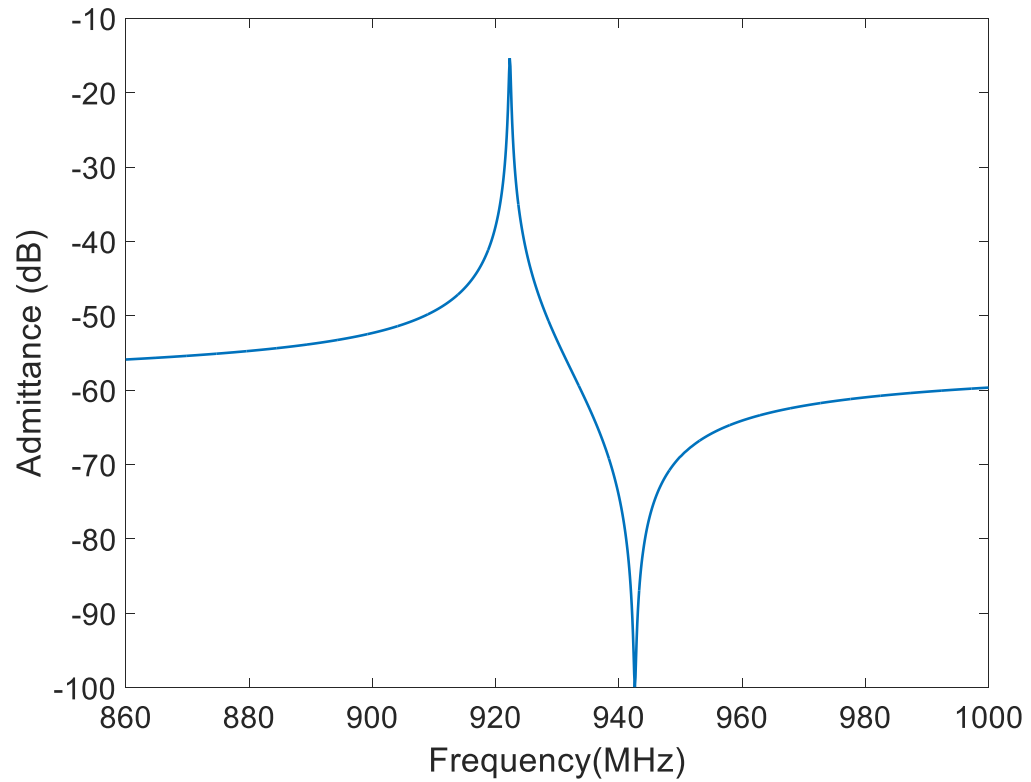


Figure A.2 The spur-free response obtained by utilizing perfectly symmetrical rings without anchors or bus

Table A. 1 Simulation results of investigation of pitch on CLMR performance

Pitch (um)	# Rings	% Coverage	C0 (F)	Cm (F)	k_{eff}^2	f _r (MHz)	R _{in}	R _{out}
4.1	3	60	2.11E-13	4.15E-15	1.93	951.4	100	112.3
4.2	3	60	2.14E-13	6.43E-15	2.92	944.7	100	112.6
4.3	3	60	2.16E-13	7.55E-15	3.37	937.7	100	112.9
4.4	3	60	2.19E-13	8.13E-15	3.58	930.3	100	113.2
4.5	3	60	2.22E-13	8.56E-15	3.72	922.3	100	113.5
4.6	3	60	2.25E-13	8.89E-15	3.81	913.8	100	113.8
4.7	3	60	2.27E-13	9.12E-15	3.86	904.8	100	114.1
4.8	3	60	2.30E-13	9.26E-15	3.87	895.2	100	114.4

4.9	3	60	2.33E-13	9.31E-15	3.84	885	100	114.7
5	3	60	2.36E-13	9.30E-15	3.79	874.4	100	115

Table A. 2 Simulation results of investigation of number of rings on CLMR performance

Pitch (um)	# Rings	% Coverage	C0 (F)	Cm (F)	k_{eff}^2	f_r (MHz)	Rin	Rout
4.8	1	60	6.33E-14	3.28E-15	4.92	895.06	100	104.8
4.8	2	60	1.45E-13	6.17E-15	4.09	895.14	100	109.6
4.8	3	60	2.30E-13	9.26E-15	3.87	895.18	100	114.4
4.8	4	60	3.19E-13	1.24E-14	3.74	895.2	100	119.2
4.8	5	60	4.12E-13	1.58E-14	3.69	895.21	100	124
4.8	6	60	5.08E-13	1.90E-14	3.61	895.22	100	128.8

Table A. 3 Simulation of effect of electrode coverage on the CLMR

Pitch (um)	# Rings	% Coverage	C0 (F)	Cm (F)	k_{eff}^2	f_r (MHz)	Rin	Rout
5	7	30	4.07E-13	1.47558E-14	3.50	905.72	100	135
5	7	40	4.78E-13	1.79832E-14	3.63	893.46	100	135
5	7	50	5.49E-13	2.2075E-14	3.86	883.23	100	135
5	7	60	6.27E-13	2.63414E-14	4.03	874.45	100	135
5	7	70	7.26E-13	1.43492E-14	1.94	865.85	100	135
5	7	80	8.44E-13	1.36807E-14	1.60	854.80	100	135
5	7	65	6.70E-13	2.28486E-14	3.30	870.21	100	135

5	7	67	6.89E-13	2.32293E-14	3.26	868.50	100	135
5	7	55	5.87E-13	2.43438E-14	3.98	878.72	100	135
5	7	57	6.03E-13	2.51804E-14	4.01	876.99	100	135
5	7	59	6.19E-13	2.59682E-14	4.03	875.29	100	135
5	7	61	6.36E-13	2.66995E-14	4.03	873.61	100	135
5	7	63	6.53E-13	2.73644E-14	4.02	871.93	100	135

Table A. 4 Investigation of ring inner radius on performance of CLMR

Pitch (um)	# Rings	% Coverage	C0 (F)	Cm (F)	k_{eff}^2	f _r (MHz)	Rin	Rout
4.8	1	60	3.24E-14	1.68E-15	4.92	905.72	50	54.8
4.8	1	60	3.86E-14	2.00E-15	4.92	893.46	60	64.8
4.8	1	60	4.47E-14	2.32E-15	4.92	883.23	70	74.8
4.8	1	60	5.09E-14	2.64E-15	4.92	874.45	80	84.8
4.8	1	60	5.71E-14	2.96E-15	4.92	865.85	90	94.8
4.8	1	60	6.33E-14	3.28E-15	4.92	854.80	100	104.8

After the design space as investigated, a low ring number, with 60% electrode coverage with a pitch of 4.8 μm was investigated for the spurious mode response with non-symmetric electrodes. The response of such a resonator may be seen in Figure A.3. All modes have the same Q_m factor of 3000.

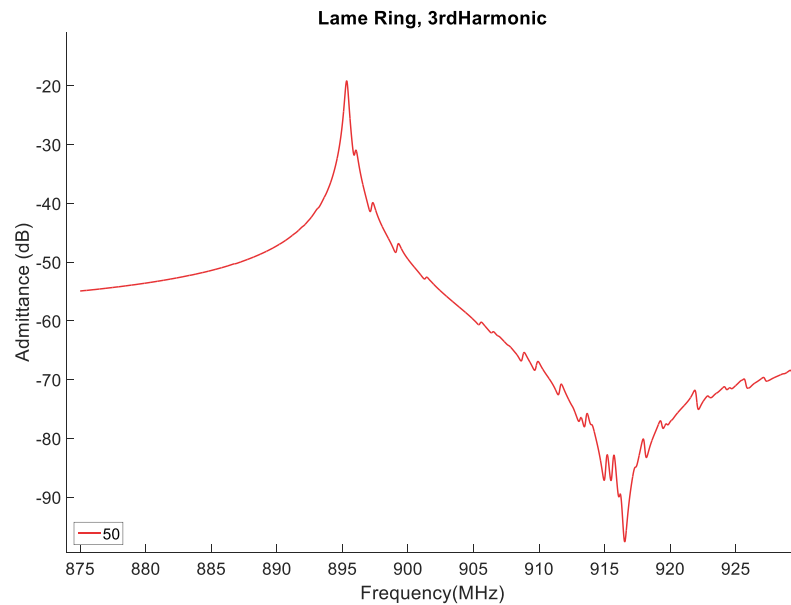


Figure A.3 The simulated response of a ring resonator with a bus and anchor. The bus/anchor break the symmetry and spurious modes appear in the electrical response

Bibliography

- [1] G. Piazza, P. J. Stephanou and A. P. Pisano, "Piezoelectric Aluminum Nitride Vibrating Contour-Mode MEMS Resonators," *Journal of Microelectromechanical Systems*, vol. 15, no. 6, pp. 1406-1418, 2006.
- [2] R. Aigner and L. Elbrecht, "Design and Fabrication of BAW Devices," in *RF Bulk Acoustic Wave Filters for Communications*, K. Hashimoto, Ed., Norwood, Artech House, 2009, pp. 91-115.
- [3] R. Q. Rudy, J. S. Pulskamp, S. S. Bedair, J. M. Puder and R. G. Polcawich, "Piezoelectric Disk Flexure Resonator with 1 dB of Loss," in *2016 IEEE International Frequency Control Symposium*, New Orleans, 2016.
- [4] S. Gong and G. Piazza, "Figure-of-Merit Enhancement for Laterally Vibrating Lithium Niobate MEMS Resonators," *IEEE Transactions on Electron Devices*, vol. 60, no. 11, pp. 3888-3894, 2013.
- [5] J. S. Pulskamp, R. Q. Rudy, S. S. Bedair, M. G. Breen and R. G. Polcawich, "Ferroelectric PZT MEMS HF/VHF Resonators/Filters," in *2016 IEEE Ferroelectric PZT MEMS HF/VHF Resonators/Filters*, New Orleans, 2016.
- [6] J. Wang, J. Butler, T. Feygelson and C. C. Nguyen, "1.51-ghz nanocrystalline diamond micromechanical disk resonator with material-mismatched isolating support," in *17th IEEE International Conference on (MEMS)*, Maastricht, 2004.

- [7] K. Lakin, "Background and History," in *RF Bulk Acoustic Wave Filters For Communications*, K. Hashimoto, Ed., Norwood, Artech House, 2009, pp. 1-19.
- [8] R. Ruby, "Review and Comparison of Bulk Acoustic Wave FBAR, SMR Technology," in *IEEE Ultrasonics Symposium*, New York, 2007.
- [9] R. Wang and S. A. Bhawe, "Design and Fabrication of S0 Lamb-Wave Thin-Film Lithium Niobate Micromechanical Resonators," *Journal of Microelectromechanical Systems*, vol. 24, no. 2, pp. 300-308, 2015.
- [10] S. Gong, "Lithium Niobate for N/MEMS Resonators," in *Piezoelectric MEMS Resonators*, Cham, Springer International, 2017, pp. 99-129.
- [11] C. Cassella, G. Chen, T. Wu, Z. Qian and M. Rinaldi, "Low Impedance Arrays of COupled Cross-Sectional Lame Mode Resonators With High Figure of Merit In Excess of 100," in *The 19t Internaional Conference on Solid-State Seneors, Actuators and Microsystems (TRANSDUCERS)*, Kaohsiung, 2017.
- [12] H. F. Tiersten, *Linear Piezoelectric Plate Vibrations*, New York: Plenum Press, 1969.
- [13] *IEEE Standard on Piezoelectricity*, 1988.
- [14] B. Jaffe, W. Cook and H. Jaffe, *Piezoelectric Ceramics*, Academic Pres Ltd., 1971.
- [15] "IRE Standards on Piezoelectric CrystalsL Measurements of Piezoelectric Ceramics, 1961," *Proceedings of the IRE*, vol. 49, no. 7, pp. 1161-1169, 1961.
- [16] R. Abdolvand, H. Fatemi and S. Moradian, "Quality Factor and Coupling in Piezoelectric MEMS Resonators," in *Piezoelectric MEMS Resonators*, Cham, Springer, 2017, pp. 133-152.
- [17] J. G. Smits, *Eigenstates of Coupling Factor and Loss Factor of Piezoelectric Ceramics*, Technische Hogeschool Twente, Enschede, 1978.
- [18] G. K. Ho, R. Abdolvand, S. H. Sivapurapu and F. Ayazi, "Piezoelectric-on-Silicon Lateral Bulk Acoustic Wave Micromechanical Resonators," *Journal of Microelectromechanical Systems*, vol. 17, no. 2, pp. 512-520, 2008.
- [19] H. Chandralalim, S. A. Bhawe, R. G. Polcawich, J. P. Pulskamp, D. Judy, R. Kaul and M. Dubey, "Influence of Silicon on Quality Factor, Motional Impedance, and Tuning Range of PZT-transduced Resonators," in *2008 Solid State Sensor, Actuator, and Microsystems Workshop*, Hilton Head Island, 2008.
- [20] H. Chandralalim, S. A. Bhawe, R. G. Polcawich, J. P. Pulskamp and R. Kaul, "PZT Transduction of High-Overton Contour-Mode Resonators," *IEEE Transactions on Ultrasonics, Ferroelectrics, and Frequency Control*, vol. 58, no. 9, pp. 2035-2041, 2010.
- [21] K. F. Graff, *Wave Motion in Elastic Solids*, New York: Dover, 1975.
- [22] R. Ruby, "FBAR Resonators and Filters," in *RF Bulk Acoustic Wave Filters For Communications*, Norwood, Artech House, 2009, pp. 117-159.
- [23] Y.-H. Song and S. Gong, "A 1.17 GHz Wideband MEMS Filter Using Higher Order SH0 Lithium Niobate Resonators," in *Solid-State Sensors, Actuators, and Microsystems Conference*, Kaohsiung, 2017.

- [24] H. Majjad, J.-R. Coudevylle, S. Basrour and M. Labachellerie, "Modeling and Characterization of Lamé-Mode Resonators Realized by UV-LIGA," in *Transducers*, Munich, 2001.
- [25] M. Rinaldi, C. Zuniga and G. Piazza, "5-10 GHz AlN Contour-Mode Nanoelectromechanical Resonators," in *IEEE 22nd International Conference on Micro Electro Mechanical Systems*, Sorrento, 2009.
- [26] R. Wang, S. A. Bhave, S. Zhgoon and K. Bhattacharjee, "Multi-Frequency LiNbO₃ Lamb Wave Resonators with < 3 Ohm Impedance," in *29th IEEE International Conference on Micro Electro Mechanical Systems*, Shanghai, 2016.
- [27] R. Q. Rudy, J. S. Pulskamp, S. S. Bedair, J. M. Puder and R. G. Polcawich, "Piezoelectric Disk Flexure Resonator with 1 dB of Loss," in *2016 IEEE International Frequency Control Symposium*, New Orleans, 2016.
- [28] G. Chen, C. Cassella, T. Wu, Z. Qian and M. Rinaldi, *Aluminum Nitride Cross-Sectional Lamé Mode Resonators With Figure of Merit > 134 and Frequency Tunability*, 2017.
- [29] "Ripple (electrical)," Wikipedia, 2008. [Online]. Available: [https://en.wikipedia.org/wiki/Ripple_\(electrical\)](https://en.wikipedia.org/wiki/Ripple_(electrical)). [Accessed 13 Dec 2015].
- [30] A. Link, E. Schidhammer, H. Heinze, M. Mayer, B. Bader and R. Weigel, "Appropriate Methods to Suppress Spurious FBAR Modes in Volume Production," in *2006 IEEE MTT-S International Microwave Symposium Digest*, San Francisco, 2006.
- [31] J. D. Larson, R. C. Ruby and P. Bradley, "Bulk Acoustic Wave Resonator with Improved Lateral Mode Suppression". USA Patent US6215375 B1, 30 Mar 1999.
- [32] L. Sorenson, J. Fu and F. Ayazi, "Linear Acoustic Bandgap Arrays for Spurious Mode Suppression in Piezoelectric MEMS Resonators," in *2011 Joint Conference of the IEEE International Frequency Control and the European Frequency and Time Forum*, San Francisco, 2011.
- [33] M. Giovanni, S. Yazici, N.-K. Kuo and G. Piazza, "Apodization Technique for Spurious Mode Suppression in AlN Contour-Mode Resonators," *Sensors and Actuators A: Physical*, vol. 206, pp. 42-50, 2014.
- [34] J. M. Puder, J. S. Pulskamp, R. Q. Rudy, R. G. Polcawich and S. A. Bhave, "A Method for the Suppression of Multiple Spurious Modes," *Journal of Microelectromechanical Systems*, 2017.
- [35] A. Gao and S. Gong, "Harnessing Mode Conversion for Spurious Mode Suppression in AlN Laterally Vibrating Resonators," *Journal of Microelectromechanical Systems*, vol. 25, no. 3, pp. 450-458, 2016.
- [36] R. Wang, *Thin-Film Lithium Niobate Technology*, Ithaca, 2015.
- [37] R. Polcawich and J. Pulskamp, "Additive Processes for Piezoelectrics Materials: Piezoelectric MEMS," in *MEMS Materials and Processes Handbook*, R. Ghodssi and P. Lin, Eds., New York, Springer, 2011, pp. 273-344.

- [38] P. Murralt, "AlN Thin Film Processing and Basic Properties," in *Piezoelectric MEMS Resonators*, H. Bhugra and G. Piazza, Eds., Cham, Switzerland International, 2017, pp. 1-37.
- [39] R. G. Polcawich and J. S. Pulskamp, "Lead Zirconate Titanate (PZT) for M/NEMS," in *Piezoelectric MEMS Resonators*, H. Bhugra and G. Piazza, Eds., Cham, Springer International Publishing, 2017, pp. 39-71.
- [40] S. Trolier-McKinstry and P. Murralt, "Thin Film Piezoelectrics for MEMS," *Journal of Electroceramics*, vol. 12, no. 1-2, pp. 7-17, 2004.
- [41] J. Guyonnet, *Ferroelectric Domain Walls*, Cham: Springer International, 2014.
- [42] H. Chandralim, S. A. Bhave, R. G. Polcawich, J. S. Pulskamp and R. Kaul, "PZT Transduction of High-Overtone Contour-Mode Resonators," *IEEE Transactions on Ultrasonics, Ferroelectrics, and Frequency Control*, vol. 57, no. 9, pp. 2035-2041, 2010.
- [43] M. Levy, R. M. Osgood, R. Liu, L. E. Cross, G. S. Cargill, A. Kumar and H. Bakhru, "Fabrication of single-crystal lithium niobate films by crystal ion slicing," *Appl. Phys. Lett.*, vol. 73, no. 16, p. 2293-2295, 1998.
- [44] J. D. Larson, P. D. Bradley, S. Wartenberg and R. C. Ruby, "Modifield Butterworth-Van Dyke," in *2000 IEEE Ultrasonics Symposium*, San Juan, 2000.
- [45] *Modal Analysis Book*.
- [46] T. K. Caughey and M. E. O'Kelly, "Effect of Damping on the Natural Frequencies of Linear Dynamic Systems," *The Journal of the Acoustical Society of America*, vol. 33, no. 11, pp. 1458-1461, 1951.
- [47] J. R. Bray and L. Roy, "Measure the unloaded, loaded, and external quality factors of one- and two-port resonators using scattering-parameter magnitudes at fractional power levels," in *IEEE Proceedings: Microwaves, Antennas and Propagation*, 2004.
- [48] R. Q. Rudy, J. M. Puder, J. S. Pulskamp and R. G. Polcawich, "PZT MEMS HF/VHF Resonators and Filters," *Unpublished*.
- [49] D. M. Pozar, *Microwave engineering*.
- [50] N. W. Hagood IV and A. J. McFarland, "Modeling of Piezoelectric Rotary Ultrasonic Motors," *IEEE Transactions on Ultrasonics, Ferroelectrics, and Frequency Control*, vol. 42, no. 2, pp. 210-224, 1995.
- [51] B. Kim, R. H. Olsson and K. E. Wojciechowski, "AlN Microresonator-Based Filters With Multiple Bandwidths at Low Intermediate Frequencies," *Journal of Microelectromechanical Systems*, vol. 22, no. 4, pp. 949-961, 2013.
- [52] N. L. Lobontiu, *Microcantilevers and Microbridges: Bending and Torsion Resonant Frequencies*, 1-5 ed., vol. 17, New York, NY: Springer, 2007.
- [53] J. S. Pulskamp, S. S. Bedair, R. G. Polcawich, G. L. Smith, J. Martin, B. Power and S. A. Bhave, "Electrode-shaping for the Excitation and Detection of Permitted Arbitrary Modes in Arbitrary Geometries in Piezoelectric Resonators," *IEEE Transactions on Ultrasonics, Ferroelectrics and Frequency Control*, vol. 59, no. 5, pp. 1043-1060, 2012.

- [54] J. Kaitila, "BAW Device Basics," in *RF Bulk Acoustic Wave Filters For Communications*, K. Hashimoto, Ed., Boston, Artech House, 2009, pp. 63-64.
- [55] W. Voigt, Ueber die Beziehung zwischen den beiden Elasticitätsconstanten isotroper Körper, Weinheim: WILEY-VCH Verlag, 1889.
- [56] R. D. Blevins, *Formulas for Natural Frequency and Mode Shape*, Malabar: Krieger, 1983.
- [57] T. B. Gabrielson, "Frequency Constants for Transverse Bivration of Annular Disks," *The Journal of the Acoustic Society of America*, vol. 105, no. 6, pp. 3311-3317, 1999.
- [58] T. Irvine, "Natural Frequencies of Circular Plates," Feb 2012. [Online]. [Accessed <http://www.vibrationdata.com/circular.pdf>].
- [59] F. Kremer and A. Schönhals, "Theory of Dielectric Relaxation," in *Broadband Dielectric Spectroscopy*, Berlin, Springer, 2003, pp. I-XXI.
- [60] T. K. Caughey and M. E. O'Kelley, "Classical Normal Modes in Damped Linear Dynamic Systems," *Journal of Applied Mechanics*, vol. 32, pp. 583-588, 1965.
- [61] S. Yagnamurthy, I. Chasiotis, J. Lambros, R. G. Polcawich, J. S. Pulskamp and M. Dubey, "Mechanical and Ferroelectric Behavior of PZT-based Thin Films," *J. of Microelectromech. Systems*, vol. 20, no. 6, pp. 1250-1258, 2011.
- [62] J. M. Puder, J. S. Pulskamp, R. Q. Rudy, S. S. Bedair, R. G. Polcawich, B. Power, J. Martin and S. Isaacson, *Modeling of High-Electric Bias Field Induced Piezoelectric Nonlinearity*, College Station, 2016.
- [63] G. Chen, C. Cassella, Z. Qian, G. Hummel and M. Rinaldi, "Lithographically Defined Aluminum Nitride Cross-Sectional Lamé Mode Resonators," *J. of Micromech. and Microeng.*, vol. 27, no. 3, 2017.
- [64] M. Kamon, *White Paper: Fast Analysis of Acoustic Resonators for the Rapidly Growing Premium RF Filter Market*, 2014.
- [65] J. M. Puder, J. S. Pulskamp, R. Q. Rudy, R. G. Polcawich and S. A. Bhave, "Fundamental Limits of Disk Flexure Resonators," in *International Frequency Control Symposium*, Besancon, 2017.
- [66] M. Kamon, "Computational Modeling Challenges," in *Piezoelectric MEMS Resonators*, Springer, 2017, pp. 257-265.
- [67] K. Uchino, "Piezoelectrici ultrasnoc motors: overview," *Smart Materials and Structures*, vol. 7, no. 3, 1997.
- [68] S. Epstein, "Piezoelectric Stiffening Effects on Various Elastic Properties," in *Ultrasonics Symposium*, Monterey, 1973.
- [69] V. Kaajakari, "Ville Kaajakari's Homepage," [Online]. Available: http://www.kaajakari.net/~ville/research/tutorials/pull_in_tutorial.pdf. [Accessed 11 Sep. 2017].
- [71] A. Arnau and T. Sogorb, "Appendix A Fundamentla of Electrostatics," in *Piezoelectric Transducers and Applications*, Berlin, Springer, 2004, pp. 299-314.

- [72] R. A. Heisin, *Quartz Crystals for Electrical Circuits*, New York: D. Van Nostrand Company, 1946.
- [73] K. F. Graff, "Wave Propagation in Rods and Plates," in *Wave Motion in Elastic Solids*, New York, Dover, 1975, pp. 440-450.